

1 SEARCH FOR PRODUCTION OF A HIGGS BOSON AND A SINGLE TOP
2 QUARK IN MULTILEPTON FINAL STATES IN pp COLLISIONS AT $\sqrt{s} = 13$
3 TeV.

4 by

5 Jose Andres Monroy Montañez

A DISSERTATION

7 Presented to the Faculty of

8 The Graduate College at the University of Nebraska

9 In Partial Fulfilment of Requirements

10 For the Degree of Doctor of Philosophy

11 Major: Physics and Astronomy

¹² Under the Supervision of Kenneth Bloom and Aaron Dominguez

13 Lincoln, Nebraska

14 July, 2018

15 SEARCH FOR PRODUCTION OF A HIGGS BOSON AND A SINGLE TOP
16 QUARK IN MULTILEPTON FINAL STATES IN pp COLLISIONS AT $\sqrt{s} = 13$
17 TeV.

18 Jose Andres Monroy Montañez, Ph.D.

19 University of Nebraska, 2018

20 Adviser: Kenneth Bloom and Aaron Dominguez

₂₁ Table of Contents

₂₂ Table of Contents	iii
₂₃ List of Figures	vii
₂₄ List of Tables	x
₂₅ 1 INTRODUCTION	1
₂₆ 2 Theoretical approach	2
27 2.1 Introduction	2
28 2.2 Standard model of particle physics	3
29 2.2.1 Fermions	5
30 2.2.1.1 Leptons	6
31 2.2.1.2 Quarks	8
32 2.2.2 Fundamental interactions	12
33 2.2.3 Gauge invariance.	16
34 2.2.4 Gauge bosons	18
35 2.3 Electroweak unification and the Higgs mechanism	19
36 2.3.1 Spontaneous symmetry breaking (SSB)	27
37 2.3.2 Higgs mechanism	31

38	2.3.3	Masses of the gauge bosons	34
39	2.3.4	Masses of the fermions	35
40	2.3.5	The Higgs field	36
41	2.3.6	Production of Higgs bosons at LHC	37
42	2.3.7	Higgs boson decay channels	41
43	2.4	Experimental status of the anomalous Higgs-fermion coupling	43
44	2.5	Associated production of a Higgs boson and a single top quark	45
45	2.6	CP-mixing in tH processes	50
46	3	The CMS experiment at the LHC	55
47	3.1	Introduction	55
48	3.2	The LHC	56
49	3.3	The CMS experiment	66
50	3.3.1	CMS coordinate system	69
51	3.3.2	Tracking system	71
52	3.3.3	Silicon strip tracker	74
53	3.3.4	Electromagnetic calorimeter	75
54	3.3.5	Hadronic calorimeter	77
55	3.3.6	Superconducting solenoid magnet	78
56	3.3.7	Muon system	80
57	3.3.8	CMS trigger system	81
58	3.3.9	CMS computing	82
59	4	Event generation, simulation and reconstruction	87
60	4.1	Event generation	88
61	4.2	Monte Carlo Event Generators	92
62	4.3	CMS detector simulation	94

63	4.4 Event reconstruction	95
64	4.4.1 Particle-Flow Algorithm	96
65	4.4.1.1 Missing transverse energy	107
66	4.4.2 Event reconstruction examples	108
67	5 Statistical methods	111
68	5.1 Multivariate analysis	111
69	5.1.1 Decision trees	114
70	5.1.2 Boosted decision trees (BDT)	117
71	5.1.3 Overtraining.	120
72	5.1.4 Variable ranking.	120
73	5.1.5 BDT output example.	121
74	5.2 Statistical inference.	122
75	5.2.1 Nuisance parameters.	122
76	5.2.2 Maximum likelihood estimation method	123
77	5.2.3 Hypothesis test	124
78	5.3 exclusion limits	125
79	5.4 asymptotic limits	125
80	6 Search for production of a Higgs boson and a single top quark in multilepton final states in pp collisions at $\sqrt{s} = 13$ TeV	126
82	6.1 Introduction	126
83	6.2 tHq signature	128
84	6.3 Background processes	130
85	6.4 Data and MC Samples	132
86	6.4.1 Full 2016 dataset and MC samples	132
87	6.4.2 Triggers	133

88	6.5 Object Identification	137
89	6.5.1 Jets and b -jet tagging.	137
90	6.5.2 Missing Energy MET.	138
91	6.5.3 Lepton reconstruction and identification	139
92	6.5.4 Lepton selection efficiency	147
93	6.6 Event selection	149
94	6.7 Background predictions	150
95	6.8 Signal discrimination	152
96	6.8.1 Classifiers response	154
97	6.9 Additional discriminating variables	158
98	Bibliography	160
99	References	162

¹⁰⁰ List of Figures

101	2.1 Standard Model of particle physics.	4
102	2.2 Transformations between quarks	12
103	2.3 Fundamental interactions in nature.	13
104	2.4 SM interactions diagrams	14
105	2.5 Neutral current processes	20
106	2.6 Spontaneous symmetry breaking mechanism	28
107	2.7 SSB Potential form	29
108	2.8 Potential for complex scalar field	30
109	2.9 SSB mechanism for complex scalar field	31
110	2.10 Proton-Proton collision	37
111	2.11 Proton PDFs	38
112	2.12 Higgs boson production mechanism Feynman diagrams	39
113	2.13 Higgs boson production cross section and decay branching ratios	40
114	2.14 κ_t - κ_V plot of the coupling modifiers. ATLAS and CMS combination.	43
115	2.15 Higgs boson production in association with a top quark	46
116	2.16 Cross section for tHq process as a function of κ_t	49
117	2.17 Cross section for tHW process as a function of κ_{Htt}	49
118	2.18 NLO cross section for tX_0 and $t\bar{t}X_0$	53

119	2.19 NLO cross section for $tWX_0, t\bar{t}X_0$.	54
120	3.1 CERN accelerator complex	56
121	3.2 LHC protons source. First acceleration stage.	57
122	3.3 The LINAC2 accelerating system at CERN.	58
123	3.4 LHC layout and RF cavities module.	59
124	3.5 LHC dipole magnet.	61
125	3.6 Integrated luminosity delivered by LHC and recorded by CMS during 2016	63
126	3.7 LHC interaction points	64
127	3.8 Multiple pp collision bunch crossing at CMS.	66
128	3.9 Layout of the CMS detector	67
129	3.10 CMS detector transverse slice	68
130	3.11 CMS detector coordinate system	70
131	3.12 CMS tracking system schematic view.	71
132	3.13 CMS pixel detector	72
133	3.14 SST Schematic view.	74
134	3.15 CMS ECAL schematic view	76
135	3.16 CMS HCAL schematic view	78
136	3.17 CMS solenoid magnet	79
137	3.18 CMS Muon system schematic view	80
138	3.19 CMS Level-1 trigger architecture	82
139	3.20 WLCG structure	83
140	3.21 Data flow from CMS detector through hardware Tiers	85
141	4.1 Event generation process.	88
142	4.2 Particle flow algorithm.	96
143	4.3 Jet reconstruction.	104

144	4.4	Jet energy corrections.	105
145	4.5	Secondary vertex in a b-hadron decay.	106
146	4.6	HIG-13-004 Event 1 reconstruction.	108
147	4.7	$e\mu$ event reconstruction.	109
148	4.8	Recorded event reconstruction.	110
149	5.1	Scatter plots-MVA event classification.	113
150	5.2	Scalar test statistical.	113
151	5.3	Decision tree.	115
152	5.4	Decision tree output example.	118
153	5.5	BDT output example.	121
154	6.1	tHq event signature.	129
155	6.2	$t\bar{t}$ and $t\bar{t}W$ events signature.	131
156	6.3	Tight vs loose lepton selection efficiencies in the 2lss channel.	147
157	6.4	Tight vs loose lepton selection efficiencies in the 3l channel.	148
158	6.5	Input variables to the BDT for signal discrimination normalized.	153
159	6.6	Input variables to the BDT for signal discrimination not normalized.	155
160	6.7	BDT input variables. Discrimination against $t\bar{t}$.	156
161	6.8	BDT input variables. Discrimination against $t\bar{t}V$.	157
162	6.9	Correlation matrices for the BDT input variables.	158
163	6.10	MVA classifiers performance.	158
164	6.11	Additional discriminating variables distributions.	160

¹⁶⁵ List of Tables

166	2.1	Fermions of the SM.	5
167	2.2	Fermion masses.	6
168	2.3	Lepton properties.	8
169	2.4	Quark properties.	9
170	2.5	Fermion weak isospin and weak hypercharge multiplets.	10
171	2.6	Fundamental interactions features.	15
172	2.7	SM gauge bosons.	19
173	2.8	Higgs boson properties.	37
174	2.9	Predicted branching ratios for a SM Higgs boson with $m_H = 125 \text{ GeV}/c^2$	42
175	2.10	Predicted SM cross sections for tH production at $\sqrt{s} = 13 \text{ TeV}$	47
176	2.11	Predicted enhancement of the tHq and tHW cross sections at LHC	50
177	6.1	Signal samples and their cross section and branching fraction.	133
178	6.2	κ_V and κ_t combinations.	134
179	6.3	List of background samples used in this analysis (CMSSW 80X).	135
180	6.4	Leading-order $t\bar{t}W$ and $t\bar{t}Z$ samples used in the signal BDT training.	135
181	6.5	Table of high-level triggers that we consider in the analysis.	136
182	6.6	Trigger efficiency scale factors and associated uncertainties.	137
183	6.7	Effective areas, for electrons and muons.	143

184	6.8 Requirements on each of the three muon selections.	146
185	6.9 Criteria for each of the three electron selections.	146
186	6.10 MVA input discriminating variables	154
187	6.11 TMVA input variables ranking for BDTA_GRAD method	159
188	6.12 TMVA configuration used in the BDT training.	159
189	6.13 ROC-integral for all the testing cases.	161

¹⁹⁰ Chapter 1

¹⁹¹ INTRODUCTION

¹⁹² **Chapter 2**

¹⁹³ **Theoretical approach**

¹⁹⁴ **2.1 Introduction**

¹⁹⁵ The physical description of the universe is a challenge that physicists have faced by
¹⁹⁶ making theories that refine existing principles and proposing new ones in an attempt
¹⁹⁷ to embrace emerging facts and phenomena.

¹⁹⁸ At the end of 1940s Julian Schwinger [1] and Richard P. Feynman [2], based on
¹⁹⁹ the work of Sin-Itiro Tomonaga [3], developed an electromagnetic theory consistent
²⁰⁰ with special relativity and quantum mechanics that describes how matter and light
²⁰¹ interact; the so-called *quantum electrodynamics* (QED) was born.

²⁰² QED has become the blueprint for developing theories that describe the universe.
²⁰³ It was the first example of a quantum field theory (QFT), which is the theoretical
²⁰⁴ framework for building quantum mechanical models that describes particles and their
²⁰⁵ interactions. QFT is composed of a set of mathematical tools that combines classical
²⁰⁶ fields, special relativity and quantum mechanics, while keeping the quantum point
²⁰⁷ particles and locality ideas.

²⁰⁸ This chapter gives an overview of the standard model of particle physics, starting

209 with a description of the particles and their interactions, followed by a description of
 210 the electroweak interaction, the Higgs boson and the associated production of Higgs
 211 boson and a single top quark (tH). The description contained in this chapter is based
 212 on References [4–6].

213 2.2 Standard model of particle physics

214 The *standard model of particle physics (SM)* describes particle physics at the funda-
 215 mental level in terms of a collection of interacting particles and fields. The full picture
 216 of the SM is composed of three fields¹ whose excitations are interpreted as particles
 217 called mediators or force-carriers, a set of fields whose excitations are interpreted as
 218 elementary particles interacting through the exchange of those mediators, and a field
 219 that gives the mass to elementary particles. Figure 2.1 shows a scheme of the SM
 220 particles’ organization. In addition, for each of the particles in the scheme there exists
 221 an antiparticle with the same mass and opposite quantum numbers. The existence of
 222 antiparticles is a prediction of the relativistic quantum mechanics from the solution
 223 of the Dirac equation for which a negative energy solution is also possible. In some
 224 cases a particle is its own anti-particle, like photon or Higgs boson.

225 The mathematical formulation of the SM is based on group theory and the use of
 226 Noether’s theorem [8] which states that for a physical system modeled by a Lagrangian
 227 that is invariant under a group of transformations a conservation law is expected. For
 228 instance, a system described by a time-independent Lagrangian is invariant (symmet-
 229 ric) under time changes (transformations) with the total energy conservation law as
 230 the expected conservation law. In QED, the charge operator (Q) is the generator of

¹ The formal and complete treatment of the SM is out of the scope of this document, however a plenty of textbooks describing it at several levels are available in the literature. The treatment in References [5, 6] is quite comprehensive and detailed. Note that gravitational field is not included in the standard model formulation

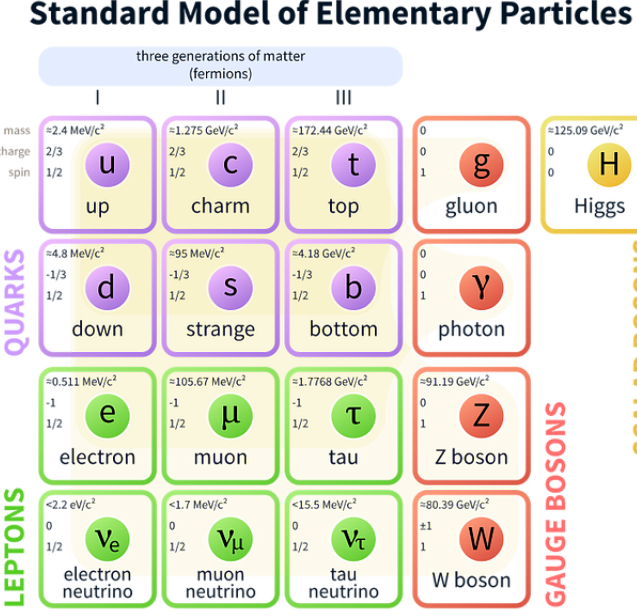


Figure 2.1: Schematic representation of the Standard Model of particle physics. The SM is a theoretical model intended to describe three of the four fundamental forces of the universe in terms of a set of particles and their interactions. [7].

231 the $U(1)$ symmetry which according to the Noether's theorem means that there is a
 232 conserved quantity; this conserved quantity is the electric charge and thus the law
 233 conservation of electric charge is established.

234 In the SM, the symmetry group $SU(3)_C \otimes SU(2)_L \otimes U(1)_Y$ describes three of the
 235 four fundamental interactions in nature (see Section 2.2.2): strong interaction (SI),
 236 weak interaction (WI) and electromagnetic interactions (EI) in terms of symmetries
 237 associated to physical quantities:

- 238 • Strong: $SU(3)_C$ associated to color charge
- 239 • Weak: $SU(2)_L$ associated to weak isospin and chirality
- 240 • Electromagnetic: $U(1)_Y$ associated to weak hypercharge and electric charge
- 241 It will be shown that the electromagnetic and weak interactions are combined in

242 the so-called electroweak interaction where chirality, hypercharge, weak isospin and
 243 electric charge are the central concepts.

244 **2.2.1 Fermions**

245 The basic constituents of the ordinary matter at the lowest level, which form the set
 246 of elementary particles in the SM formulation, are quarks and leptons. All of them
 247 have spin 1/2, therefore they are classified as fermions since they obey Fermi-Dirac
 248 statistics. There are six *flavors* of quarks and three of leptons organized in three
 249 generations, or families, as shown in Table 2.1.

		Generation		
		1st	2nd	3rd
Leptons	Type	Electron (e)	Moun(μ)	Tau (τ)
	Neutral	Electron neutrino (ν_e)	Muon neutrino (ν_μ)	Tau neutrino (ν_τ)
Quarks	Up-type	Up (u)	Charm (c)	Top (t)
	Down-type	Down (d)	Strange (s)	Bottom (b)

Table 2.1: Fermions of the SM. There are six flavors of quarks and three of leptons, organized in three generations, or families, composed of two pairs of closely related particles. The close relationship is motivated by the fact that each pair of particles is a member of an $SU(2)_L$ doublet that has an associated invariance under isospin transformations. WI between leptons is limited to the members of the same generation; WI between quarks is not limited but greatly favored, to same generation members.

250

251 There is a mass hierarchy between generations (see Table 2.2), where the higher
 252 generation particles decays to the lower one, which can explain why the ordinary
 253 matter is made of particles from the first generation. In the SM, neutrinos are modeled
 254 as massless particles so they are not subject to this mass hierarchy; however, today it
 255 is known that neutrinos are massive so the hierarchy could be restated. The reason
 256 behind this mass hierarchy is one of the most important open questions in particle
 257 physics, and it becomes more puzzling when noticing that the mass difference between

258 first and second generation fermions is small compared to the mass difference with
 259 respect to the third generation.

Lepton	Mass (MeV/c ²)	Quark	Mass (MeV/c ²)
e	0.51	u	2.2
μ	105.65	c	1.28×10^3
τ	1776.86	t	173.1×10^3
ν_e	Unknown	d	4.7
ν_μ	Unknown	s	96
τ_μ	Unknown	b	4.18×10^3

Table 2.2: Fermion masses [9]. Generations differ by mass in a way that has been interpreted as a mass hierarchy. Approximate values with no uncertainties are used, for comparison purpose.

260

261 Usually, the second and third generation fermions are produced in high energy
 262 processes, like the ones recreated in particle accelerators.

263 **2.2.1.1 Leptons**

264 A lepton is an elementary particle that is not subject to the SI. As seen in Table 2.1,
 265 there are two types of leptons, the charged ones (electron, muon and tau) and the
 266 neutral ones (the three neutrinos). The electric charge (Q) is the property that gives
 267 leptons the ability to participate in the EI. From the classical point of view, Q plays
 268 a central role determining, among others, the strength of the electric field through
 269 which the electromagnetic force is exerted. It is clear that neutrinos are not affected
 270 by EI because they don't carry electric charge.

271 Another feature of the leptons that is fundamental in the mathematical description
 272 of the SM is the chirality, which is closely related to spin and helicity. Helicity
 273 defines the handedness of a particle by relating its spin and momentum such that
 274 if they are parallel then the particle is right-handed; if spin and momentum are

275 antiparallel the particle is said to be left-handed. The study of parity conservation
 276 (or violation) in β -decay has shown that only left-handed electrons/neutrinos or right-
 277 handed positrons/anti-neutrinos are created [10]; the inclusion of that feature in the
 278 theory was achieved by using projection operators for helicity, however, helicity is
 279 frame dependent for massive particles which makes it not Lorentz invariant and then
 280 another related attribute has to be used: *chirality*.

281 Chirality is a purely quantum attribute which makes it not so easy to describe in
 282 graphical terms but it defines how the wave function of a particle transforms under
 283 certain rotations. As with helicity, there are two chiral states, left-handed chiral (L)
 284 and right-handed chiral (R). In the highly relativistic limit where $E \approx p \gg m$ helicity
 285 and chirality converge, becoming exactly the same for massless particles.

286 In the following, when referring to left-handed (right-handed) it will mean left-
 287 handed chiral (right-handed chiral). The fundamental fact about chirality is that
 288 while EI and SI are not sensitive to chirality, in WI left-handed and right-handed
 289 fermions are treated asymmetrically, such that only left-handed fermions and right-
 290 handed anti-fermions are allowed to couple to WI mediators, which is a violation of
 291 parity. The way to translate this statement in a formal mathematical formulation is
 292 based on the isospin symmetry group $SU(2)_L$.

293 Each generation of leptons is seen as a weak isospin doublet.² The left-handed
 294 charged lepton and its associated left-handed neutrino are arranged in doublets of
 295 weak isospin $T=1/2$ while their right-handed partners are singlets:

$$\begin{pmatrix} \nu_l \\ l \end{pmatrix}_L, l_R := \begin{pmatrix} \nu_e \\ e \end{pmatrix}_L, \begin{pmatrix} \nu_\mu \\ \mu \end{pmatrix}_L, \begin{pmatrix} \nu_\tau \\ \tau \end{pmatrix}_L, e_R, \mu_R, \tau_R, \nu_{eR}, \nu_{\mu R}, \nu_{\tau R} \quad (2.1)$$

296 The isospin third component refers to the eigenvalues of the weak isospin operator

² The weak isospin is an analogy of the isospin symmetry in strong interaction where neutron and proton are affected equally by strong force but differ in their charge.

which for doublets is $T_3 = \pm 1/2$, while for singlets it is $T_3 = 0$. The physical meaning of this doublet-singlet arrangement falls in that the WI couples the two particles in the doublet by exchanging the interaction mediator while the singlet member is not involved in WI. The main properties of the leptons are summarized in Table 2.3.

Although all three flavor neutrinos have been observed, their masses remain unknown and only some estimations have been made [11]. The main reason is that the flavor eigenstates are not the same as the mass eigenstates which implies that when a neutrino is created its mass state is a linear combination of the three mass eigenstates and experiments can only probe the squared difference of the masses. The Pontecorvo-Maki-Nakagawa-Sakata (PMNS) mixing matrix encodes the relationship between flavor and mass eigenstates.

Lepton	$Q(e)$	T_3	L_e	L_μ	L_τ	Lifetime (s)
Electron (e)	-1	-1/2	1	0	0	Stable
Electron neutrino(ν_e)	0	1/2	1	0	0	Unknown
Muon (μ)	-1	-1/2	0	1	0	2.19×10^{-6}
Muon neutrino (ν_μ)	0	1/2	0	1	0	Unknown
Tau (τ)	-1	-1/2	0	0	1	290.3×10^{-15}
Tau neutrino (ν_τ)	0	1/2	0	0	1	Unknown

Table 2.3: Lepton properties [9]. Q: electric charge, T_3 : weak isospin. Only left-handed leptons and right-handed anti-leptons participate in the WI. Anti-particles with inverted T_3 , Q and lepton number complete the leptons set but are not listed. Right-handed leptons and left-handed anti-leptons, neither listed, form weak isospin singlets with $T_3 = 0$ and do not take part in the weak interaction.

308

309 2.2.1.2 Quarks

Quarks are the basic constituents of protons and neutrons. The way quarks join to form bound states, called *hadrons*, is through the SI. Quarks are affected by all the fundamental interactions which means that they carry all the four types of charges: color, electric charge, weak isospin and mass.

Flavor	$Q(e)$	I_3	T_3	B	C	S	T	B'	Y	Color
Up (u)	2/3	1/2	1/2	1/3	0	0	0	0	1/3	r,b,g
Charm (c)	2/3	0	1/2	1/3	1	0	0	0	4/3	r,b,g
Top(t)	2/3	0	1/2	1/3	0	0	1	0	4/3	r,b,g
Down(d)	-1/3	-1/2	-1/2	1/3	0	0	0	0	1/3	r,b,g
Strange(s)	-1/3	0	-1/2	1/3	0	-1	0	0	-2/3	r,b,g
Bottom(b)	-1/3	0	-1/2	1/3	0	0	0	-1	-2/3	r,b,g

Table 2.4: Quark properties [9]. Q: electric charge, I_3 : isospin, T_3 : weak isospin, B: baryon number, C: charmness, S: strangeness, T: topness, B' : bottomness, Y: hypercharge. Anti-quarks posses the same mass and spin as quarks but all charges (color, flavor numbers) have opposite sign.

314

315 Table 2.4 summarizes the features of quarks, among which the most remarkable
 316 is their fractional electric charge. Note that fractional charge is not a problem, given
 317 that quarks are not found isolated, but serves to explain how composed particles are
 318 formed out of two or more valence quarks³.

319 Color charge is responsible for the SI between quarks and is the symmetry ($SU(3)_C$)
 320 that defines the formalism to describe SI. There are three colors: red (r), blue (b)
 321 and green (g) and their corresponding three anti-colors; thus each quark carries one
 322 color unit while anti-quarks carries one anti-color unit. As explained in Section 2.2.2,
 323 quarks are not allowed to be isolated due to the color confinement effect, hence, their
 324 features have been studied indirectly by observing their bound states created when

- 325 • one quark with a color charge is attracted by an anti-quark with the correspond-
 326 ing anti-color charge forming a colorless particle called a *meson*.

 327 • three quarks (anti-quarks) with different color (anti-color) charges are attracted
 328 among them forming a colorless particle called a *baryon (anti-baryon)*.

³ Hadrons can contain an indefinite number of virtual quarks and gluons, known as the quark and gluon sea, but only the valence quarks determine hadrons' quantum numbers.

329 In practice, when a quark is left alone isolated a process called *hadronization* occurs
 330 where the quark emits gluons (see Section 2.2.4) which eventually will generate new
 331 quark-antiquark pairs and so on; those quarks will recombine to form hadrons that
 332 will decay into leptons. This proliferation of particles looks like a *jet* coming from
 333 the isolated quark. More details about the hadronization process and jet structure
 334 will be given in chapter4.

335 In the first version of the quark model (1964), M. Gell-Mann [12] and G. Zweig
 336 [13, 14] developed a consistent way to classify hadrons according to their properties.
 337 Only three quarks (u, d, s) were involved in a scheme in which all baryons have baryon
 338 number $B=1$ and therefore quarks have $B=1/3$; non-baryons have $B=0$. Baryon
 339 number is conserved in SI and EI which means that single quarks cannot be created
 340 but in pairs $q - \bar{q}$.

341 The scheme organizes baryons in a two-dimensional space (I_3 - Y); Y (hyper-
 342 charge) and I_3 (isospin) are quantum numbers related by the Gell-Mann-Nishijima
 343 formula [15, 16]:

$$Q = I_3 + \frac{Y}{2} \quad (2.2)$$

344 where $Y = B + S + C + T + B'$ are the quantum numbers listed in Table 2.4.

345 There are six quark flavors organized in three generations (see Table 2.1) fol-
 346 lowing a mass hierarchy which, again, implies that higher generations decay to first
 347 generation quarks.

	Quarks			T_3	Y_W	Leptons			T_3	Y_W
Doublets	$(\frac{u}{d'})_L$	$(\frac{c}{s'})_L$	$(\frac{t}{b'})_L$	$(\frac{1/2}{-1/2})$	$1/3$	$(\nu_e)_L$	$(\nu_\mu)_L$	$(\nu_\tau)_L$	$(\frac{1/2}{-1/2})$	-1
Singlets	u_R	c_R	t_R	0	$4/3$	ν_{eR}	$\nu_{\mu R}$	$\nu_{\tau R}$	0	-2

Table 2.5: Fermion weak isospin and weak hypercharge multiplets. Weak hypercharge is calculated through the Gell-Mann-Nishijima formula 2.2 but using the weak isospin and charge for quarks.

348

349 Isospin doublets of quarks are also defined (see Table 2.5), and same as for neutrinos,
 350 the WI eigenstates are not the same as the mass eigenstates which means that
 351 members of different quark generations are connected by the WI mediator; thus, up-
 352 type quarks are coupled not to down-type quarks (the mass eigenstates) directly but
 353 to a superposition of down-type quarks (q'_d ; *the weak eigenstates*) via WI according
 354 to:

355

$$\begin{aligned} q'_d &= V_{CKM} q_d \\ \begin{pmatrix} d' \\ s' \\ b' \end{pmatrix} &= \begin{pmatrix} V_{ud} & V_{us} & V_{ub} \\ V_{cd} & V_{cs} & V_{cb} \\ V_{td} & V_{ts} & V_{tb} \end{pmatrix} \begin{pmatrix} d \\ s \\ b \end{pmatrix} \end{aligned} \quad (2.3)$$

356 where V_{CKM} is known as Cabibbo-Kobayashi-Maskawa (CKM) mixing matrix [17,18]
 357 given by

$$\begin{pmatrix} |V_{ud}| & |V_{us}| & |V_{ub}| \\ |V_{cd}| & |V_{cs}| & |V_{cb}| \\ |V_{td}| & |V_{ts}| & |V_{tb}| \end{pmatrix} = \begin{pmatrix} 0.97427 \pm 0.00015 & 0.22534 \pm 0.00065 & 0.00351^{+0.00015}_{-0.00014} \\ 0.22520 \pm 0.00065 & 0.97344 \pm 0.00016 & 0.0412^{+0.0011}_{-0.0005} \\ 0.00867^{+0.00029}_{-0.00031} & 0.0404^{+0.0011}_{-0.0005} & 0.999146^{+0.000021}_{-0.000046} \end{pmatrix}. \quad (2.4)$$

358 The weak decays of quarks are represented in the diagram of Figure 2.2; again
 359 the CKM matrix plays a central role since it contains the probabilities for the differ-
 360 ent quark decay channels, in particular, note that quark decays are greatly favored
 361 between generation members.

362 CKM matrix is a 3×3 unitary matrix parametrized by three mixing angles and
 363 the *CP-mixing phase*; the latter is the parameter responsible for the Charge-Parity

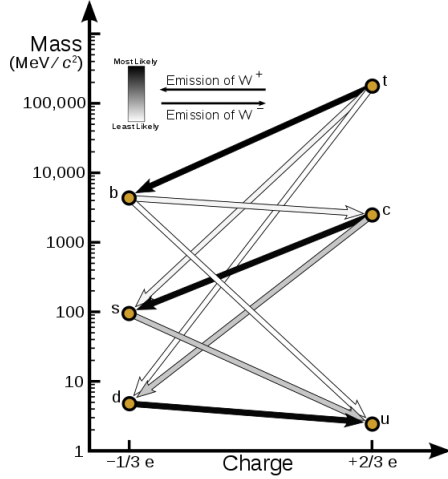


Figure 2.2: Transformations between quarks through the exchange of a WI. Higher generations quarks decay to first generation quarks by emitting a W boson. The arrow color indicates the likelihood of the transition according to the grey scale in the top left side which represent the CKM matrix parameters [19].

364 symmetry violation (CP-violation) in the SM. The fact that the top quark decays
 365 almost all the time to a bottom quark is exploited in this thesis when making the
 366 selection of the signal events by requiring the presence of a jet tagged as a jet coming
 367 from a b quark in the final state.

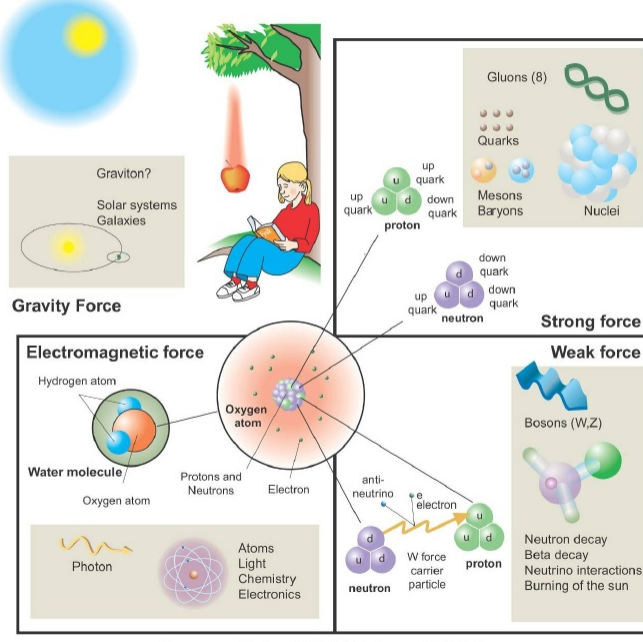
368 2.2.2 Fundamental interactions

369 Even though there are many manifestations of force in nature, like the ones repre-
 370 sented in Figure 2.3, we can classify all of them in four fundamental interactions:

- 371 • *Electromagnetic interaction (EI)* affects particles that are *electrically charged*,
 372 like electrons and protons. Figure 2.4a. shows a graphical representation, known
 373 as *Feynman diagram*, of electron-electron scattering.
- 374 • *Strong interaction (SI)* described by Quantum Chromodynamics (QCD). Hadrons
 375 like the proton and the neutron have internal structure given that they are com-

Fundamental interactions.

Illustration: Typoform



Summer School KPI 15 August 2009

Figure 2.3: Fundamental interactions in nature. Despite the many manifestations of forces in nature, we can track all of them back to one of the fundamental interactions. The most common forces are gravity and electromagnetic given that all of us are subject and experience them in everyday life.

376 posed of two or more valence quarks⁴. Quarks have fractional electric charge
 377 which means that they are subject to electromagnetic interaction and in the case
 378 of the proton they should break apart due to electrostatic repulsion; however,
 379 quarks are held together inside the hadrons against their electrostatic repulsion
 380 by the *Strong Force* through the exchange of *gluons*. The analog to the electric
 381 charge is the *color charge*. Electrons and photons are elementary particles as
 382 quarks but they don't carry color charge, therefore they are not subject to SI. A
 383 Feynman diagram for gluon exchange between quarks is shown in Figure 2.4b.

- 384 • *Weak interaction (WI)* described by the weak theory (WT), is responsible, for
 385 instance, for the radioactive decay in atoms and the deuterium production

⁴ Particles made of four and five quarks are exotic states not so common.

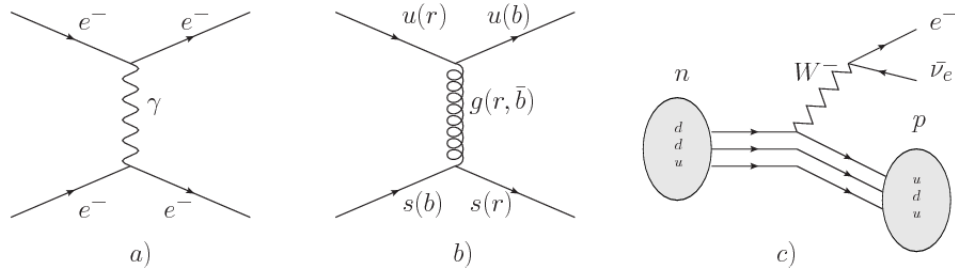


Figure 2.4: Feynman diagrams representing the interactions in SM; a) EI: e - e scattering; b) SI: gluon exchange between quarks ; c) WI: β -decay

within the sun. Quarks and leptons are the particles affected by the weak interaction; they possess a property called *flavor charge* (see 2.2.1) which can be changed by emitting or absorbing one weak force mediator. There are three mediators of the *weak force* known as Z boson in the case of electrically neutral flavor changes and W^\pm bosons in the case of electrically charged flavor changes. The *weak isospin* is the WI analog to electric charge in EI, and color charge in SI, and defines how quarks and leptons are affected by the weak force. Figure 2.4c. shows the Feynman diagram of β -decay where a neutron (n) is transformed in a proton (p) by emitting a W^- particle.

- *Gravitational interaction (GI)* described by General Theory of Relativity (GR). It is responsible for the structure of galaxies and black holes as well as the expansion of the universe. As a classical theory, in the sense that it can be formulated without even appeal to the concept of quantization, it implies that the space-time is a continuum and predictions can be made without limitation to the precision of the measurement tools. The latter represents a direct contradiction of the quantum mechanics principles. Gravity is deterministic while quantum mechanics is probabilistic; despite that, efforts to develop a quantum theory of gravity have predicted the *graviton* as mediator of the gravitational

404 force⁵.

Interaction	Acts on	Relative strength	Range (m)	Mediators
Electromagnetic (QED)	Electrically charged particles	10^{-2}	Infinite	Photon
Strong (QCD)	Quarks and gluons	1	10^{-15}	Gluon
Weak (WI)	Leptons and quarks	10^{-6}	10^{-18}	W^\pm, Z
Gravitational (GI)	Massive particles	10^{-39}	Infinite	Graviton

Table 2.6: Fundamental interactions features [20].

405

406 Table 2.6 summarizes the main features of the fundamental interactions. The
 407 strength of the interactions is represented by the coupling constants which depend
 408 on the energy scale at which the interaction is evaluated, therefore, it is the relative
 409 strength of the fundamental forces that reveals the meaning of strong and weak; in
 410 a context where the relative strength of the SI is 1, the EI is about hundred times
 411 weaker and WI is about million times weaker than the SI. A good description on how
 412 the relative strength and range of the fundamental interactions are calculated can
 413 be found in References [20, 21]. In the everyday life, only EI and GI are explicitly
 414 experienced due to the range of these interactions; i.e., at the human scale distances
 415 only EI and GI have appreciable effects, in contrast to SI which at distances greater
 416 than 10^{-15} m become negligible. Is it important to clarify that the weakness of the
 417 WI is attributed to the fact that its mediators are highly massive which affects the
 418 propagators of the interaction, as a result, the effect of the coupling constant is
 419 reduced.

⁵ Actually a wide variety of theories have been developed in an attempt to describe gravity; some famous examples are string theory and supergravity.

420 **2.2.3 Gauge invariance.**

421 QED was built successfully on the basis of the classical electrodynamics theory (CED)
 422 of Maxwell and Lorentz, following theoretical and experimental requirements imposed
 423 by

- 424 • Lorentz invariance: independence on the reference frame.
- 425 • Locality: interacting fields are evaluated at the same space-time point to avoid
 426 action at a distance.
- 427 • Renormalizability: physical predictions are finite and well defined.
- 428 • Particle spectrum, symmetries and conservation laws already known must emerge
 429 from the theory.
- 430 • Local gauge invariance.

431 The gauge invariance requirement reflects the fact that the fundamental fields
 432 cannot be directly measured but associated fields which are the observables. Electric
 433 (**E**) and magnetic (**B**) fields in CED are associated with the electric scalar potential
 434 V and the vector potential **A**. In particular, **E** can be obtained by measuring the
 435 change in the space of the scalar potential (ΔV); however, two scalar potentials
 436 differing by a constant f correspond to the same electric field. The same happens
 437 in the case of the vector potential **A**; thus, different configurations of the associated
 438 fields result in the same set of values of the observables. The freedom in choosing one
 439 particular configuration is known as *gauge freedom*; the transformation law connecting
 440 two configurations is known as *gauge transformation* and the fact that the observables
 441 are not affected by a gauge transformation is called *gauge invariance*.

442 When the gauge transformation:

$$\begin{aligned} \mathbf{A} &\rightarrow \mathbf{A} - \Delta f \\ V &\rightarrow V - \frac{\partial f}{\partial t} \end{aligned} \tag{2.5}$$

443 is applied to Maxwell equations, they are still satisfied and the fields remain invariant.
 444 Thus, CED is invariant under gauge transformations and is called a *gauge theory*.
 445 The set of all gauge transformations form the *symmetry group* of the theory, which
 446 according to the group theory, has a set of *group generators*. The number of group
 447 generators determine the number of *gauge fields* of the theory.

448 As mentioned in the first lines of Section 2.2, QED has one symmetry group ($U(1)$)
 449 with one group generator (the Q operator) and one gauge field (the electromagnetic
 450 field A^μ). In CED there is not a clear definition, beyond the historical convention,
 451 of which fields are the fundamental and which are the associated, but in QED the
 452 fundamental field is A^μ . When a gauge theory is quantized, the gauge fields are
 453 quantized and their quanta are called *gauge bosons*. The word boson characterizes
 454 particles with integer spin which obey Bose-Einstein statistics.

455 As will be detailed in Section 2.3, interactions between particles in a system can
 456 be obtained by considering first the Lagrangian density of free particles in the sys-
 457 tem, which of course is incomplete because the interaction terms have been left out,
 458 and demanding global phase transformation invariance. Global phase transforma-
 459 tion means that a gauge transformation is performed identically to every point
 460 in the space⁶ and the Lagrangian remains invariant. Then, the global transforma-
 461 tion is promoted to a local phase transformation (this time the gauge transformation
 462 depends on the position in space) and again invariance is required.

⁶ Here space corresponds to the 4-dimensional space i.e. space-time.

463 Due to the space dependence of the local transformation, the Lagrangian density is
 464 not invariant anymore. In order to reinstate the gauge invariance, the gauge covariant
 465 derivative is introduced in the Lagrangian and with it the gauge field responsible for
 466 the interaction between particles in the system. The new Lagrangian density is gauge
 467 invariant, includes the interaction terms needed to account for the interactions and
 468 provides a way to explain the interaction between particles through the exchange of
 469 the gauge boson.

470 This recipe was used to build QED and the theories that aim to explain the
 471 fundamental interactions.

472 2.2.4 Gauge bosons

473 The importance of the gauge bosons comes from the fact that they are the force
 474 mediators or force carriers. The features of the gauge bosons reflect those of the fields
 475 they represent and they are extracted from the Lagrangian density used to describe
 476 the interactions. In Section 2.3, it will be shown how the gauge bosons of the EI and
 477 WI emerge from the electroweak Lagrangian. The SI gauge bosons features are also
 478 extracted from the SI Lagrangian but it is not detailed in this document. The main
 479 features of the SM gauge bosons will be briefly presented below and summarized in
 480 Table 2.7.

481 • **Photon.** EI occurs when the photon couples to (is exchanged between) parti-
 482 cles carrying electric charge; however, The photon itself does not carry electric
 483 charge, therefore, there is no coupling between photons. Given that the photon
 484 is massless the EI is of infinite range, i.e., electrically charged particles interact
 485 even if they are located far away one from each other; this also implies that
 486 photons always move with the speed of light.

- 487 • **Gluon.** SI is mediated by gluons which just as photons are massless. They
 488 carry one unit of color charge and one unit of anticolor charge, hence, gluons
 489 can couple to other gluons. As a result, the range of the SI is not infinite
 490 but very short due to the attraction between gluons, giving rise to the *color*
 491 *confinement* which explains why color charged particles cannot be isolated but
 492 live within composite particles, like quarks inside protons.
- 493 • **W, Z.** W^\pm and Z, are massive which explains their short-range. Given that
 494 the WI is the only interaction that can change the flavor of the interacting
 495 particles, the W boson is the responsible for the nuclear transmutation where
 496 a neutron is converted into a proton or vice versa with the involvement of an
 497 electron and a neutrino (see Figure 2.4c). The Z boson is the responsible for the
 498 neutral weak processes like neutrino elastic scattering where no electric charge
 499 but momentum transference is involved. WI gauge bosons carry isospin charge
 500 which makes interaction between them possible.

Interaction	Mediator	Electric charge (e)	Color charge	Weak Isospin	mass (GeV/c ²)
Electromagnetic	Photon (γ)	0	No	0	0
Strong	Gluon (g)	0	Yes -octet	No	0
Weak	W^\pm	± 1	No	± 1	80.385 ± 0.015
	Z	0	No	0	91.188 ± 0.002

Table 2.7: SM gauge bosons main features [9].

501

502 2.3 Electroweak unification and the Higgs 503 mechanism

504 Physicists dream of building a theory that contains all the interactions in one single
 505 interaction, i.e., showing that at some scale in energy all the four fundamental inter-

actions are unified and only one interaction emerges in a *Theory of everything*. The first sign of the feasibility of such unification came from success in the construction of the CED. Einstein spent years trying to reach that full unification, which by 1920 only involved electromagnetism and gravity, with no success; however, a new partial unification was achieved in the 1960's, when S.Glashow [22], A.Salam [23] and S.Weinberg [24] independently proposed that electromagnetic and weak interactions are two manifestations of a more general interaction called *electroweak interaction* (EWI). EWI was developed by following the useful prescription provided by QED and the gauge invariance principles.

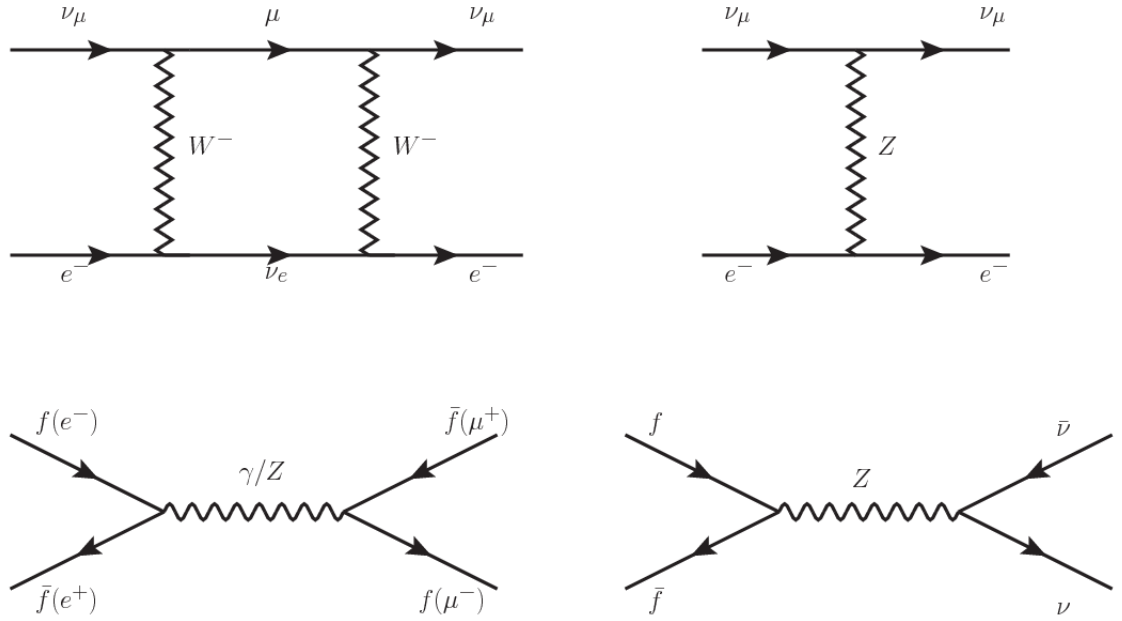


Figure 2.5: Top: $\nu_\mu - e^-$ scattering going through charged currents (left) and neutral currents (right). Bottom: neutral current processes for charged fermions (left) and involving neutrinos (right). While neutral current processes involving only charged fermions can proceed through EI or WI, those involving neutrinos can only proceed via WI.

The *classic* weak theory developed by Fermi, did not have the concept of the W boson but instead it was treated as a point interaction with the dimensionful constant G_F associated with it. It works really well at low energies very far off the W mass

518 shell. When going up in energy, the theory of weak interactions involving the W
 519 boson is capable of explaining the β -decay and in general the processes mediated by
 520 W^\pm bosons. However, there were some processes like the $\nu_\mu - e$ scattering which
 521 would require the exchange of two W bosons (see Figure 2.5 top diagrams) giving
 522 rise to divergent loop integrals and then non-finite predictions. The EWI theory, by
 523 including neutral currents involving fermions via the exchange of a neutral bosons Z,
 524 overcomes those divergences and the predictions become realistic.

525 Neutral weak interaction vertices conserve flavor in the same way as the electro-
 526 magnetic vertices do, but additionally, the Z boson can couple to neutrinos which
 527 implies that processes involving charged fermions can proceed through EI or WI but
 528 processes involving neutrinos can proceed only through WI.

529 The prescription to build a gauge theory of the WI consists of proposing a free
 530 field Lagrangian density that includes the particles involved; next, by requesting
 531 invariance under global phase transformations first and generalizing to local phase
 532 transformations invariance later, the conserved currents are identified and interactions
 533 are generated by introducing gauge fields. Given that the goal is to include the EI
 534 and WI in a single theory, the group symmetry considered should be a combination of
 535 $SU(2)_L$ and $U(1)_{em}$, however the latter cannot be used directly because the EI treats
 536 left and right-handed particles indistinctly in contrast to the former. Fortunately, the
 537 weak hypercharge, which is a combination of the weak isospin and the electric charge
 538 (Eqn. 2.2) is suitable to be used since it is conserved by the EI and WI. Thus, the
 539 symmetry group to be considered is

$$G \equiv SU(2)_L \otimes U(1)_Y \quad (2.6)$$

540 The following treatment applies to any of the fermion generations, but for sim-

541 plicity the first generation of leptons will be considered [5, 6, 25, 26].

542 Given the first generation of leptons

$$\psi_1 = \begin{pmatrix} \nu_e \\ e^- \end{pmatrix}_L, \quad \psi_2 = \nu_{eR}, \quad \psi_3 = e_R^- \quad (2.7)$$

543 the charged fermionic currents are given by

$$J_\mu \equiv J_\mu^+ = \bar{\nu}_{eL} \gamma_\mu e_L, \quad J_\mu^\dagger \equiv J_\mu^- = \bar{e}_L \gamma_\mu \nu_{eL} \quad (2.8)$$

544 and the free Lagrangian is given by

$$\mathcal{L}_0 = \sum_{j=1}^3 i\bar{\psi}_j(x) \gamma^\mu \partial_\mu \psi_j(x). \quad (2.9)$$

545 Mass terms are included directly in the QED free Lagrangians since they preserve
 546 the invariance under the symmetry transformations involved which treat left and right
 547 handed particles similarly, however mass terms of the form

$$m_W^2 W_\mu^\dagger(x) W^\mu(x) + \frac{1}{2} m_Z^2 Z_\mu(x) Z^\mu(x) - m_e \bar{\psi}_e(x) \psi_e(x) \quad (2.10)$$

548 which represent the mass of W^\pm , Z and electrons, are not invariant under G trans-
 549 formations, therefore the gauge fields described by the EWI are in principle massless.

550 Experiments have shown that the EWI gauge fields are not massless [27–30];
 551 however, they have to acquire mass through a mechanism compatible with the gauge
 552 invariance; that mechanism is known as the *Higgs mechanism* and will be considered
 553 later in this Section. The global transformations in the combined symmetry group G
 554 can be written as

$$\begin{aligned}
\psi_1(x) &\xrightarrow{G} \psi'_1(x) \equiv U_Y U_L \psi_1(x), \\
\psi_2(x) &\xrightarrow{G} \psi'_2(x) \equiv U_Y \psi_2(x), \\
\psi_3(x) &\xrightarrow{G} \psi'_3(x) \equiv U_Y \psi_3(x)
\end{aligned} \tag{2.11}$$

555 where U_L represent the $SU(2)_L$ transformation acting only on the weak isospin dou-
 556 blet and U_Y represent the $U(1)_Y$ transformation acting on all the weak isospin mul-
 557 tiplets. Explicitly

$$U_L \equiv \exp\left(i \frac{\sigma_i}{2} \alpha^i\right), \quad U_Y \equiv \exp(i y_i \beta) \quad (i = 1, 2, 3) \tag{2.12}$$

558 with σ_i the Pauli matrices and y_i the weak hypercharges. In order to promote the
 559 transformations from global to local while keeping the invariance, it is required that
 560 $\alpha^i = \alpha^i(x)$, $\beta = \beta(x)$ and the replacement of the ordinary derivatives by the covariant
 561 derivatives

$$\begin{aligned}
D_\mu \psi_1(x) &\equiv \left[\partial_\mu + ig\sigma_i W_\mu^i(x)/2 + ig'y_1 B_\mu(x) \right] \psi_1(x) \\
D_\mu \psi_2(x) &\equiv \left[\partial_\mu + ig'y_2 B_\mu(x) \right] \psi_2(x) \\
D_\mu \psi_3(x) &\equiv \left[\partial_\mu + ig'y_3 B_\mu(x) \right] \psi_3(x)
\end{aligned} \tag{2.13}$$

562 introducing in this way four gauge fields, $W_\mu^i(x)$ and $B_\mu(x)$, in the process. The
 563 covariant derivatives (Eqn. 2.13) are required to transform in the same way as fermion
 564 fields $\psi_i(x)$ themselves, therefore, the gauge fields transform as:

$$\begin{aligned} B_\mu(x) &\xrightarrow{G} B'_\mu(x) \equiv B_\mu(x) - \frac{1}{g'} \partial_\mu \beta(x) \\ W_\mu^i(x) &\xrightarrow{G} W_\mu^{i\prime}(x) \equiv W_\mu^i(x) - \frac{i}{g} \partial_\mu \alpha_i(x) - \varepsilon_{ijk} \alpha_i(x) W_\mu^j(x). \end{aligned} \quad (2.14)$$

565 The G invariant version of the Lagrangian density 2.9 can be written as

$$\mathcal{L}_0 = \sum_{j=1}^3 i \bar{\psi}_j(x) \gamma^\mu D_\mu \psi_j(x) \quad (2.15)$$

566 where free massless fermion and gauge fields and fermion-gauge boson interactions
 567 are included. The EWI Lagrangian density must additionally include kinetic terms
 568 for the gauge fields (\mathcal{L}_G) which are built from the field strengths, according to

$$B_{\mu\nu}(x) \equiv \partial_\mu B_\nu - \partial_\nu B_\mu \quad (2.16)$$

$$W_{\mu\nu}^i(x) \equiv \partial_\mu W_\nu^i(x) - \partial_\nu W_\mu^i(x) - g \varepsilon^{ijk} W_\mu^j W_\nu^k \quad (2.17)$$

569 the last term in Eqn. 2.17 is added in order to hold the gauge invariance; therefore,

$$\mathcal{L}_G = -\frac{1}{4} B_{\mu\nu}(x) B^{\mu\nu}(x) - \frac{1}{4} W_{\mu\nu}^i(x) W_i^{\mu\nu}(x) \quad (2.18)$$

570 which contains not only the free gauge fields contributions, but also the gauge fields
 571 self-interactions and interactions among them.

572 The three weak isospin conserved currents resulting from the $SU(2)_L$ symmetry
 573 are given by

$$J_\mu^i(x) = \frac{1}{2} \bar{\psi}_1(x) \gamma_\mu \sigma^i \psi_1(x) \quad (2.19)$$

574 while the weak hypercharge conserved current resulting from the $U(1)_Y$ symmetry is
 575 given by

$$J_\mu^Y = \sum_{j=1}^3 \bar{\psi}_j(x) \gamma_\mu y_j \psi_j(x) \quad (2.20)$$

576 In order to evaluate the electroweak interactions modeled by an isos triplet field
 577 W_μ^i that couples to isospin currents J_μ^i with strength g and additionally the singlet
 578 field B_μ which couples to the weak hypercharge current J_μ^Y with strength $g'/2$. The
 579 interaction Lagrangian density to be considered is

$$\mathcal{L}_I = -g J^{i\mu}(x) W_\mu^i(x) - \frac{g'}{2} J^{Y\mu}(x) B_\mu(x) \quad (2.21)$$

580 Note that the weak isospin currents are not the same as the charged fermionic cur-
 581 rents that were used to describe the WI (Eqn. 2.8), since the weak isospin eigenstates
 582 are not the same as the mass eigenstates, but they are closely related

$$J_\mu = \frac{1}{2}(J_\mu^1 + iJ_\mu^2), \quad J_\mu^\dagger = \frac{1}{2}(J_\mu^1 - iJ_\mu^2). \quad (2.22)$$

583 The same happens with the gauge fields W_μ^i which are related to the mass eigen-
 584 states W^\pm by

$$W_\mu^+ = \frac{1}{\sqrt{2}}(W_\mu^1 - iW_\mu^2), \quad W_\mu^- = \frac{1}{\sqrt{2}}(W_\mu^1 + iW_\mu^2). \quad (2.23)$$

585 The fact that there are three weak isospin conserved currents is an indication that
 586 in addition to the charged fermionic currents, which couple charged to neutral leptons,
 587 there should be a neutral fermionic current that does not involve electric charge
 588 exchange; therefore, it couples neutral fermions or fermions of the same electric charge.
 589 The third weak isospin current contains a term that is similar to the electromagnetic

590 current (j_μ^{em}), indicating that there is a relation between them and resembling the
 591 Gell-Mann-Nishijima formula 2.2 adapted to electroweak interactions

$$Q = T_3 + \frac{Y_W}{2}. \quad (2.24)$$

592 Just as Q generates the $U(1)_{em}$ symmetry, the weak hypercharge generates the
 593 $U(1)_Y$ symmetry as said before. It is possible to write the relationship in terms of
 594 the currents as

$$j_\mu^{em} = J_\mu^3 + \frac{1}{2} J_\mu^Y. \quad (2.25)$$

595 The neutral gauge fields W_μ^3 and B_μ cannot be directly identified with the Z
 596 and the photon fields since the photon interacts similarly with left and right-handed
 597 fermions; however, they are related through a linear combination given by

$$\begin{aligned} A_\mu &= B_\mu \cos \theta_W + W_\mu^3 \sin \theta_W \\ Z_\mu &= -B_\mu \sin \theta_W + W_\mu^3 \cos \theta_W \end{aligned} \quad (2.26)$$

where θ_W is known as the *Weinberg angle*. The interaction Lagrangian is now given by

$$\begin{aligned} \mathcal{L}_I = -\frac{g}{\sqrt{2}}(J^\mu W_\mu^+ + J^{\mu\dagger} W_\mu^-) - &\left(g \sin \theta_W J_\mu^3 + g' \cos \theta_W \frac{J_\mu^Y}{2}\right) A^\mu \\ &- \left(g \cos \theta_W J_\mu^3 - g' \sin \theta_W \frac{J_\mu^Y}{2}\right) Z^\mu \end{aligned} \quad (2.27)$$

598 the first term is the weak charged current interaction, while the second term is the

599 electromagnetic interaction under the condition

$$g \sin \theta_W = g' \cos \theta_W = e, \quad \frac{g'}{g} = \tan \theta_W \quad (2.28)$$

600 contained in the Eqn.2.25; the third term is the neutral weak current.

601

602 Note that the neutral fields transformation given by the Eqn. 2.26 can be written
 603 in terms of the coupling constants g and g' as:

$$A_\mu = \frac{g' W_\mu^3 + g B_\mu}{\sqrt{g^2 + g'^2}}, \quad Z_\mu = \frac{g W_\mu^3 - g' B_\mu}{\sqrt{g^2 + g'^2}}. \quad (2.29)$$

604 So far, the Lagrangian density describing the non-massive EWI is:

$$\mathcal{L}_{nmEWI} = \mathcal{L}_0 + \mathcal{L}_G \quad (2.30)$$

605 where fermion and gauge fields have been considered massless because their regular
 606 mass terms are manifestly non invariant under G transformations; therefore, masses
 607 have to be generated in a gauge invariant way. The mechanism by which this goal is
 608 achieved is known as the *Higgs mechanism* and is closely connected to the concept of
 609 *spontaneous symmetry breaking*.

610 2.3.1 Spontaneous symmetry breaking (SSB)

611 Figure 2.6 left shows a steel nail (top) which is subject to an external force; the form
 612 of the potential energy is also shown (bottom).

613 Before reaching the critical force value, the system has rotational symmetry with
 614 respect to the nail axis; however, after the critical force value is reached the nail buck-

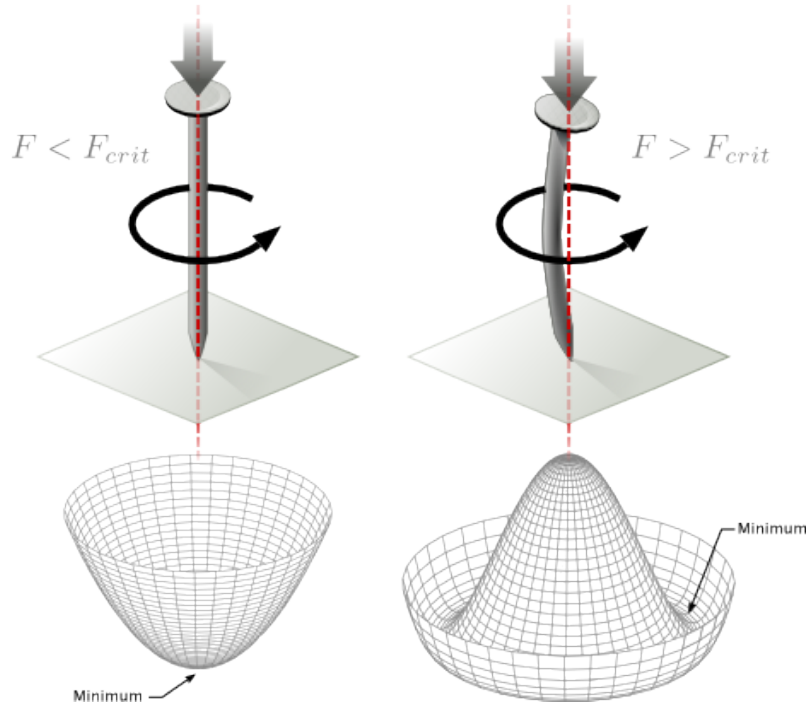


Figure 2.6: Spontaneous symmetry breaking mechanism. The steel nail, subject to an external force (top left), has rotational symmetry with respect to its axis. When the external force overcomes a critical value the nail buckles (top right) choosing a minimal energy state (ground state) and thus *breaking spontaneously the rotational symmetry*. The potential energy (bottom) changes but holds the rotational symmetry; however, an infinite number of asymmetric ground states are generated and circularly distributed in the bottom of the potential [31].

615 les (top right). The form of the potential energy (bottom right) changes appearing a
 616 set of infinity minima but preserving its rotational symmetry. Right before the nail
 617 buckles there is no indication of the direction the nail will bend because any of the
 618 directions are equivalent, but once the nail bends, choosing a direction, an arbitrary
 619 minimal energy state (ground state) is selected and it does not share the system's
 620 rotational symmetry. This mechanism for reaching an asymmetric ground state is
 621 known as *spontaneous symmetry breaking*.

622 The lesson from this analysis is that the way to introduce the SSB mechanism
 623 into a system is by adding the appropriate potential to it.

624 Figure 2.7 shows a plot of the potential $V(\phi)$ in the case of a scalar field ϕ

$$V(\phi) = \mu^2 \phi^\dagger \phi + \lambda (\phi^\dagger \phi)^2 \quad (2.31)$$

625 If $\mu^2 > 0$ the potential has only one minimum at $\phi = 0$ and describes a scalar field
 626 with mass μ . If $\mu^2 < 0$ the potential has a local maximum at $\phi = 0$ and two minima
 627 at $\phi = \pm\sqrt{-\mu^2/\lambda}$ which enables the SSB mechanism to work.

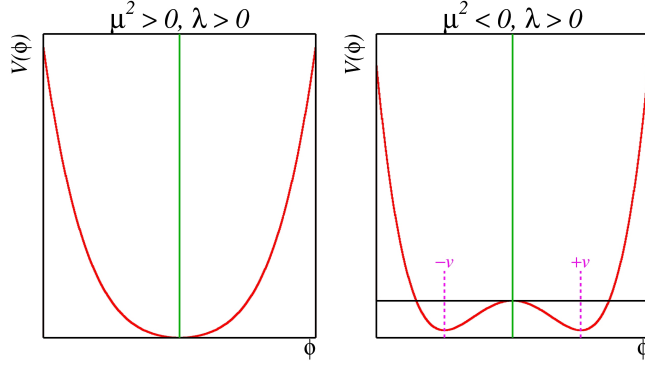


Figure 2.7: Shape of the potential $V(\phi)$ for $\lambda > 0$ and: $\mu^2 > 0$ (left) and $\mu^2 < 0$ (right). The case $\mu^2 < 0$ corresponds to the potential suitable for introducing the SSB mechanism by choosing one of the two ground states which are connected via reflection symmetry. [31].

628 In the case of a complex scalar field $\phi(x)$

$$\phi(x) = \frac{1}{\sqrt{2}}(\phi_1 + i\phi_2) \quad (2.32)$$

629 the Lagrangian (invariant under global $U(1)$ transformations) is given by

$$\mathcal{L} = (\partial_\mu \phi)^\dagger (\partial^\mu \phi) - V(\phi), \quad V(\phi) = \mu^2 \phi^\dagger \phi + \lambda (\phi^\dagger \phi)^2 \quad (2.33)$$

630 where an appropriate potential has been added in order to introduce the SSB.

631 As seen in Figure 2.8, the potential has now an infinite number of minima circularly
 632 distributed along the ξ -direction which makes possible the occurrence of the SSB by
 633 choosing an arbitrary ground state; for instance, $\xi = 0$, i.e. $\phi_1 = v, \phi_2 = 0$

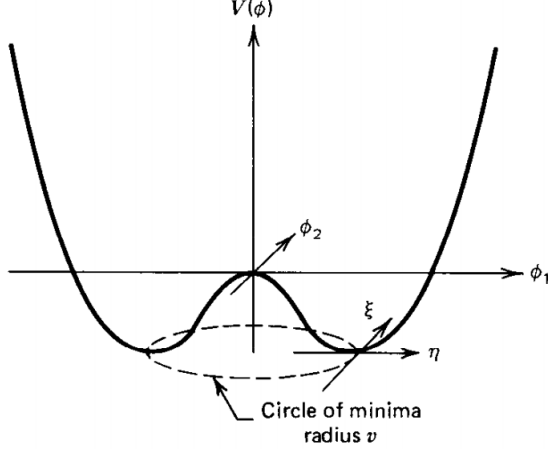


Figure 2.8: Potential for complex scalar field. There is a circle of minima of radius v along the ξ -direction [6].

$$\phi_0 = \frac{v}{\sqrt{2}} \exp(i\xi) \xrightarrow{\text{SSB}} \phi_0 = \frac{v}{\sqrt{2}} \quad (2.34)$$

634 As usual, excitations over the ground state are studied by making an expansion
 635 about it; thus, the excitations can be parametrized as:

$$\phi(x) = \frac{1}{\sqrt{2}}(v + \eta(x) + i\xi(x)) \quad (2.35)$$

636 which when substituted into Eqn. 2.33 produces a Lagrangian in terms of the new
 637 fields η and ξ

$$\mathcal{L}' = \frac{1}{2}(\partial_\mu \xi)^2 + \frac{1}{2}(\partial_\mu \eta)^2 + \mu^2 \eta^2 - V(\phi_0) - \lambda v \eta (\eta^2 + \xi^2) - \frac{\lambda}{4}(\eta^2 + \xi^2)^2 \quad (2.36)$$

638 where the last two terms represent the interactions and self-interaction between the
 639 two fields η and ξ . The particular feature of the SSB mechanism is revealed when
 640 looking to the first three terms of \mathcal{L}' . Before the SSB, only the massless ϕ field is

641 present in the system; after the SSB there are two fields of which the η -field has
 642 acquired mass $m_\eta = \sqrt{-2\mu^2}$ while the ξ -field is still massless (see Figure 2.9).

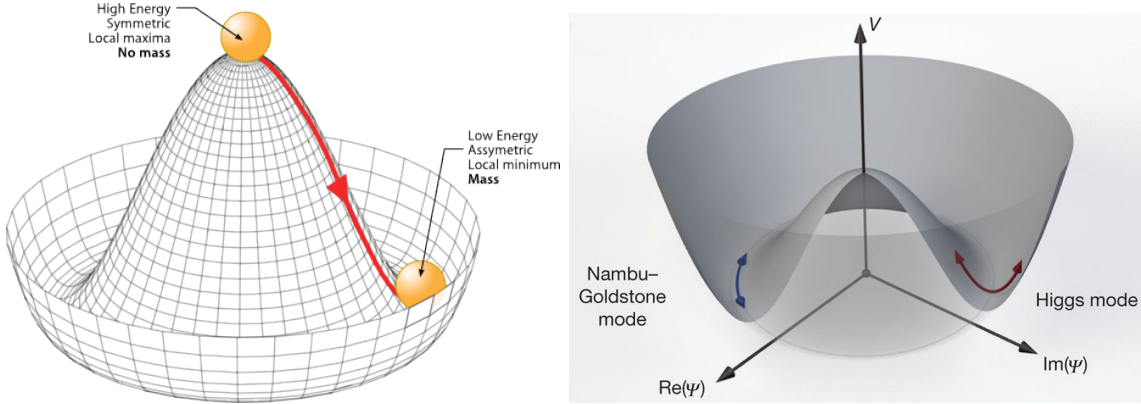


Figure 2.9: SSB mechanism for a complex scalar field [31, 32].

643 Thus, the SSB mechanism serves as a method to generate mass but as a side ef-
 644 fect a massless field is introduced in the system. This fact is known as the Goldstone
 645 theorem and states that a massless scalar field appears in the system for each con-
 646 tinuous symmetry spontaneously broken. Another version of the Goldstone theorem
 647 states that “if a Lagrangian is invariant under a continuous symmetry group G , but
 648 the vacuum is only invariant under a subgroup $H \subset G$, then there must exist as many
 649 massless spin-0 particles (Nambu-Goldstone bosons) as broken generators.” [26] The
 650 Nambu-Goldstone boson can be understood considering that the potential in the ξ -
 651 direction is flat so excitations in that direction are not energy consuming and thus
 652 represent a massless state.

653 2.3.2 Higgs mechanism

654 When the SSB mechanism is introduced in the formulation of the EWI in an attempt
 655 to generate the mass of the so far massless gauge bosons and fermions, an interesting
 656 effect is revealed. In order to keep the G symmetry group invariance and generate

657 the mass of the EW gauge bosons, a G invariant Lagrangian density (\mathcal{L}_S) has to be
 658 added to the non massive EWI Lagrangian (Eqn. 2.30)

$$\mathcal{L}_S = (D_\mu \phi)^\dagger (D^\mu \phi) - \mu^2 \phi^\dagger \phi - \lambda (\phi^\dagger \phi)^2, \quad \lambda > 0, \mu^2 < 0 \quad (2.37)$$

$$D_\mu \phi = \left(i\partial_\mu - g \frac{\sigma_i}{2} W_\mu^i - g' \frac{Y}{2} B_\mu \right) \phi \quad (2.38)$$

659 ϕ has to be an isospin doublet of complex scalar fields so it preserves the G invariance;
 660 thus ϕ can be defined as:

$$\phi = \begin{pmatrix} \phi^+ \\ \phi^0 \end{pmatrix} \equiv \frac{1}{\sqrt{2}} \begin{pmatrix} \phi_1 + i\phi_2 \\ \phi_3 + i\phi_4 \end{pmatrix}. \quad (2.39)$$

661 The minima of the potential are defined by

$$\phi^\dagger \phi = \frac{1}{2} (\phi_1^2 + \phi_2^2 + \phi_3^2 + \phi_4^2) = -\frac{\mu^2}{2\lambda}. \quad (2.40)$$

662 The choice of the ground state is critical. By choosing a ground state, invariant
 663 under $U(1)_{em}$ gauge symmetry, the photon will remain massless and the W^\pm and Z
 664 bosons masses will be generated which is exactly what is needed. In that sense, the
 665 best choice corresponds to a weak isospin doublet with $T_3 = -1/2$, $Y_W = 1$ and $Q = 0$
 666 which defines a ground state with $\phi_1 = \phi_2 = \phi_4$ and $\phi_3 = v$:

$$\phi_0 \equiv \frac{1}{\sqrt{2}} \begin{pmatrix} 0 \\ v \end{pmatrix}, \quad v^2 \equiv -\frac{\mu^2}{\lambda}. \quad (2.41)$$

667 where the vacuum expectation value v is fixed by the Fermi coupling G_F according
 668 to $v = (\sqrt{2}G_F)^{1/2} \approx 246$ GeV.

669 The G symmetry has been broken and three Nambu-Goldstone bosons will appear.

670 The next step is to expand ϕ about the chosen ground state as:

$$\phi(x) = \frac{1}{\sqrt{2}} \exp\left(\frac{i}{v} \sigma_i \theta^i(x)\right) \begin{pmatrix} 0 \\ v + H(x) \end{pmatrix} \approx \frac{1}{\sqrt{2}} \begin{pmatrix} \theta_1(x) + i\theta_2(x) \\ v + H(x) - i\theta_3(x) \end{pmatrix} \quad (2.42)$$

671 to describe fluctuations from the ground state ϕ_0 . The fields $\theta_i(x)$ represent the
 672 Nambu-Goldstone bosons while $H(x)$ is known as *Higgs field*. The fundamental fea-
 673 ture of the parametrization used is that the dependence on the $\theta_i(x)$ fields is factored
 674 out in a global phase that can be eliminated by taking the physical *unitary gauge*
 675 $\theta_i(x) = 0$. Therefore the expansion about the ground state is given by:

$$\phi(x) \frac{1}{\sqrt{2}} \begin{pmatrix} 0 \\ v + H(x) \end{pmatrix} \quad (2.43)$$

676 which when substituted into \mathcal{L}_S (Eqn. 2.37) results in a Lagrangian containing the
 677 now massive three gauge bosons W^\pm, Z , one massless gauge boson (photon) and
 678 the new Higgs field (H). The three degrees of freedom corresponding to the Nambu-
 679 Goldstone bosons are now integrated into the massive gauge bosons as their lon-
 680 gitudinal polarizations which were not available when they were massless particles.
 681 The effect by which vector boson fields acquire mass after an spontaneous symmetry
 682 breaking, but without an explicit gauge invariance breaking is known as the *Higgs*
 683 *mechanism*.

684 The mechanism was proposed by three independent groups: F.Englert and R.Brout
 685 in August 1964 [33], P.Higgs in October 1964 [34] and G.Guralnik, C.Hagen and
 686 T.Kibble in November 1964 [35]; however, its importance was not realized until
 687 S.Glashow [22], A.Salam [23] and S.Weinberg [24], independently, proposed that elec-
 688 tromagnetic and weak interactions are two manifestations of a more general interac-
 689 tion called *electroweak interaction* in 1967.

690 **2.3.3 Masses of the gauge bosons**

691 The masses of the gauge bosons are extracted by evaluating the kinetic part of La-
 692 grangian \mathcal{L}_S in the ground state (known also as the vacuum expectation value), i.e.,

$$\left| \left(\partial_\mu - ig \frac{\sigma_i}{2} W_\mu^i - i \frac{g'}{2} B_\mu \right) \phi_0 \right|^2 = \left(\frac{1}{2} v g \right)^2 W_\mu^+ W^{-\mu} + \frac{1}{8} v^2 (W_\mu^3, B_\mu) \begin{pmatrix} g^2 & -gg' \\ -gg' & g'^2 \end{pmatrix} \begin{pmatrix} W^{3\mu} \\ B^\mu \end{pmatrix} \quad (2.44)$$

693 comparing with the typical mass term for a charged boson $M_W^2 W^+ W^-$

$$M_W = \frac{1}{2} v g. \quad (2.45)$$

The second term in the right side of the Eqn.2.44 comprises the masses of the neutral bosons, but it needs to be written in terms of the gauge fields Z_μ and A_μ in order to be compared to the typical mass terms for neutral bosons, therefore using Eqn. 2.29

$$\begin{aligned} \frac{1}{8} v^2 [g^2 (W_\mu^3)^2 - 2gg' W_\mu^3 B^\mu + g'^2 B_\mu^2] &= \frac{1}{8} v^2 [g W_\mu^3 - g' B_\mu]^2 + 0[g' W_\mu^3 + g B_\mu]^2 \quad (2.46) \\ &= \frac{1}{8} v^2 [\sqrt{g^2 + g'^2} Z_\mu]^2 + 0[\sqrt{g^2 + g'^2} A_\mu]^2 \end{aligned}$$

694 and then

$$M_Z = \frac{1}{2} v \sqrt{g^2 + g'^2}, \quad M_A = 0 \quad (2.47)$$

695 **2.3.4 Masses of the fermions**

696 The lepton mass terms can be generated by introducing a gauge invariant Lagrangian
 697 term describing the Yukawa coupling between the lepton field and the Higgs field

$$\mathcal{L}_{Yl} = -G_l \left[(\bar{\nu}_l, \bar{l})_L \begin{pmatrix} \phi^+ \\ \phi^0 \end{pmatrix} l_R + \bar{l}_R (\phi^-, \bar{\phi}^0) \begin{pmatrix} \nu_l \\ l \end{pmatrix} \right], \quad l = e, \mu, \tau. \quad (2.48)$$

698 After the SSB and replacing the usual field expansion about the ground state
 699 (Eqn.2.41) into \mathcal{L}_{Yl} , the mass term arises

$$\mathcal{L}_{Yl} = -m_l (\bar{l}_L l_R + \bar{l}_R l_L) - \frac{m_l}{v} (\bar{l}_L l_R + \bar{l}_R l_L) H = -m_l \bar{l} \left(1 + \frac{H}{v} \right) \quad (2.49)$$

700

$$m_l = \frac{G_l}{\sqrt{2}} v \quad (2.50)$$

701 where the additional term represents the lepton-Higgs interaction. The quark masses
 702 are generated in a similar way as lepton masses but for the upper member of the
 703 quark doublet a different Higgs doublet is needed:

$$\phi_c = -i\sigma_2 \phi^* = \begin{pmatrix} -\bar{\phi}^0 \\ \phi^- \end{pmatrix}. \quad (2.51)$$

704 Additionally, given that the quark isospin doublets are not constructed in terms
 705 of the mass eigenstates but in terms of the flavor eigenstates, as shown in Table 2.5,
 706 the coupling parameters will be related to the CKM matrix elements; thus, the quark
 707 Lagrangian is given by:

$$\mathcal{L}_{Yq} = -G_d^{i,j} (\bar{u}_i, \bar{d}'_i)_L \begin{pmatrix} \phi^+ \\ \phi^0 \end{pmatrix} d_{jR} - G_u^{i,j} (\bar{u}_i, \bar{d}'_i)_L \begin{pmatrix} -\bar{\phi}^0 \\ \phi^- \end{pmatrix} u_{jR} + h.c. \quad (2.52)$$

708 with $i, j = 1, 2, 3$. After SSB and expansion about the ground state, the diagonal form

709 of \mathcal{L}_{Yq} is:

$$\mathcal{L}_{Yq} = -m_d^i \bar{d}_i d_i \left(1 + \frac{H}{v}\right) - m_u^i \bar{u}_i u_i \left(1 + \frac{H}{v}\right) \quad (2.53)$$

710 Fermion masses depend on arbitrary couplings G_l and $G_{u,d}$ and are not predicted
711 by the theory.

712 2.3.5 The Higgs field

713 After the characterization of the fermions and gauge bosons as well as their interac-
714 tions, it is necessary to characterize the Higgs field itself. The Lagrangian \mathcal{L}_S in Eqn.
715 2.37 written in terms of the gauge bosons is given by

$$\mathcal{L}_S = \frac{1}{4} \lambda v^4 + \mathcal{L}_H + \mathcal{L}_{HV} \quad (2.54)$$

716

$$\mathcal{L}_H = \frac{1}{2} \partial_\mu H \partial^\mu H - \frac{1}{2} m_H^2 H^2 - \frac{1}{2v} m_H^2 H^3 - \frac{1}{8v^2} m_H^2 H^4 \quad (2.55)$$

717

$$\mathcal{L}_{HV} = m_H^2 W_\mu^+ W^{\mu-} \left(1 + \frac{2}{v} H + \frac{2}{v^2} H^2\right) + \frac{1}{2} m_Z^2 Z_\mu Z^\mu \left(1 + \frac{2}{v} H + \frac{2}{v^2} H^2\right) \quad (2.56)$$

718 The mass of the Higgs boson is deduced as usual from the mass term in the Lagrangian
719 resulting in:

$$m_H = \sqrt{-2\mu^2} = \sqrt{2\lambda}v \quad (2.57)$$

720 however, it is not predicted by the theory either. The experimental measurement of
721 the Higgs boson mass have been performed by the *Compact Muon Solenoid (CMS)*
722 experiment and the *A Toroidal LHC Appartus (ATLAS)* experiments at the *Large
723 Hadron Collider (LHC)*, [36–38], and is presented in Table 2.8.

724

Property	Value
Electric charge	0
Color charge	0
Spin	0
Weak isospin	-1/2
Weak hypercharge	1
Parity	1
Mass (GeV/c^2)	$125.09 \pm 0.21 \text{ (stat.)} \pm 0.11 \text{ (syst.)}$

Table 2.8: Higgs boson properties. Higgs mass is not predicted by the theory and the value here corresponds to the experimental measurement.

2.3.6 Production of Higgs bosons at LHC

At the LHC, Higgs bosons are produced as a result of the collision of two counter-rotating protons beams. A detailed description of the LHC machine will be presented in chapter 3.

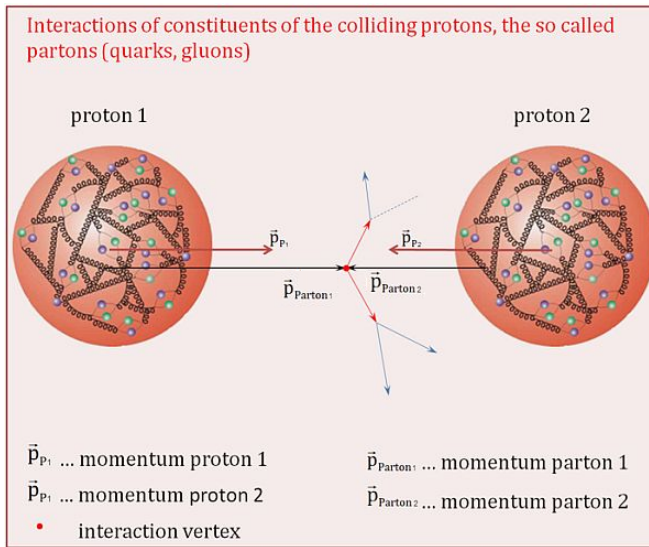


Figure 2.10: Proton-proton collision. Protons are composed of 3 valence quarks, a sea of quarks and gluons; therefore in a proton-proton collision, quarks and gluons are those who collide. [39].

728

729 Protons are composed of quarks and these quarks are bound by gluons; however,
730 what is commonly called the quark content of the proton makes reference to the
731 valence quarks. In fact, a proton is not just a rigid entity with three balls in it all
732 tied up with springs, but the gluons exchanged by the valence quarks tend to split

733 spontaneously into quark-antiquark pairs or more gluons, creating *sea of quarks and*
 734 *gluons* as represented in Figure 2.10.

735 In a proton-proton (pp) collision, the proton's constituents, quarks and gluons, are
 736 those that collide. The pp cross section depends on the momentum of the colliding
 737 particles, reason for which it is needed to know how the momentum is distributed
 738 inside the proton. Quarks and gluons are known as partons, hence, the functions
 739 that describe how the proton momentum is distributed among partons inside it are
 740 called *parton distribution functions (PDFs)*; PDFs are determined from experimental
 741 data obtained in experiments where the internal structure of hadrons is tested, and
 742 depend on the momentum transfer Q and the fraction of momentum x carried by an
 743 specific parton. Figure 2.11 shows the proton PDFs ($xf(x, Q^2)$) for two values of Q .

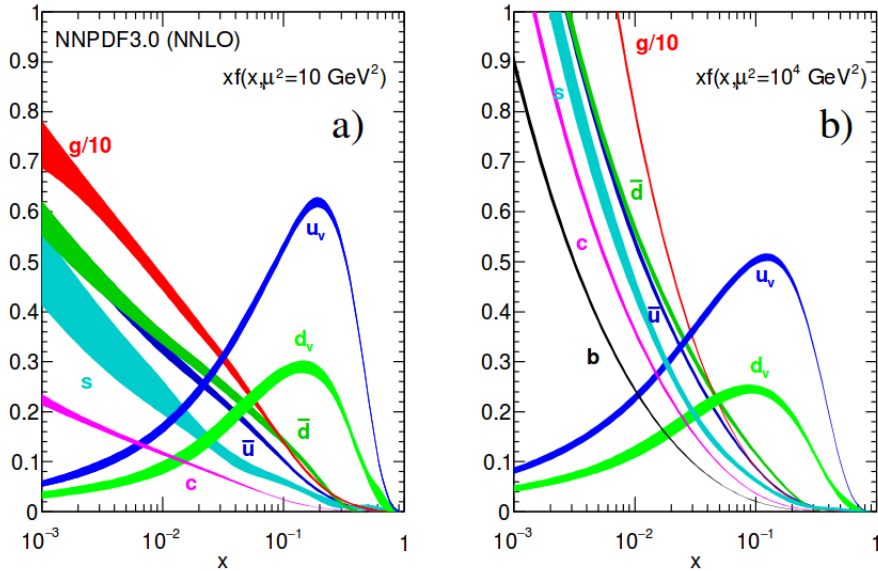


Figure 2.11: Proton PDFs for two values of Q^2 : left. $\mu^2 = Q^2 = 10 \text{ GeV}^2$, right. $\mu^2 = Q^2 = 10^4 \text{ GeV}^2$. u_v and d_v correspond to the u and d valence quarks, $s, c, b, \bar{u}, \bar{d}$ correspond to sea quarks, and g corresponds to gluons. Note that gluons carry a high fraction of the proton's momentum. [9]

744 In physics, a common approach to study complex systems consists of starting
 745 with a simpler version of them, for which a well known description is available, and

adding an additional *perturbation* which represents a small deviation from the known behavior. If the perturbation is small enough, the physical quantities associated with the perturbed system are expressed as a series of corrections to those of the simpler system. The perturbation series corresponds to an expansion in power series of a small parameter, therefore, the more terms are considered in the series (the higher order in the perturbation series), the more precise is the description of the complex system. If the perturbation does not get progressively smaller, the strategy cannot be applied and new methods have to be employed.

High energy systems, like the Higgs production at LHC explored in this thesis, usually can be treated perturbatively with the expansion made in terms of the coupling constants. The overview presented here will be oriented specifically to the Higgs boson production mechanisms in pp collisions at LHC.

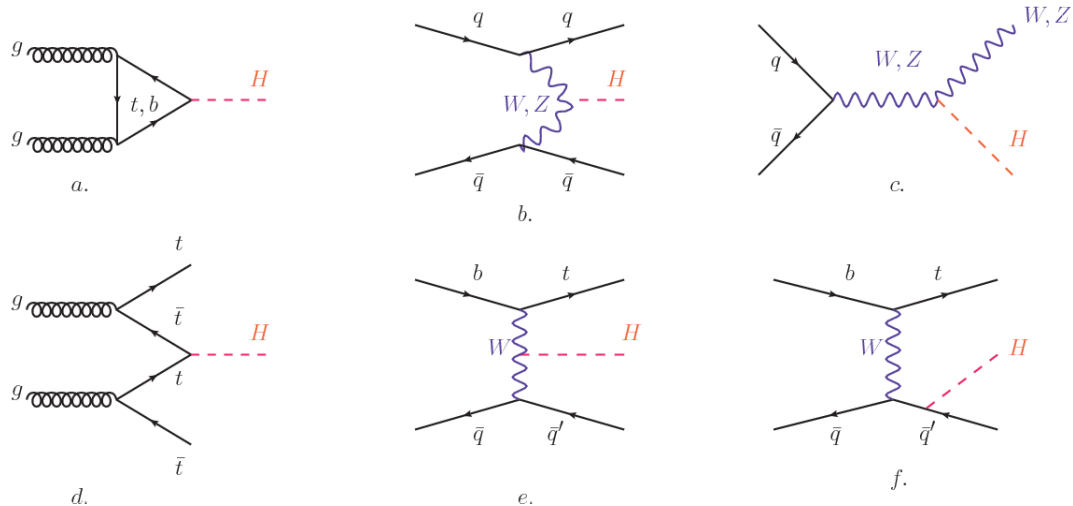


Figure 2.12: Main Higgs boson production mechanism Feynman diagrams. a. gluon-gluon fusion, b. vector boson fusion (VBF), c. Higgs-strahlung, d. Associated production with a top or bottom quark pair, e-f. associated production with a single top quark.

Figure 2.12 shows the Feynman diagrams for the leading order (first order) Higgs production processes at LHC; note that in these diagrams the incoming particles are not the protons themselves but the partons from the protons that actually participate

in the interaction, hence, theorists typically calculate the cross section for the parton interaction, and then convolute that cross section with the information from the PDFs to get a production cross section that is actually measured in experiments. The cross section for Higgs production as a function of the center of mass-energy (\sqrt{s}) for pp collisions is showed in Figure 2.13 left. The tags NLO (next to leading order), NNLO (next to next to leading order) and N3LO (next to next to next to leading order) make reference to the order at which the perturbation series have been considered while the tags QCD and EW correspond to the strong and electroweak coupling constants respectively.

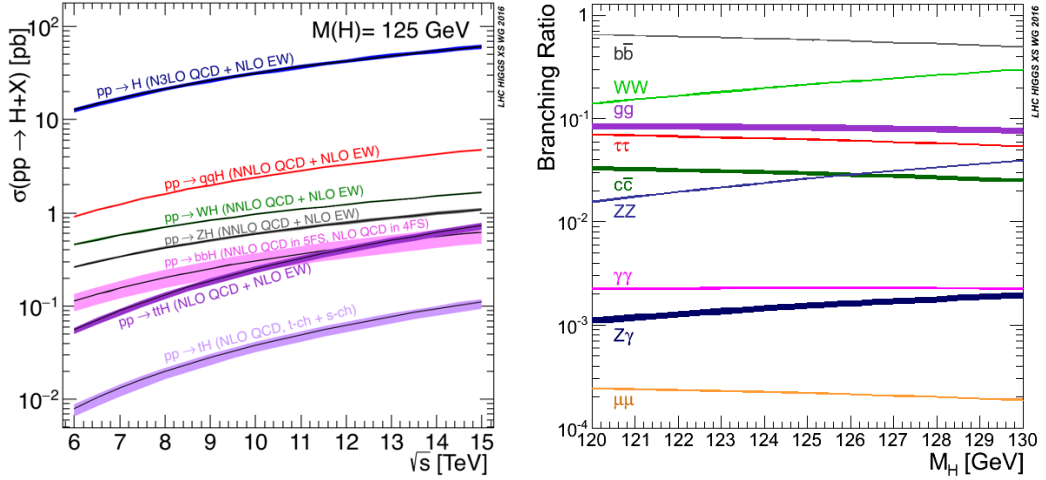


Figure 2.13: Higgs boson production cross sections (left) and decay branching ratios (right) for the main mechanisms. The VBF is indicated as qqH [40].

The main production mechanism is the gluon fusion (Figure 2.12a and $pp \rightarrow H$ in Figure 2.13) given that gluons carry the highest fraction of momentum of the protons in pp colliders (as shown in Figure ??). Since the Higgs boson does not couple to gluons, the mechanism proceeds through the exchange of a virtual top-quark loop. Note that in this process the Higgs boson is produced alone, turning out to be problematic for some Higgs decays, because such absence of anything produced in

776 association with the Higgs represent a trouble for triggering, however, this mechanism
 777 is experimentally clean when combined with the two-photon or the four-lepton decay
 778 channels (see Section 2.3.7).

779 Vector boson fusion (Figure 2.12b and $pp \rightarrow qqH$ in Figure 2.13) has the second
 780 largest production cross section. The scattering of two fermions is mediated by a weak
 781 gauge boson which later emits a Higgs boson. In the final state, the two fermions tend
 782 to be located in the central region of the detector; this kind of features are generally
 783 used as a signature when analyzing the datasets provided by the experiments⁷.

784 In the Higgs-strahlung mechanism (Figure 2.12c and $pp \rightarrow WH, pp \rightarrow ZH$ in
 785 Figure 2.13) two fermions annihilate to form a weak gauge boson. If the initial
 786 fermions have enough energy, the emergent boson might emit a Higgs boson.

787 The associated production with a top or bottom quark pair and the associated
 788 production with a single top quark (Figure 2.12d-f and $pp \rightarrow bbH, pp \rightarrow t\bar{t}H, pp \rightarrow tH$
 789 in Figure 2.13) have a smaller cross section than the main three mechanisms above,
 790 but they provide a good opportunity to test the Higgs-top coupling. The analysis
 791 reported in this thesis is developed using these production mechanisms. A detailed
 792 description of the tH mechanism will be given in Section 2.5.

793 2.3.7 Higgs boson decay channels

794 When a particle can decay through several modes, also known as channels, the prob-
 795 ability of decaying through a given channel is quantified by the *branching ratio (BR)*
 796 of the decay channel; thus, the BR is defined as the ratio of number of decays go-
 797 ing through that given channel to the total number of decays. In regard to the
 798 Higgs boson decay, the BR can be predicted with accuracy once the Higgs mass is
 799 known [41, 42]. In Figure 2.13 right, a plot of the BR as a function of the Higgs mass

⁷ More details about how to identify events of interest in this analysis will be given in chapter 6.

is presented; the largest predicted BR corresponds to the $b\bar{b}$ pair decay channel (see Table 2.9) given that it is the heaviest particle pair whose on-shell⁸ production is kinematically allowed in the decay.

Decay channel	Branching ratio	Rel. uncertainty
$H \rightarrow b\bar{b}$	5.84×10^{-1}	$+3.2\% - 3.3\%$
$H \rightarrow W^+W^-$	2.14×10^{-1}	$+4.3\% - 4.2\%$
$H \rightarrow \tau^+\tau^-$	6.27×10^{-2}	$+5.7\% - 5.7\%$
$H \rightarrow ZZ$	2.62×10^{-2}	$+4.3\% - 4.1\%$
$H \rightarrow \gamma\gamma$	2.27×10^{-3}	$+5.0\% - 4.9\%$
$H \rightarrow Z\gamma$	1.53×10^{-3}	$+9.0\% - 8.9\%$
$H \rightarrow \mu^+\mu^-$	2.18×10^{-4}	$+6.0\% - 5.9\%$

Table 2.9: Predicted branching ratios and the relative uncertainty for some decay channels of a SM Higgs boson with $m_H = 125\text{GeV}/c^2$ [9]; the uncertainties are driven by theoretical uncertainties for the different Higgs boson partial widths and by parametric uncertainties associated to the strong coupling and the masses of the quarks which are the input parameters. Further details on these calculations can be found in Reference [43]

803

804 Decays to other lepton and quark pairs, like electron, strange, up, and down
 805 quark pairs not listed in the table, are also possible but their likelihood is too small
 806 to measure since they are very lightweight, hence, their interaction with the Higgs
 807 boson is very weak. On other hand, the decay to top quark pairs is heavily suppressed
 808 due to the top quark mass ($\approx 173\text{ GeV}/c^2$).

809 Decays to gluons proceed indirectly through a virtual top quark loop while the
 810 decays to photons proceed through a virtual W boson loop, therefore, their branching
 811 ratio is smaller compared to direct interaction decays. Same is true for the decay to
 812 a photon and a Z boson.

⁸ In general, on-shell or real particles are those which satisfy the energy-momentum relation ($E^2 - |\vec{p}|^2 c^2 = m^2 c^4$); off-shell or virtual particles does not satisfy it which is possible under the uncertainty principle of quantum mechanics. Usually, virtual particles correspond to internal propagators in Feynman diagrams.

813 In the case of decays to pairs of W and Z bosons, the decay proceed with one of
 814 the bosons being on-shell and the other being off-shell. The likelihood of the process
 815 diminish depending on how far off-shell are the virtual particles involved, hence, the
 816 branching ratio for W boson pairs is bigger than for Z boson pairs since Z boson mass
 817 is bigger than W boson mass.

818 Note that the decay to a pair of virtual top quarks is possible, but the probability
 819 is way too small.

820 **2.4 Experimental status of the anomalous**
 821 **Higgs-fermion coupling**

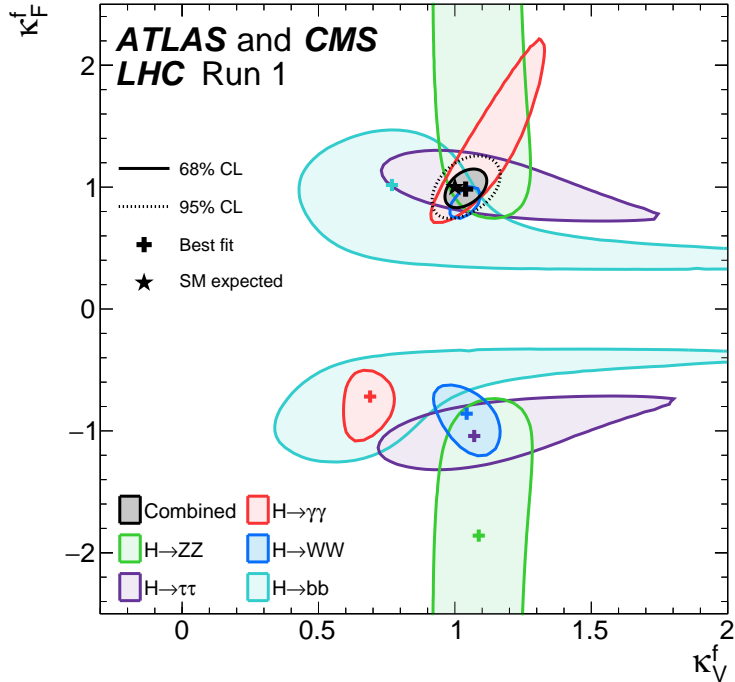


Figure 2.14: Combination of the ATLAS and CMS fits for coupling modifiers $\kappa_t - \kappa_V$; also shown the individual decay channels combination and their global combination. No assumptions have been made on the sign of the coupling modifiers [44].

822 ATLAS and CMS have performed analyses of the anomalous Higgs-fermion cou-
 823 pling by making likelihood scans for the two coupling modifiers, κ_f and κ_V , under
 824 the assumption that $\kappa_Z = \kappa_W \equiv \kappa_V$ and $\kappa_t = \kappa_\tau = \kappa_b \equiv \kappa_f$. Figure 2.14 shows the
 825 result of the combination of ATLAS and CMS fits; also the individual decay channels
 826 combination and the global combination results are shown. Note that from this plot
 827 there is limited information on the sign of the coupling since the only information
 828 available about the sign of the coupling comes from decays rather than production.

829 While all the channels are compatible for positive values of the modifiers, for
 830 negative values of κ_f there is no compatibility. The best fit for individual channels
 831 is compatible with negative values of κ_f except for the $H \rightarrow bb$ channel. The best
 832 fit for the combination yields $\kappa_f \geq 0$, in contrast to the yields from the individual
 833 channels; the reason of this yield resides in the $H \rightarrow \gamma\gamma$ coupling. $H \rightarrow \gamma\gamma$ decay
 834 proceeds through a loop of either top quarks or W bosons, hence, this channel is
 835 sensitive to κ_t thanks to the interference of these two amplitude contributions; under
 836 the assumption that no beyond SM particles take part in the loops, a flipped sign
 837 of κ_t will increase the $H \rightarrow \gamma\gamma$ branching fraction by a factor of ~ 2.4 which is not
 838 supported by measurements; thus, this large asymmetry between the positive and
 839 negative coupling ratios in the $H \rightarrow \gamma\gamma$ channel drives the yield of the global fit and
 840 would mean that the anomalous H-t coupling is excluded as stated in Reference [44],
 841 but there is a caveat, this exclusion holds only if no new particles contribute to the
 842 loop in the main diagram for that decay.

843 Although the $H \rightarrow bb$ channel is expected to be the most sensitive channel and
 844 its best fit value of κ_t is positive, and then the global fit yield is still supported,
 845 the contributions from all the other decay channels, small compared to the $H \rightarrow bb$,
 846 indicate that the anomalous H-t coupling cannot be excluded completely, motivating
 847 to look at tH processes which can help with both, the limited information on the sign

848 of the H-t coupling and the access to information from the Higgs boson production
 849 rather than from its decays.

850 It will be shown in Section 2.5 that the same interference effect enhance the
 851 tH production rate and could reveal evidence of direct production of heavy new par-
 852 ticles as predicted in composite and little Higgs models [45], or new physics related
 853 to Higgs boson mediated flavor changing neutral currents [46] as well as probes the
 854 CP-violating phase of the H-t coupling [47, 48].

855 **2.5 Associated production of a Higgs boson and a 856 single top quark**

857 The production of Higgs boson in association with a top quark has been extensively
 858 studied [47, 49–52]. While measurements of the main Higgs production mechanisms
 859 rates are sensitive to the strength of the Higgs coupling to W boson or top quark,
 860 they are not sensitive to the relative sign between the two couplings. In this thesis,
 861 the Higgs boson production mechanism explored is the associated production with a
 862 single top quark (tH) which offers sensitivity to the relative sign of the Higgs couplings
 863 to W boson and to top quark. The description given here is based on Reference [51]

A process where two incoming particles interact and produce a final state with two
 particles can proceed in three called channels (see, for instance, Figure 2.15 omitting
 the red line). The t-channel represents processes where an intermediate particle is
 emitted by one of the incoming particles and absorbed by the other. The s-channel
 represents processes where the two incoming particles merge into an intermediate par-
 ticle which eventually will split into the particles in the final state. The third channel,
 u-channel, is similar to the t-channel but the two outgoing particles interchange their

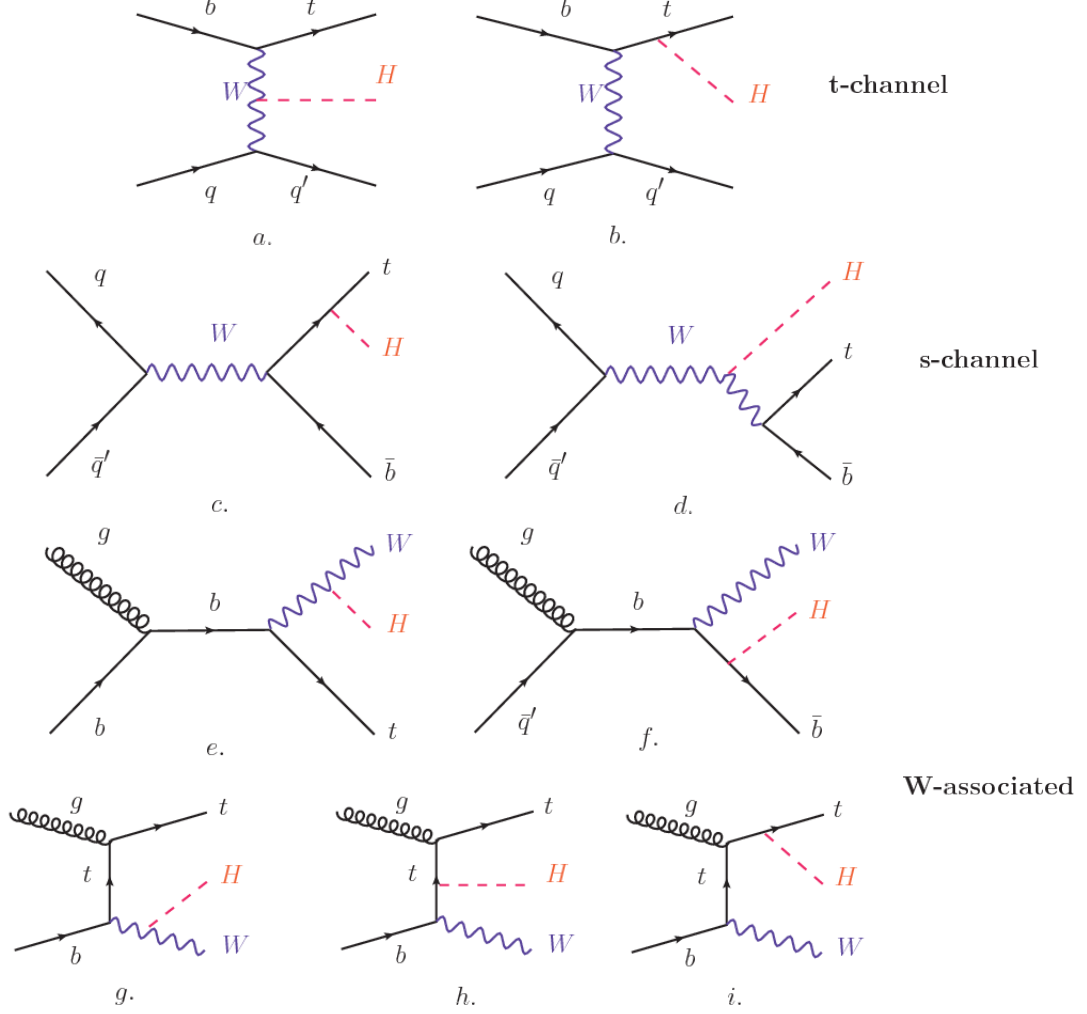


Figure 2.15: Associated Higgs boson production with a top quark mechanism Feynman diagrams. a.,b. t-channel (tHq), c.,d. s-channel (tHb), e-i. W-associated.

roles. These three channels are connected to the so-called Mandelstam variables

$$s = (p_1 + p_2)^2 = (p'_1 + p'_2)^2 \rightarrow \text{square of the center mass-energy.} \quad (2.58)$$

$$t = (p_1 - p'_1)^2 = (p'_2 - p_2)^2 \rightarrow \text{square of the four-momentum transfer.} \quad (2.59)$$

$$u = (p_1 - p'_2)^2 = (p'_1 - p_2)^2 \rightarrow \text{square of the crossed four-momentum transfer.} \quad (2.60)$$

$$s + t + u = m_1^2 + m_2^2 + m'_1{}^2 + m'_2{}^2 \quad (2.61)$$

which relate the momentum, energy and the angles of the incoming and outgoing particles in an scattering process of two particles to two particles. The importance of the Mandelstam variables reside in that they form a minimum set of variables needed to describe the kinematics of this scattering process; they are Lorentz invariant which makes them very useful when doing calculations.

The tH production, where Higgs boson can be radiated either from the top quark or from the W boson, is represented by the leading order Feynman diagrams in Figure 2.15. The cross section for the tH process is calculated, as usual, summing over the contributions from the different Feynman diagrams; therefore it depends on the interference between the contributions. In the SM, the interference for t-channel (tHq process) and W-associated (tHW process) production is destructive [49] resulting in the small cross sections presented in Table 2.10.

tH production channel	Cross section (fb)
t-channel ($pp \rightarrow tHq$)	$70.79^{+2.99}_{-4.80}$
W-associated ($pp \rightarrow tHW$)	$15.61^{+0.83}_{-1.04}$
s-channel($pp \rightarrow tHb$)	$2.87^{+0.09}_{-0.08}$

Table 2.10: Predicted SM cross sections for tH production at $\sqrt{s} = 13$ TeV [53, 54].

876

The s-channel contribution can be neglected. It will be shown that a deviation from the SM destructive interference would result in an enhancement of the tH cross section compared to that in SM, which could be used to get information about the sign of the Higgs-top coupling [51, 52]. In order to describe tH production processes, Feynman diagram 2.15b will be considered; there, the W boson is radiated by a quark in the proton and eventually it will interact with the b quark. In the high energy regime, the effective W approximation [55] is used to describe the process as the

884 emission of an approximately on-shell W and its hard scattering with the b quark;
 885 i.e. $Wb \rightarrow th$. The scattering amplitude for the process is given by

$$\mathcal{A} = \frac{g}{\sqrt{2}} \left[(\kappa_t - \kappa_V) \frac{m_t \sqrt{s}}{m_W v} A \left(\frac{t}{s}, \varphi; \xi_t, \xi_b \right) + \left(\kappa_V \frac{2m_W s}{v t} + (2\kappa_t - \kappa_V) \frac{m_t^2}{m_W v} \right) B \left(\frac{t}{s}, \varphi; \xi_t, \xi_b \right) \right], \quad (2.62)$$

886 where $\kappa_V \equiv g_{HVV}/g_{HVV}^{SM}$ and $\kappa_t \equiv g_{Ht}/g_{Ht}^{SM} = y_t/y_t^{SM}$ are scaling factors that quantify
 887 possible deviations of the couplings from the SM values, Higgs-Vector boson (H-
 888 W) and Higgs-top (H-t) respectively, from the SM couplings; $s = (p_W + p_b)^2$, $t =$
 889 $(p_W - p_H)^2$, φ is the Higgs azimuthal angle around the z axis taken parallel to the
 890 direction of motion of the incoming W; A and B are functions describing the weak
 891 interaction in terms of the chiral states (ξ_t, ξ_b) of the quarks b and t . Terms that
 892 vanish in the high energy limit have been neglected as well as the Higgs and b quark
 893 masses⁹.

894 The scattering amplitude grows with energy like \sqrt{s} for $\kappa_V \neq \kappa_t$, in contrast to
 895 the SM ($\kappa_t = \kappa_V = 1$), where the first term in 2.62 cancels out and the amplitude
 896 is constant for large s ; therefore, a deviation from the SM predictions represents an
 897 enhancement in the tHq cross section. In particular, for a SM H-W coupling and a
 898 H-t coupling of inverted sign with respect to the SM ($\kappa_V = -\kappa_t = 1$) the tHq cross
 899 section is enhanced by a factor greater 10 as seen in the Figure 2.16 taken from
 900 Reference [51]; Reference [56] has reported similar enhancement results.

901 A similar analysis is valid for the W-associated channel but, in that case, the in-
 902 terference is more complicated since there are more than two contributions and an ad-
 903 ditional interference with the production of Higgs boson and a top pair process($t\bar{t}H$).
 904 The calculations are made using the so-called Diagram Removal (DR) technique where

⁹ A detailed explanation of the structure and approximations used to derive \mathcal{A} can be found in Reference [51]

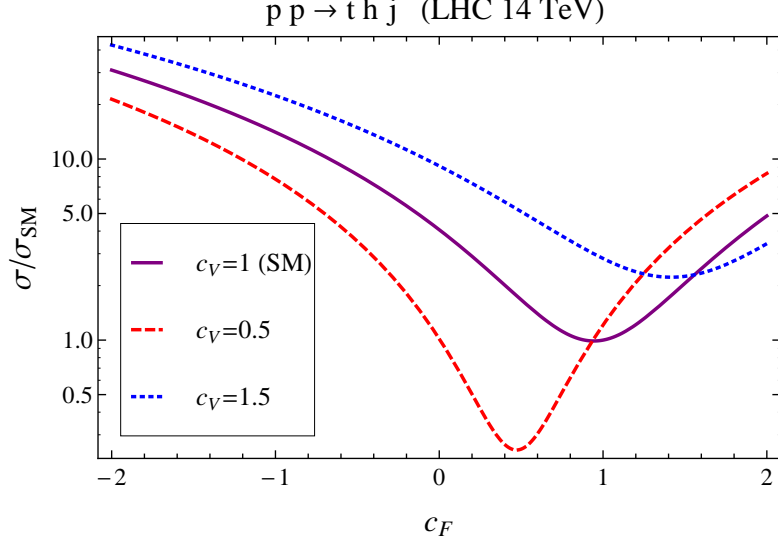


Figure 2.16: Cross section for tHq process as a function of κ_t , normalized to the SM, for three values of κ_V . In the plot c_f refers to the Higgs-fermion coupling which is dominated by the H-t coupling and represented here by κ_t . Solid, dashed and dotted lines correspond to $c_V \rightarrow \kappa_V = 1, 0.5, 1.5$ respectively. Note that for the SM ($\kappa_V = \kappa_t = 1$), the destructive effect of the interference is maximal.

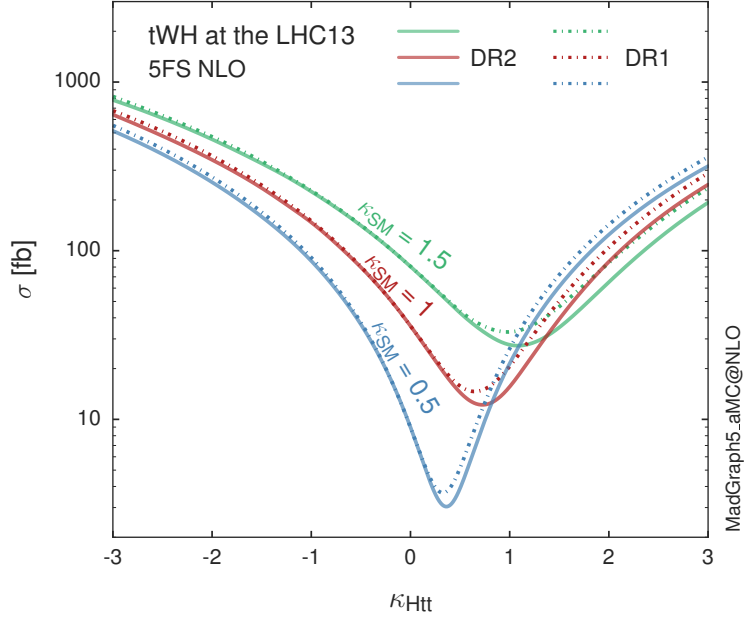


Figure 2.17: Cross section for tHW process as a function of κ_{Htt} , for three values of κ_{SM} at $\sqrt{s} = 13$ TeV. $\kappa_{Htt}^2 = \sigma_{Htt}/\sigma_{Htt}^{SM}$ is a simple re-scaling of the SM Higgs interactions.

905 interfering diagrams are removed (or added) from the calculations in order to evaluate
 906 the impact of the removed contributions. DR1 was defined to neglect $t\bar{t}H$ interfer-
 907 ence while DR2 was defined to take $t\bar{t}H$ interference into account [48]. As shown in
 908 Figure 2.17, the tHW cross section is enhanced from about 15 fb (SM: $\kappa_{Htt} = 1$) to
 909 about 150 fb ($\kappa_{Htt} = -1$). Differences between curves for DR1 and DR2 help to gauge
 910 the impact of the interference with $t\bar{t}H$. Results of the calculations of the tHq and
 911 tHW cross sections at $\sqrt{s} = 13$ TeV can be found in Reference [57] and a summary of
 912 the results is presented in Table 2.11.

	\sqrt{s} TeV	$\kappa_t = 1$	$\kappa_t = -1$
$\sigma^{LO}(tHq)(fb)$ [51]	8	≈ 17.4	≈ 252.7
	14	≈ 80.4	≈ 1042
$\sigma^{NLO}(tHq)(fb)$ [51]	8	$18.28^{+0.42}_{-0.38}$	$233.8^{+4.6}_{-0.0}$
	14	$88.2^{+1.7}_{-0.0}$	$982.8^{+28}_{-0.0}$
$\sigma^{LO}(tHq)(fb)$ [56]	14	≈ 71.8	≈ 893
$\sigma^{LO}(tHW)(fb)$ [56]	14	≈ 16.0	≈ 139
$\sigma^{NLO}(tHq)(fb)$ [57]	8	$18.69^{+8.62\%}_{-17.13\%}$	-
	13	$74.25^{+7.48\%}_{-15.35\%}$	$848^{+7.37\%}_{-13.70\%}$
	14	$90.10^{+7.34\%}_{-15.13\%}$	$1011^{+7.24\%}_{-13.39\%}$
$\sigma^{LO}(tHW)(fb)$ [48]	13	$15.77^{+15.91\%}_{-15.76\%}$	-
$\sigma^{NLO}DR1(tHW)(fb)$ [48]	13	$21.72^{+6.52\%}_{-5.24\%}$	≈ 150
$\sigma^{NLO}DR2(tHW)(fb)$ [48]	13	$16.28^{+7.34\%}_{-15.13\%}$	≈ 150

Table 2.11: Predicted enhancement of the tHq and tHW cross sections at LHC for $\kappa_V = 1$ and $\kappa_t = \pm 1$ at LO and NLO; the cross section enhancement of more than a factor of 10 is due to the flipping in the sign of the H-t coupling with respect to the SM one.

913

914 2.6 CP-mixing in tH processes

915 In addition to the sensitivity to sign of the H-t coupling, the tHq and tHW processes
 916 have been proposed as a tool to investigate the possibility of a H-t coupling that does

917 not conserve CP [47, 48, 58].

918 In this thesis, the sensitivity of tH processes to CP-mixing is also studied on the
 919 basis of References [47, 48] using the effective field theory framework where a generic
 920 particle (X_0) of spin-0 and a general CP violating interaction with the top quark
 921 (Htt coupling), can couple to scalar and pseudo-scalar fermionic densities. The H-W
 922 interaction is assumed to be SM-like. The Lagrangian modeling the H-t interaction
 923 is given by

$$\mathcal{L}_0^t = -\bar{\psi}_t (c_\alpha \kappa_{Htt} g_{Htt} + i s_\alpha \kappa_{Att} g_{Att} \gamma_5) \psi_t X_0, \quad (2.63)$$

924 where α is the CP-mixing phase, $c_\alpha \equiv \cos \alpha$ and $s_\alpha \equiv \sin \alpha$, κ_{Htt} and κ_{Att} are real
 925 dimensionless re-scaling parameters¹⁰ used to parametrize the magnitude of the CP-
 926 violating and CP-conserving parts of the amplitude. The model defines $g_{Htt} =$
 927 $g_{Att} = m_t/v = y_t/\sqrt{2}$ with $v \sim 246$ GeV the Higgs vacuum expectation value. In
 928 this parametrization, three special cases can be recovered

929 • CP-even coupling $\rightarrow \alpha = 0^\circ$

930 • CP-odd coupling $\rightarrow \alpha = 90^\circ$

931 • SM coupling $\rightarrow \alpha = 0^\circ$ and $\kappa_{Htt} = 1$

932 The loop induced X_0 coupling to gluons can also be described in terms of the
 933 parametrization above, according to

$$\mathcal{L}_0^g = -\frac{1}{4} \left(c_\alpha \kappa_{Hgg} g_{Hgg} G_{\mu\nu}^a G^{a,\mu\nu} + s_\alpha \kappa_{Agg} g_{Agg} G_{\mu\nu}^a \tilde{G}^{a,\mu\nu} \right) X_0. \quad (2.64)$$

934 where $g_{Hgg} = -\alpha_s/3\pi v$ and $g_{Agg} = \alpha_s/2\pi v$ and $G_{\mu\nu}$ is the gluon field strength tensors.

935 Under the assumption that the top quark dominates the gluon-fusion process at LHC

¹⁰ analog to κ_t and κ_V

936 energies, $\kappa_{Hgg} \rightarrow \kappa_{Htt}$ and $\kappa_{Agg} \rightarrow \kappa_{Att}$, so that the ratio between the gluon-gluon
 937 fusion cross section for X_0 and for the SM Higgs prediction can be written as

$$\frac{\sigma_{NLO}^{gg \rightarrow X_0}}{\sigma_{NLO,SM}^{gg \rightarrow H}} = c_\alpha^2 \kappa_{Htt}^2 + s_\alpha^2 \left(\kappa_{Att} \frac{g_{Agg}}{g_{Hgg}} \right)^2. \quad (2.65)$$

938 If the re-scaling parameters are set to

$$\kappa_{Htt} = 1, \quad \kappa_{Att} = \left| \frac{g_{Hgg}}{g_{Agg}} \right| = \frac{2}{3}. \quad (2.66)$$

939 the gluon-fusion SM cross section is reproduced for every value of the CP-mixing
 940 angle α ; therefore, by imposing that condition to the Lagrangian density 2.63, the
 941 CP-mixing angle is not constrained by current data. Figure 2.18 shows the NLO cross
 942 sections for t-channel tX_0 (blue) and $t\bar{t}X_0$ (red) associated production processes as a
 943 function of the CP-mixing angle α . X_0 is a generic spin-0 particle with top quark
 944 CP-violating coupling. Re-scaling factors κ_{Htt} and κ_{Att} have been set to reproduce
 945 the SM gluon-fusion cross sections.

946 It is interesting to notice that the tX_0 cross section is enhanced, by a factor of
 947 about 10, when a continuous rotation in the scalar-pseudoscalar plane is applied; this
 948 enhancement is similar to the enhancement produced when the H-t coupling is flipped
 949 in sign with respect to the SM ($y_t = -y_{t,SM}$ in the plot), as showed in Section 2.5. In
 950 contrast, the degeneracy in the $t\bar{t}X_0$ cross section is still present given that it depends
 951 quadratically on the H-t coupling, but more interesting is to notice that $t\bar{t}X_0$ cross
 952 section is exceeded by tX_0 cross section after $\alpha \sim 60^\circ$.

953 A similar parametrization can be used to investigate the tHW process sensitivity
 954 to CP-violating H-t coupling. As said in 2.5, the interference in the W-associated
 955 channel is more complicated because there are more than two contributions and also
 956 there is interference with the $t\bar{t}H$ production process.

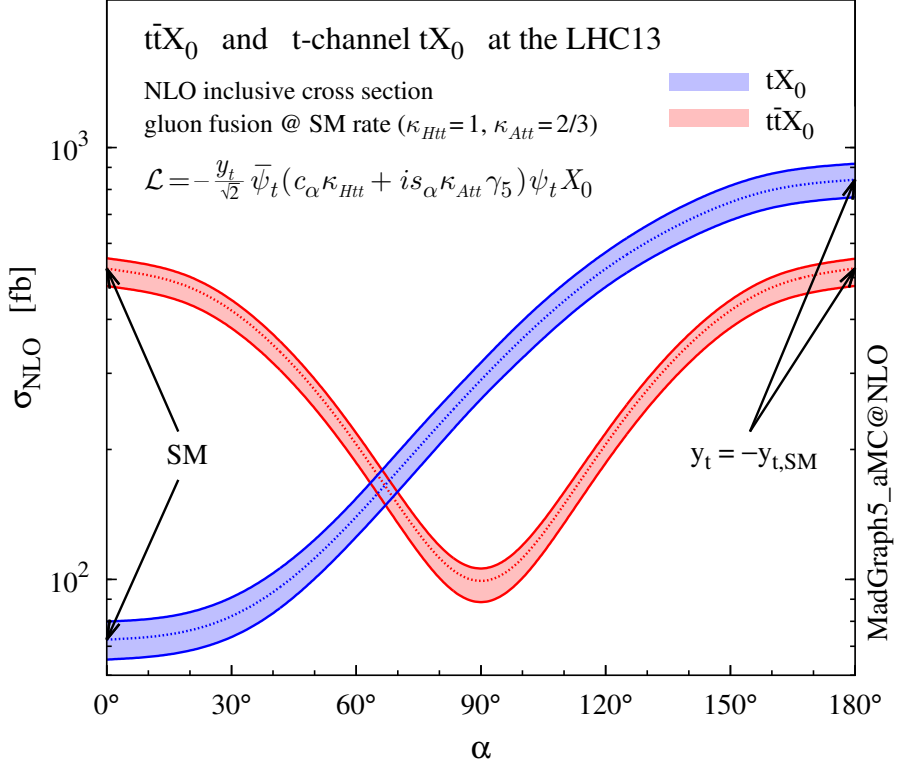


Figure 2.18: NLO cross sections for t-channel tX_0 (blue) and $t\bar{t}X_0$ (red) associated production processes as a function of the CP-mixing angle α . X_0 is a generic spin-0 particle with top quark CP-violating coupling [47].

957 Figure 2.19 shows the NLO cross sections for t-channel tX_0 (blue), $t\bar{t}X_0$ (red)
958 associated production and for the combined $tWX_0+t\bar{t}X_0+interference$ (orange) as
959 a function of the CP-mixing angle. It is clear that the effect of the interference in the
960 combined case is the lifting of the degeneracy present in the $t\bar{t}X_0$ production. The
961 constructive interference enhances the cross section from about 500 fb at SM ($\alpha = 0$)
962 to about 600 fb ($\alpha = 180^\circ \rightarrow y_t = -y_{t,SM}$).

963 An analysis combining tHq and tHW processes will be made in this thesis taking
964 advantage of the sensitivity improvement.

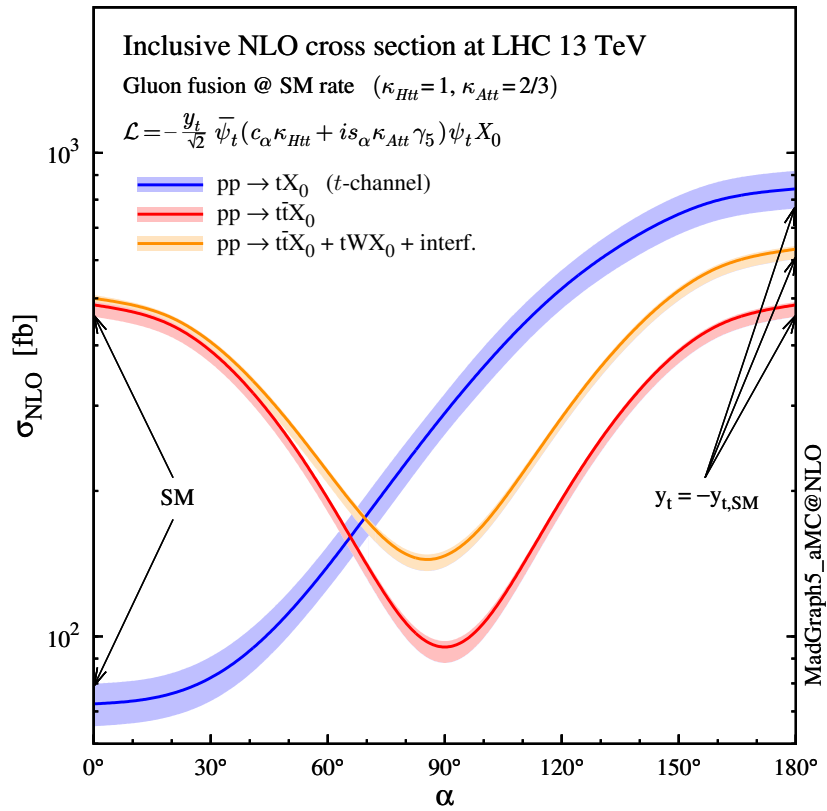


Figure 2.19: NLO cross sections for t-channel tX_0 (blue), $t\bar{t}X_0$ (red) associated production processes and combined $tWX_0 + t\bar{t}X_0$ (including interference) production as a function of the CP-mixing angle α [47].

965 **Chapter 3**

966 **The CMS experiment at the LHC**

967 **3.1 Introduction**

968 Located on the Swiss-French border, the European Council for Nuclear Research
969 (CERN) is the largest scientific organization leading particle physics research. About
970 13000 people in a broad range of roles including users, students, scientists, engineers,
971 among others, contribute to the data taking and analysis, with the goal of unveiling
972 the secrets of nature and revealing the fundamental structure of the universe. CERN
973 is also the home of the Large Hadron Collider (LHC), the largest particle accelerator
974 around the world, where protons (or heavy ions) traveling close to the speed of light,
975 are made to collide. These collisions open a window to investigate how particles (and
976 their constituents if they are composite) interact with each other, providing clues
977 about the laws of nature. This chapter presents an overview of the LHC structure
978 and operation. A detailed description of the CMS detector is offered, given that the
979 data used in this thesis have been taken with this detector.

980 3.2 The LHC

981 With 27 km of circumference, the LHC is currently the most powerful circular accelerator
 982 in the world. It is installed in the same tunnel where the Large Electron-Positron
 983 (LEP) collider was located, taking advantage of the existing infrastructure. The LHC
 984 is part of the CERN's accelerator complex composed of several successive accelerat-
 985 ing stages before the particles are injected into the LHC ring where they reach their
 986 maximum energy (see Figure 3.1).

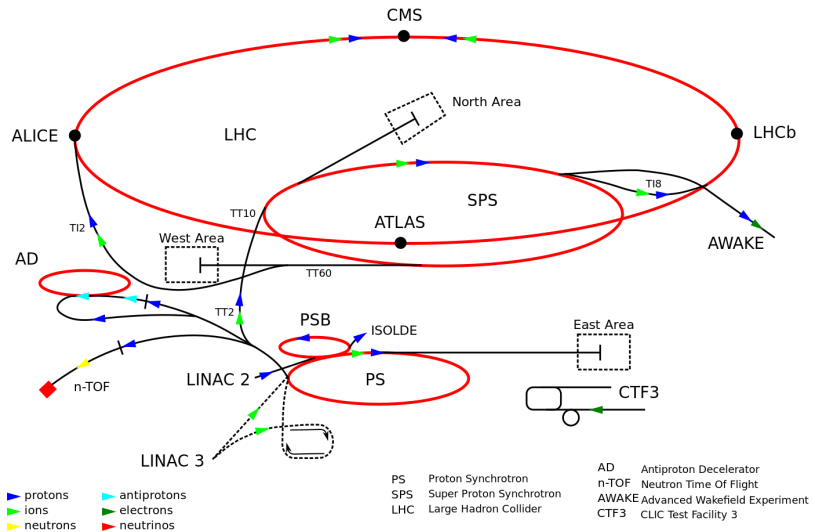


Figure 3.1: CERN accelerator complex. Blue arrows show the path followed by protons along the acceleration process [61].

987 The LHC runs in three collision modes depending on the particles being acceler-
 988 ated

- 989 • Proton-Proton collisions (pp) for multiple physics experiments.
- 990 • Lead-Lead collisions ($Pb-Pb$) for heavy ion experiments.
- 991 • Proton-Lead collisions ($p-Pb$) for quark-gluon plasma experiments.

992 In this thesis only pp collisions will be considered.

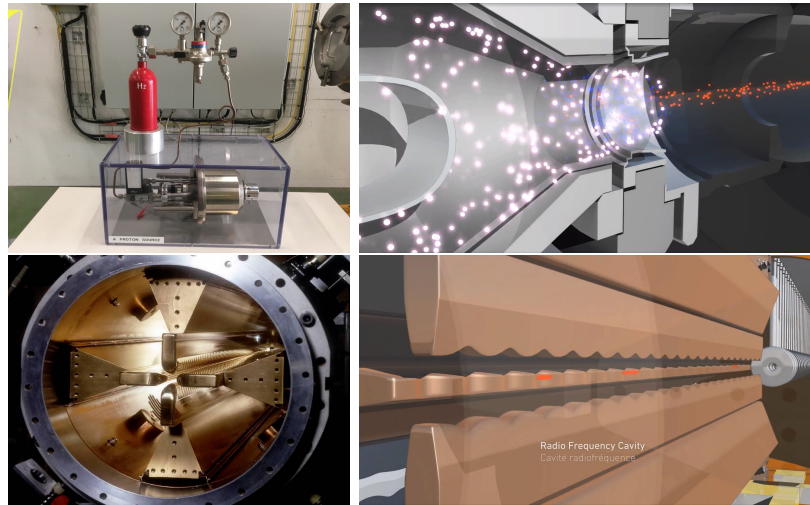


Figure 3.2: LHC protons source and the first acceleration stage. Top: the bottle contains hydrogen gas which is injected into the metal cylinder (white dots) to be broken down into electrons (blue dots) and protons (red dots); Bottom: the obtained protons are directed towards the radio frequency quadrupole which perform the first acceleration, focus the beam and create the bunches of protons. Left images are real pictures while right images are drawings [65, 66].

993 Collection of protons starts with hydrogen atoms taken from a bottle, containing
 994 hydrogen gas, and injecting them in a metal cylinder; hydrogen atoms are broken
 995 down into electrons and protons by an intense electric field (see Figure 3.2 top).
 996 The resulting protons leave the metal cylinder towards a radio frequency quadrupole
 997 (RFQ) that focus the beam, accelerates the protons and creates the packets of protons
 998 called bunches. In the RFQ, an electric field is generated by a RF wave at a frequency
 999 that matches the resonance frequency of the cavity where the electrodes are contained.
 1000 The beam of protons traveling on the RFQ axis experiences an alternating electric
 1001 field gradient that generates the focusing forces.

1002 In order to accelerate the protons, a longitudinal time-varying electric field com-
 1003 ponent is added to the system; it is done by giving the electrodes a sine-like profile as
 1004 shown in Figure 3.2 bottom. By matching the speed and phase of the protons with
 1005 the longitudinal electric field the bunching is performed; protons synchronized with

1006 the RFQ (synchronous protons) do not feel an accelerating force, but those protons in
 1007 the beam that have more (or less) energy than the synchronous proton (asynchronous
 1008 protons) will feel a decelerating (accelerating) force; therefore, asynchronous protons
 1009 will oscillate around the synchronous ones forming bunches of protons [63]. From the
 1010 RFQ protons emerge with energy 750 keV in bunches of about 1.15×10^{11} protons [64].

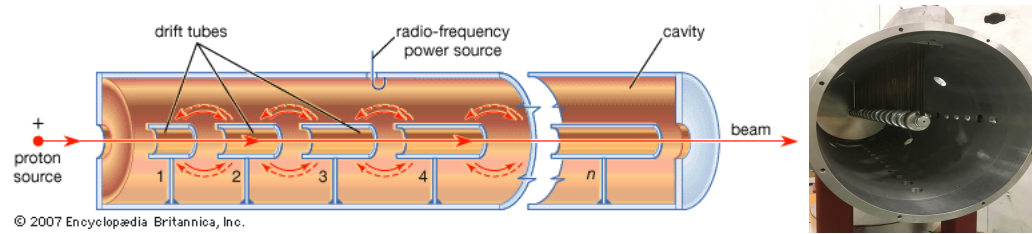


Figure 3.3: Left: drawing of the LINAC2 accelerating system at CERN. Electric fields generated by radio frequency (RF) create acceleration and deceleration zones inside the cavity; deceleration zones are blocked by drift tubes where quadrupole magnets focus the proton beam. Right: picture of a real RF cavity [67].

1011 Proton bunches coming from the RFQ go to the linear accelerator 2 (LINAC2)
 1012 where they are accelerated to reach 50 MeV energy. In the LINAC2 stage, acceleration
 1013 is performed using electric fields generated by radio frequency which create zones
 1014 of acceleration and deceleration as shown in Figure 3.3. In the deceleration zones,
 1015 the electric field is blocked using drift tubes where protons are free to drift while
 1016 quadrupole magnets focus the beam.

1017 The beam coming from LINAC2 is injected into the proton synchrotron booster
 1018 (PSB) to reach 1.4 GeV in energy. The next acceleration is provided at the proton
 1019 synchrotron (PS) up to 26 GeV, followed by the injection into the super proton
 1020 synchrotron (SPS) where protons are accelerated to 450 GeV. Finally, protons are
 1021 injected into the LHC where they are accelerated to the target energy of 6.5 TeV.

1022 PSB, PS, SPS and LHC accelerate protons using the same RF acceleration tech-
 1023 nique described before.

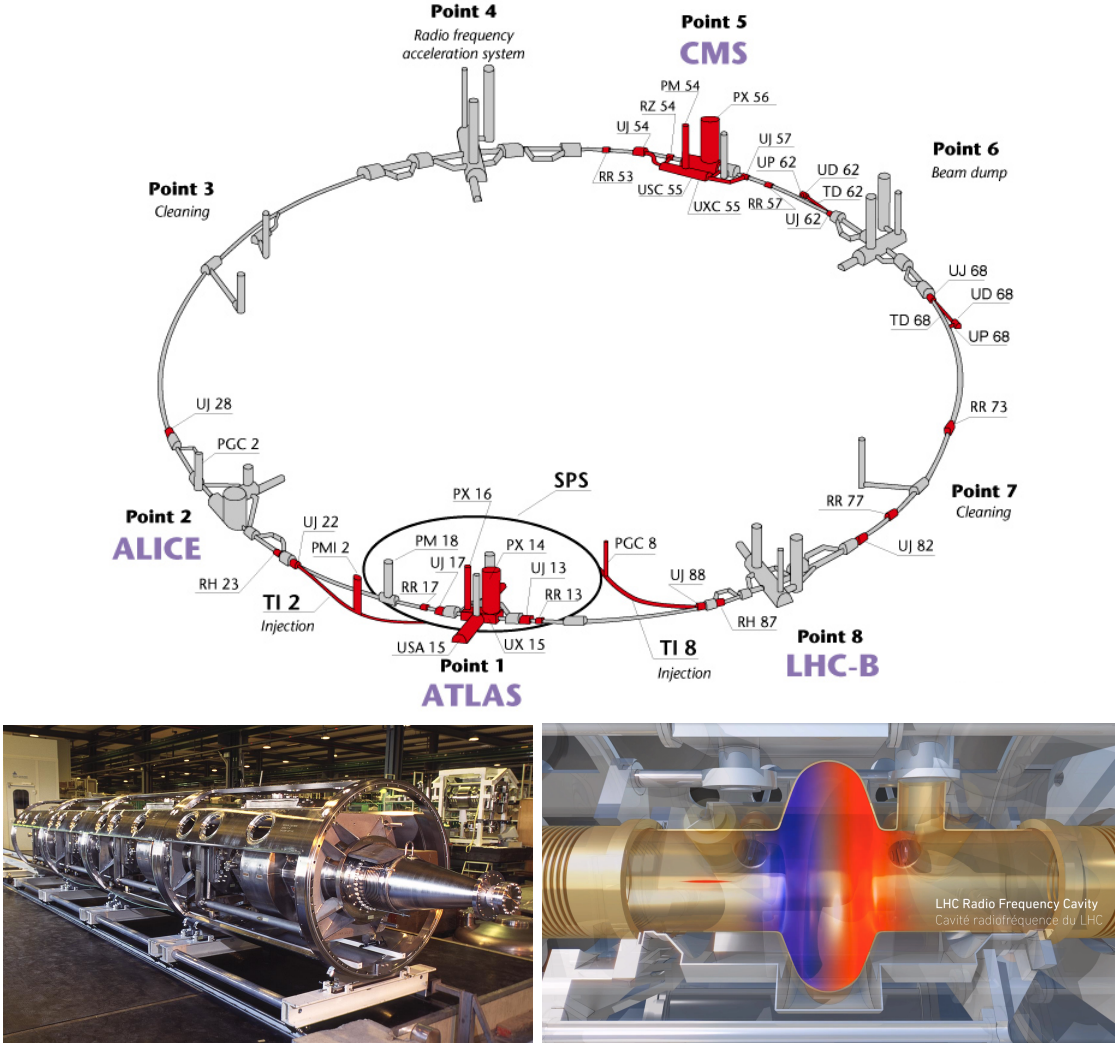


Figure 3.4: Top: LHC layout. The red zones indicate the infrastructure additions to the LEP installations, built to accommodate the ATLAS and CMS experiments which exceed the size of the former experiments located there [62]. Bottom: LHC RF cavities. A module (left picture) accommodates 4 cavities, each like the one in the right drawing, that accelerate protons and preserve the bunch structure of the beam. The color gradient pattern represents the strength of the electric field inside the cavity; red zone corresponds to the maximum of the oscillation electric field while the blue zone corresponds to the minimum. [66, 68]

1024 The LHC has a system of 16 RF cavities located in the so-called point 4, as
 1025 shown in Figure 3.4 top, tuned at a frequency of 400 MHz. The bottom side of
 1026 Figure 3.4 shows a picture of a RF module composed of 4 RF cavities working in a
 1027 superconducting state at 4.5 K; also, a representation of the accelerating electric field

that accelerates the protons in the bunch is shown. The maximum of the oscillating electric field (red region) picks the proton bunches at the entrance of the cavity and keeps accelerating them through the whole cavity. The protons are carefully timed so that in addition to the acceleration effect the bunch structure of the beam is preserved.

While protons are accelerated in one section of the LHC ring, where the RF cavities are located, in the rest of their path they have to be kept in the curved trajectory defined by the LHC ring. Technically, LHC is not a perfect circle; RF, injection, beam dumping, beam cleaning and sections before and after the experimental points where protons collide are all straight sections. In total, there are 8 arcs 2.45 km long each and 8 straight sections 545 m long each. In order to curve the proton's trajectory in the arc sections, superconducting dipole magnets are used.

Inside the LHC ring, there are two proton beams traveling in opposite directions in two separated beam pipes; the beam pipes are kept at ultra-high vacuum ($\sim 10^{-9}$ Pa) to ensure that there are no particles that interact with the proton beams. The superconducting dipole magnets used in LHC are made of a NbTi alloy, capable of transporting currents of about 12000 A when cooled at a temperature below 2K using liquid helium (see Figure 3.5).

Protons in the arc sections of LHC feel a centripetal force exerted by the dipole magnets; the magnitude of magnetic field needed to keep the protons in the LHC curved trayectomy can be found assuming that protons travel at $v \approx c$, using the standard values for proton mass and charge and the LHC radius, as

$$F_m = \frac{mv^2}{r} = qBv \rightarrow B = 8.33T \quad (3.1)$$

which is about 100000 times the Earth's magnetic field. A representation of the

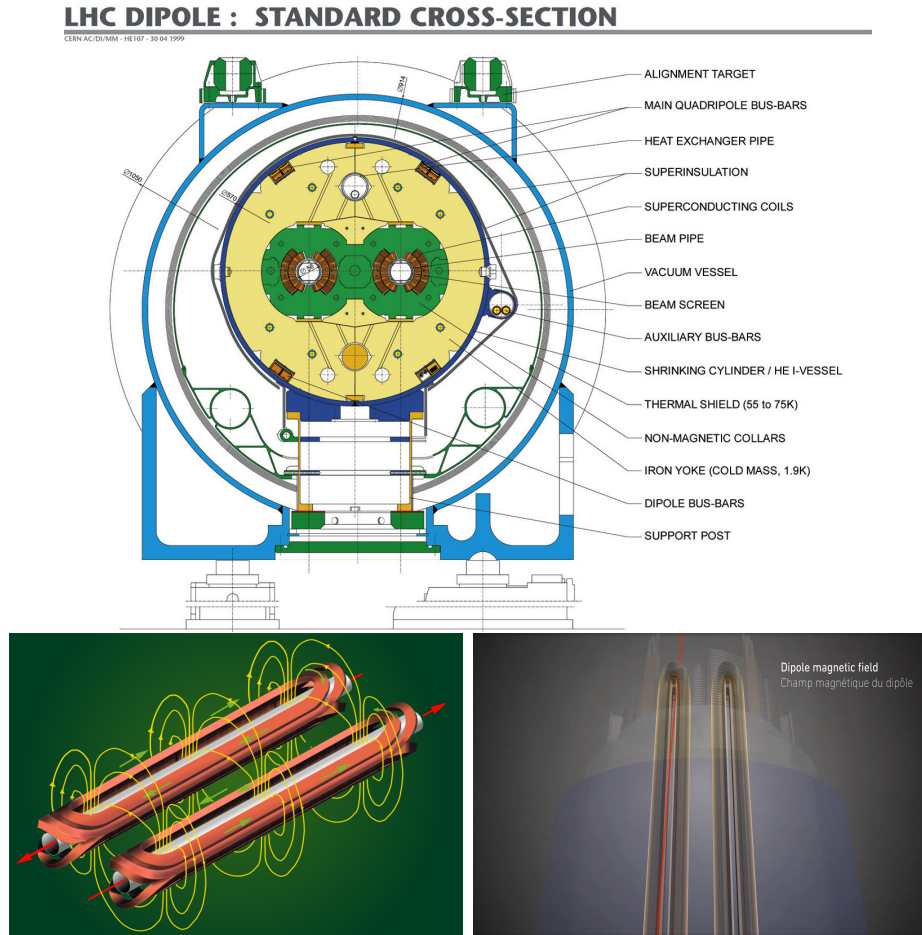


Figure 3.5: Top: LHC dipole magnet transverse view; cooling, shielding and mechanical support are indicated. Bottom left: Magnetic field generated by the dipole magnets; note that the direction of the field inside one beam pipe is opposite with respect to the other beam pipe which guarantee that both proton beams are curved in the same direction towards the center of the ring. The effect of the dipole magnetic field on the proton beam is represented on the bottom right side [66, 69, 70].

1051 magnetic field generated by the dipole magnets is shown on the bottom left side of
 1052 Figure 3.5. The bending effect of the magnetic field on the proton beam is shown on
 1053 the bottom right side of Figure 3.5. Note that the dipole magnets are not curved;
 1054 the arc section of the LHC ring is composed of straight dipole magnets of about 15
 1055 m. In total there are 1232 dipole magnets along the LHC ring.
 1056 In addition to the bending of the beam trajectory, the beam has to be focused. The

focusing is performed by quadrupole magnets installed in a different straight section; in total 858 quadrupole magnets are installed along the LHC ring. Other effects like electromagnetic interaction among bunches, interaction with electron clouds from the beam pipe, the gravitational force on the protons, differences in energy among protons in the same bunch, among others, are corrected using sextupole and other magnetic multipoles.

The two proton beams inside the LHC ring are made of bunches with a cylindrical shape of about 7.5 cm long and about 1 mm in diameter; when bunches are close to the interaction point (IP), the beam is focused up to a diameter of about 16 μm in order to maximize the probability of collisions between protons. The number of collisions per second is proportional to the cross section of the bunches with the *luminosity* (L) as the proportionality factor, thus, the luminosity can be calculated using

$$L = fn \frac{N_1 N_2}{4\pi\sigma_x\sigma_y} \quad (3.2)$$

where f is the revolution frequency, n is the number of bunches per beam, N_1 and N_2 are the numbers of protons per bunch, σ_x and σ_y are the gaussian transverse sizes of the bunches. With the expected parameters, the LHC expected luminosity is about

$$f = \frac{v}{2\pi r_{LHC}} \approx \frac{3 \times 10^8 \text{ m/s}}{27 \text{ km}} \approx 11.1 \text{ kHz},$$

$$n = 2808$$

$$N_1 = N_2 \sim 1.5 \times 10^{11}$$

$$\sigma_x = \sigma_y = 16 \mu\text{m}$$

1072

$$L = 1.28 \times 10^{34} \text{ cm}^{-2} \text{ s}^{-1} = 1.28 \times 10^{-5} \text{ fb}^{-1} \text{ s}^{-1} \quad (3.3)$$

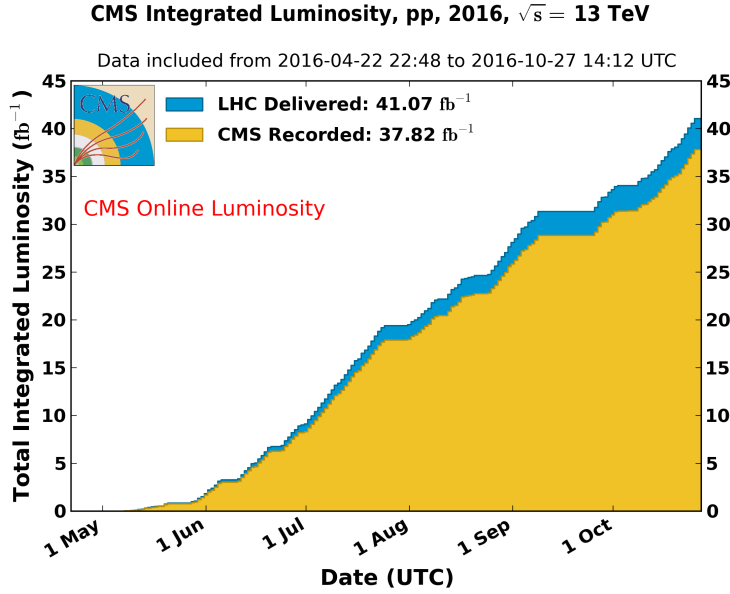


Figure 3.6: Integrated luminosity delivered by LHC and recorded by CMS during 2016. The difference between the delivered and the recorded luminosity is due to fails and issues occurred during the data taking in the CMS experiment [71].

1073 Luminosity is a fundamental aspect of LHC given that the bigger luminosity the
 1074 bigger number of collisions, which means that for processes with a very small cross
 1075 section the number of expected occurrences is increased and so the chances of being
 1076 detected. The integrated luminosity, collected by the CMS experiment during 2016
 1077 is shown in Figure 3.6; the data analyzed in this thesis corresponds to an integrated
 1078 luminosity of 35.9 fb^{-1} at a center of mass-energy $\sqrt{s} = 13 \text{ TeV}$.

1079 One way to increase L is increasing the number of bunches in the beam. Cur-
 1080 rently, the separation between two consecutive bunches in the beam is 7.5 m which
 1081 corresponds to a time separation of 25 ns. In the full LHC ring the allowed number
 1082 of bunches is $n = 27\text{km}/7.5\text{m} = 3600$; however, there are some gaps in the bunch pat-
 1083 tern intended for preparing the dumping and injection of the beam, thus, the proton
 1084 beams are composed of 2808 bunches.

1085 Once the proton beams reach the desired energy, they are brought to cross each

1086 other producing pp collisions. The bunch crossing happens in precise places where
 1087 the four LHC experiments are located, as seen in the top of Figure 3.7. In 2008 pp
 1088 collisions of $\sqrt{s} = 7$ TeV were performed; the energy was increased to 8 TeV in 2012
 1089 and to 13 TeV in 2015.

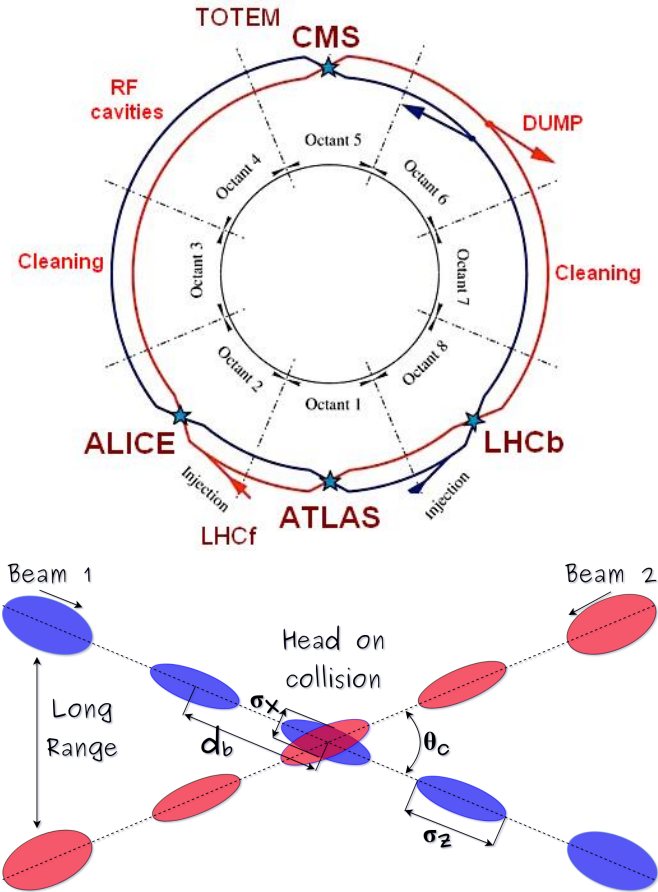


Figure 3.7: Top: LHC interaction points. Bunch crossing occurs where the LHC experiments are located [72]. Sections indicated as cleaning are dedicated to collimate the beam in order to protect the LHC ring from collisions with protons in very spreaded bunches. Bottom: bunch crossing scheme. Since the bunch crossing is not perfectly head-on, the luminosity is reduced in a factor of 17%; adapted from Reference [86].

1090 The CMS and ATLAS experiments are multi-purpose experiments, hence, they
 1091 are enabled to explore physics in any of the LHC collision modes. LHCb experiment
 1092 is optimized to explore bottom quark physics, while ALICE is optimized for heavy

1093 ion collisions searches; TOTEM and LHCf are dedicated to forward physics studies;
 1094 MoEDAL (not indicated in the Figure) is intended for monopole or massive pseudo
 1095 stable particles searches.

1096 At the IP there are two interesting details that need to be addressed. The first
 1097 one is that the bunch crossing does not occur head-on but at a small crossing angle θ_c
 1098 (280 μ rad in CMS and ATLAS) as shown in the bottom side of Figure 3.7, affecting
 1099 the overlapping between bunches; the consequence is a reduction of about 17% in
 1100 the luminosity (represented by a factor not included in eqn. 3.2). The second one
 1101 is the occurrence of multiple pp collisions in the same bunch crossing; this effect is
 1102 called *pileup* (PU). A fairly simple estimation of the PU follows from estimating the
 1103 probability of collision between two protons, one from each of the bunches in the
 1104 course of collision; it depends roughly on the ratio of proton size and the cross section
 1105 of the bunch in the IP, i.e.,

$$P(pp\text{-}collision) \sim \frac{d_{proton}^2}{\sigma_x \sigma_y} = \frac{(1\text{fm})^2}{(16\mu\text{m})^2} \sim 4 \times 10^{-21} \quad (3.4)$$

1106 however, there are $N = 1.15 \times 10^{11}$ protons in a bunch, thus the estimated number of
 1107 collisions in a bunch crossing is

$$PU = N^2 * P(pp\text{-}collision) \sim 50pp \text{ collision per bunch crossing}, \quad (3.5)$$

1108 about 20 of which are inelastic. A multiple pp collision event in a bunch crossing at
 1109 CMS is shown in Figure 3.8.

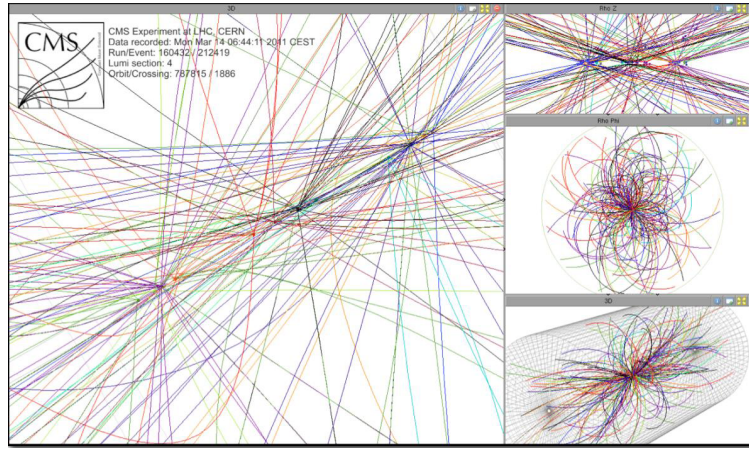


Figure 3.8: Multiple pp collision bunch crossing at CMS. [73].

1110 3.3 The CMS experiment

1111 CMS is a general-purpose detector designed to conduct research in a wide range
 1112 of physics from the standard model to new physics like extra dimensions and dark
 1113 matter. Located at Point 5 in the LHC layout as shown in Figure 3.4, CMS is
 1114 composed of several detection systems distributed in a cylindrical structure; in total,
 1115 CMS weights about 12500 tons in a very compact 21.6 m long and 14.6 m diameter
 1116 cylinder. It was built in 15 separate sections at the ground level and lowered to the
 1117 cavern individually to be assembled. A complete and detailed description of the CMS
 1118 detector and its components is given in Reference [74] on which this section is based.
 1119 Figure 3.9 shows the layout of the CMS detector. The detection system is composed
 1120 of (from the innermost to the outermost)

- 1121 • Pixel detector.
- 1122 • Silicon strip tracker.
- 1123 • Preshower detector.
- 1124 • Electromagnetic calorimeter.

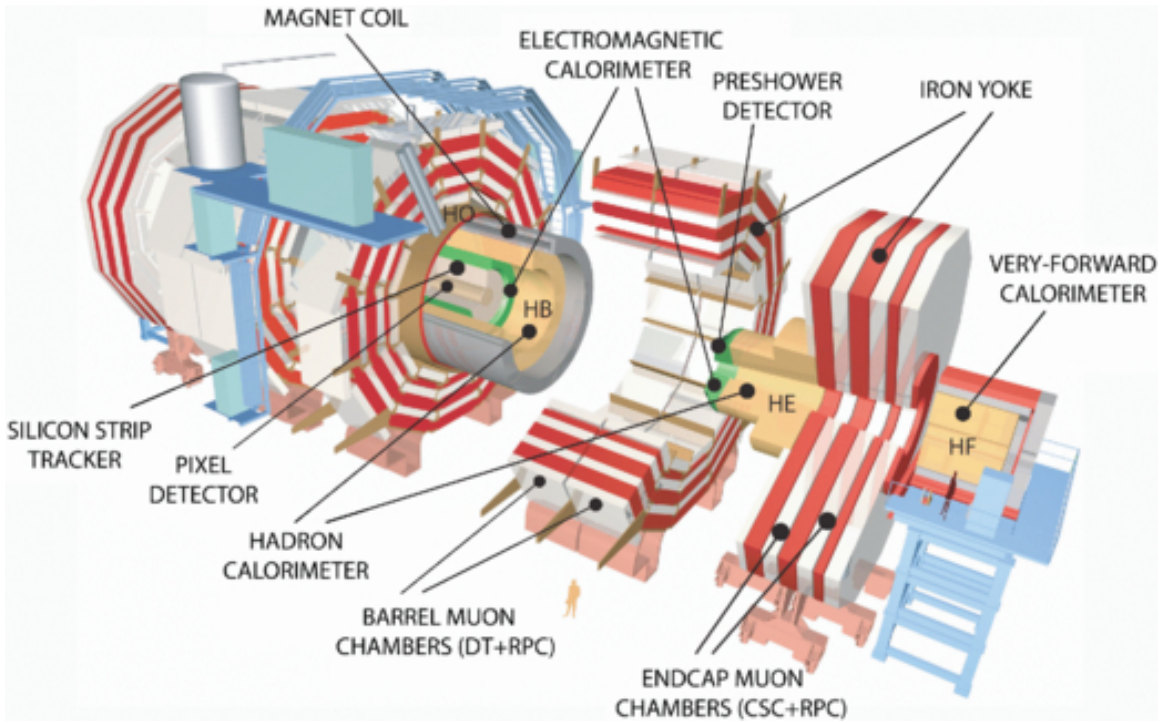


Figure 3.9: Layout of the CMS detector. The several subdetectors are indicated. The central region of the detector is referred as the barrel section while the endcaps are referred as the forward sections. [75].

1125 • Hadronic calorimeter.

1126 • Muon chambers (barrel and endcap)

1127 The central region of the detector is commonly referred as the barrel section while
 1128 the endcaps are referred as the forward sections of the detector; thus, each subdetector
 1129 is composed of a barrel section and a forward section.

1130 When a pp collision happens inside the CMS detector, many different particles are
 1131 produced, but only some of them live long enough to be detected; they are electrons,
 1132 photons, pions, kaons, protons, neutrons and muons; neutrinos are not detected by
 1133 the CMS detector. Thus, the CMS detector was designed to detect those particles and
 1134 measure their properties. Figure 3.10 shows a transverse slice of the CMS detector.
 1135 The silicon tracker (pixel detector + strip tracker) is capable to register the track of

the charged particles traversing it, while calorimeters (electromagnetic and hadronic) measure the energy of the particles that are absorbed by their materials. Considering the detectable particles, mentioned above, emerging from the IP, a basic description of the detection process is as follows.

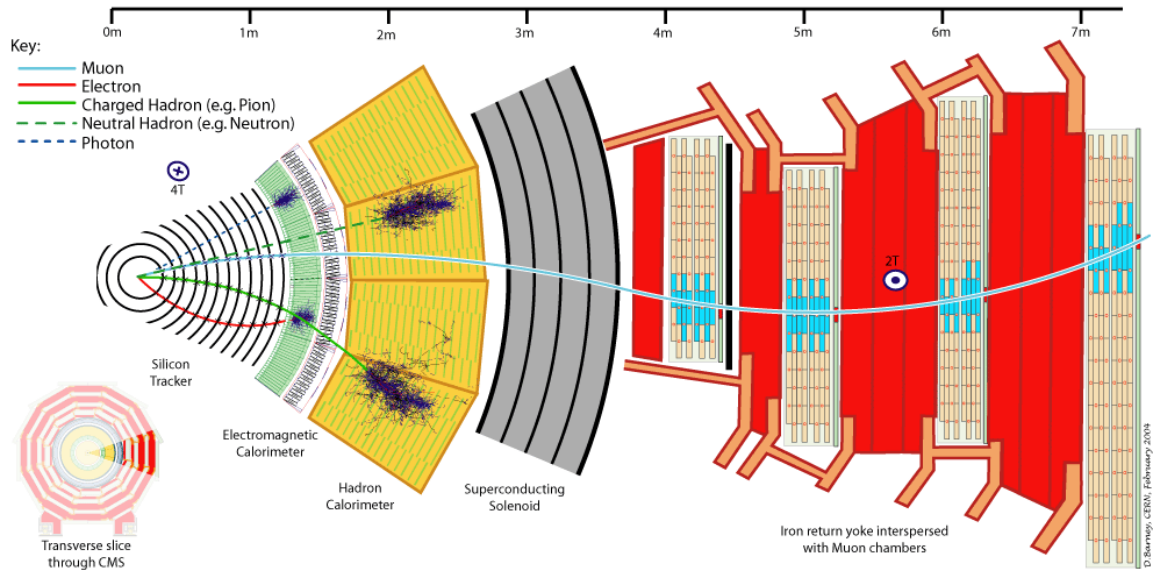


Figure 3.10: CMS detector transverse slice [76].

A muon emerging from the IP, will create a track on the silicon tracker and on the muon chambers. The design of the CMS detector is driven by the requirements on the identification, momentum resolution and unambiguous charge determination of the muons; therefore, a large bending power is provided by the solenoid magnet made of superconducting cable capable of generating a 3.8 T magnetic field. The muon track is bent twice since the magnetic field inside the solenoid is directed along the z -direction but outside its direction is reversed. Muons interact very weakly with the calorimeters, therefore, it is not absorbed but escape away from the detector.

An electron emerging from the IP will create a track along the tracker which will be bent due to the presence of the magnetic field, later, it will be absorbed in the electromagnetic calorimeter where its energy is measured.

1151 A photon will not leave a track because it is neutral, but it will be absorbed in
 1152 the electromagnetic calorimeter.

1153 A neutral hadron, like the neutron, will not leave a track either but it will lose a
 1154 small amount of its energy during its passage through the electromagnetic calorimeter
 1155 and then it will be absorbed in the hadron calorimeter depositing the rest of its energy.

1156 A charged hadron, like the proton or π^\pm , will leave a curved track on the silicon
 1157 tracker, some of its energy in the electromagnetic calorimeter and finally will be
 1158 absorbed in the hadronic calorimeter.

1159 A more detailed description of each detection system will be presented in the
 1160 following sections.

1161 3.3.1 CMS coordinate system

1162 The coordinate system used by CMS is centered on the geometrical center of the
 1163 detector which is the nominal IP as shown in Figure 3.11¹. The z -axis is parallel
 1164 to the beam direction, while the Y -axis pointing vertically upward, and the X -axis
 1165 pointing radially inward toward the center of the LHC.

1166 In addition to the common cartesian and cylindrical coordinate systems, two co-
 1167 ordinates are of particular utility in particle physics: rapidity (y) and pseudorapidity
 1168 (η), defined in connection to the polar angle θ , energy and longitudinal momentum
 1169 component (momentum along the z -axis) according to

$$y = \frac{1}{2} \ln \frac{E + p_z}{E - p_z} \quad \eta = -\ln \left(\tan \frac{\theta}{2} \right) \quad (3.6)$$

1170 Rapidity is related to the angle between the XY -plane and the direction in which
 1171 the products of a collision are emitted; it has the nice property that the difference

¹ Not all the pp interaction occur at the nominal IP because of the bunch lenght, therefore, each pp collision has its own IP location

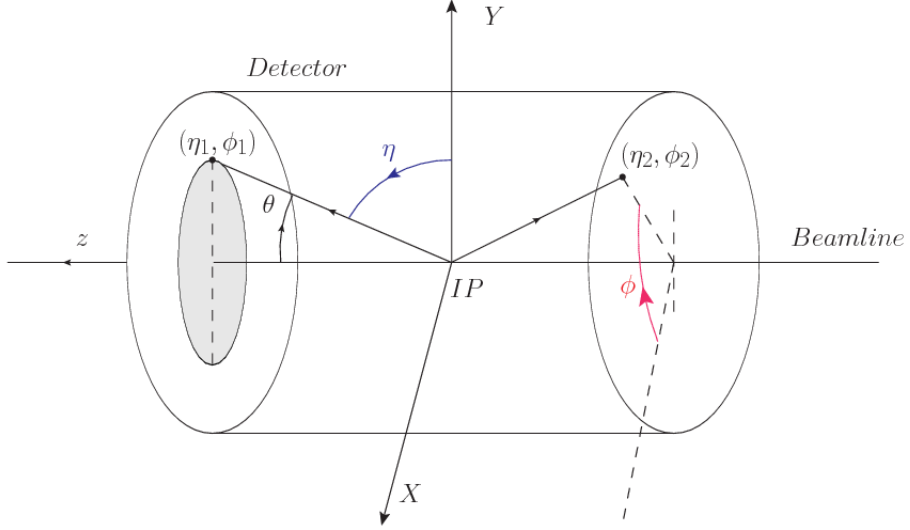


Figure 3.11: CMS detector coordinate system.

1172 between the rapidities of two particles is invariant with respect to Lorentz boosts
 1173 along the z -axis, hence, data analysis becomes more simple when based on rapid-
 1174 ity; however, it is not simple to measure the rapidity of highly relativistic particles,
 1175 as those produced after pp collisions. Under the highly relativistic motion approxi-
 1176 mation, y can be rewritten in terms of the polar angle, concluding that rapidity is
 1177 approximately equal to the pseudorapidity defined above, i.e., $y \approx \eta$. Note that η
 1178 is easier to measure than y given the direct relationship between the former and the
 1179 polar angle.

1180 The angular distance between two objects in the detector (ΔR) is commonly used
 1181 to judge the isolation of those object; it is defined in terms of their coordinates (η_1, ϕ_1) ,
 1182 (η_2, ϕ_2) as

$$\Delta R = \sqrt{(\Delta\eta)^2 - (\Delta\phi)^2} \quad (3.7)$$

1183 3.3.2 Tracking system

1184 The CMS tracking system is designed to provide a precise measurement of the trajectories (*track*) followed by the charged particles created after the pp collisions; also, the
 1185 precise reconstruction of the primary and secondary origins of the tracks (*vertices*) is
 1186 expected in an environment where, each 25 ns, the bunch crossing produces about 20
 1187 inelastic collisions and about 1000 particles.
 1188

1189 Physics requirements guiding the tracking system performance include the precise characterization of events involving gauge bosons, W and Z, and their leptonic
 1190 decays for which an efficient isolated lepton and photon reconstruction is of capital
 1191 importance, given that isolation is required to suppress background events to a level
 1192 that allows observations of interesting processes like Higgs boson decays or beyond
 1193 SM events.

1195 The ability to identify and reconstruct b -jets and B-hadrons within these jets is also
 1196 a fundamental requirement, achieved through the ability to reconstruct accurately
 1197 displaced vertices, given that b -jets are part of the signature of top quark physics, like
 1198 the one treated in this thesis.

1199 An schematic view of the CMS tracking system is shown in Figure 3.12

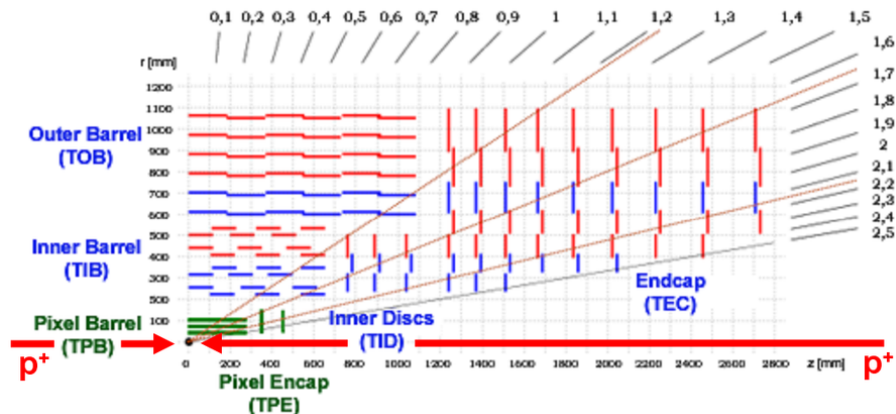


Figure 3.12: CMS tracking system schematic view [78].

1200 In order to satisfy these performance requirements, the tracking system uses two
 1201 different detector subsystems arranged in concentric cylindrical volumes, the pixel
 1202 detector and the silicon strip tracker; the pixel detector is located in the high particle
 1203 density region ($r < 20\text{cm}$) while the silicon strip tracker is located in the medium and
 1204 lower particle density regions $20\text{cm} < r < 116\text{cm}$.

1205 **Pixel detector**

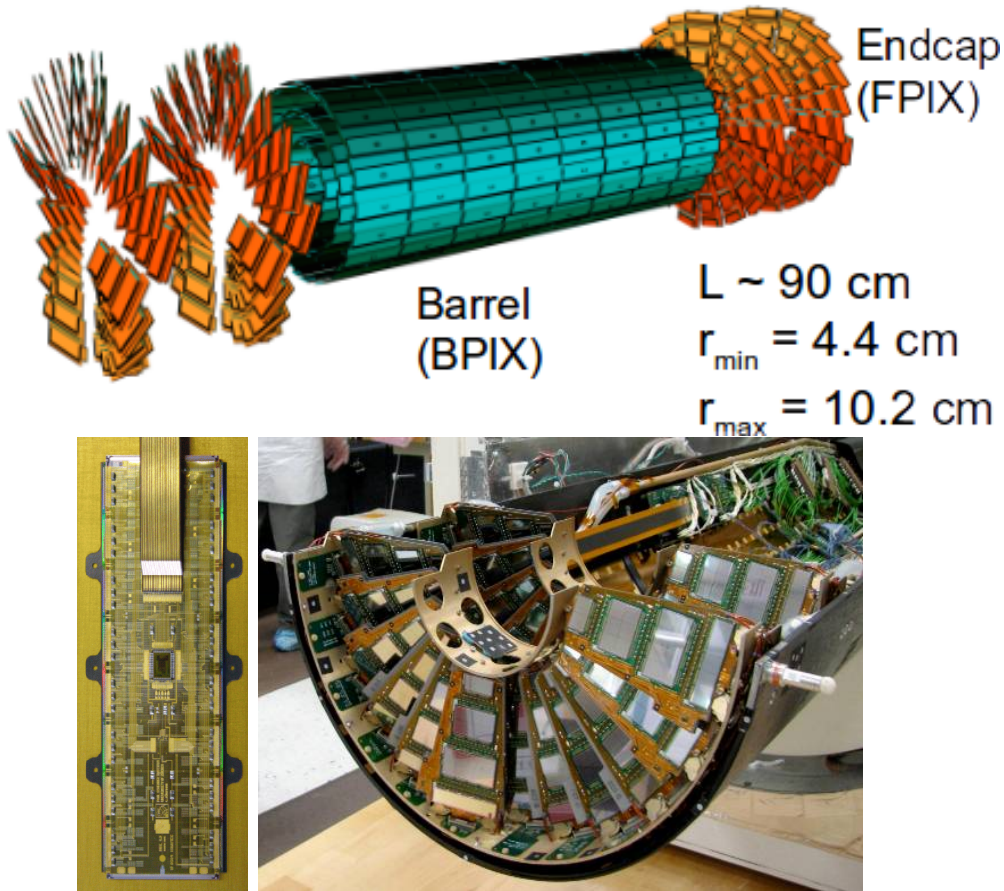


Figure 3.13: CMS pixel detector. Top: schematic view; Bottom: pictures of a barrel(BPIX) module(left) and forward modules(right) [74].

1206 The pixel detector was replaced during the 2016-2017 extended year-end technical
 1207 stop, due to the increasingly challenging operating conditions like the higher particle

flux and more radiation harsh environment, among others. The new one is responding as expected, reinforcing its crucial role in the successful way to fulfill the new LHC physics objectives after the discovery of the Higgs boson. Since the data sets used in this thesis were produced using the previous version of the pixel detector, it will be the subject of the description in this section. The last chapter of this thesis is dedicated to describe my contribution to the *Forward Pixel Phase 1 upgrade*.

The pixel detector was composed of 1440 silicon pixel detector modules organized in three-barrel layers in the central region (BPix) and two disks in the forward region (FPix) as shown in the top side of Figure 3.13; it was designed to record efficiently and with high precision, up to $20\mu\text{m}$ in the XY -plane and $20\mu\text{m}$ in the z -direction, the first three space-points (*hits*) nearest to the IP region in the range $|\eta| \leq 2.5$. The first barrel layer was located at a radius of 44 mm from the beamline, while the third layer was located at a radius of 102 mm, closer to the strip tracker inner barrel layer (see Section 3.3.3) in order to reduce the rate of fake tracks. The high granularity of the detector is represented in its about 66 Mpixels, each of size $100 \times 150\mu\text{m}^2$. The transverse momentum resolution of tracks can be measured with a resolution of 1-2% for muons of $p_T = 100$ GeV.

A charged particle passing through the pixel sensors produce ionization in them, giving energy for electrons to be removed from the silicon atoms, hence, creating electron-hole pairs. The collection of charges in the pixels generates an electrical signal that is read out by an electronic readout chip (ROC); each pixel has its own electronics which amplifies the signal. Combining the signal from the pixels activated by a traversing particle in the several layers of the detector allows one to reconstruct the particle's trajectory in 3D.

Commonly, the charge produced by traversing of a particle is collected by and shared among several pixels; by interpolating between pixels, the spatial resolution

1234 is improved. In the barrel section the charge sharing in the $r\phi$ -plane is due to the
 1235 Lorentz effect. In the forward pixels the charge sharing is enhanced by arranging the
 1236 blades in the turbine-like layout as shown in Figure 3.13 bottom left.

1237 **3.3.3 Silicon strip tracker**

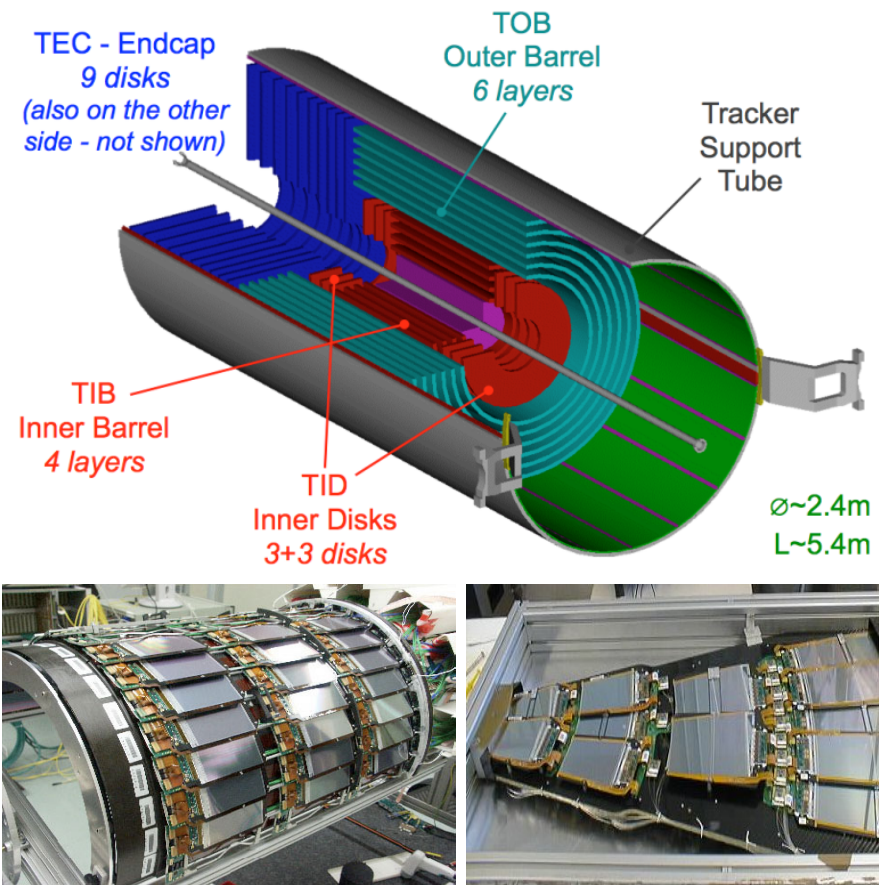


Figure 3.14: Top: CMS Silicon Strip Tracker (SST) schematic view. The SST is composed of the tracker inner barrel (TIB), the tracker inner disks (TID), the tracker outer barrel (TOB) and the tracker endcaps (TEC). Each part is made of silicon strip modules; the modules in blue represent two modules mounted back-to-back and rotated in the plane of the module by a stereo angle of 120 mrad in order to provide a 3-D reconstruction of the hit positions. Bottom: pictures of the TIB (left) and TEC (right) modules [80–82].

1238 The silicon strip tracker (SST) is the second stage in the CMS tracking system.
 1239 The top side of Figure 3.14 shows a schematic of the SST. The inner tracker region is

1240 composed of the tracker inner barrel (TIB) and the tracker inner disks (TID) covering
 1241 the region $r < 55$ cm and $|z| < 118$ cm. The TIB is composed of 4 layers while the TID
 1242 is composed of 3 disks at each end. The silicon sensors in the inner tracker are 320
 1243 μm thick, providing a resolution of about 13-38 μm in the $r\phi$ position measurement.

1244 The modules indicated in blue in the schematic view of Figure 3.14 are two mod-
 1245 ules mounted back-to-back and rotated in the plane of the module by a *stereo* angle
 1246 of 100 mrad; the hits from these two modules, known as *stereo hits*, are combined to
 1247 provide a measurement of the second coordinate (z in the barrel and r on the disks)
 1248 allowing the reconstruction of hit positions in 3-D.

1249 The outer tracker region is composed of the tracker outer barrel (TOB) and the
 1250 tracker endcaps (TEC). The six layers of the TOB offer coverage in the region $r > 55$
 1251 cm and $|z| < 118$ cm, while the 9 disks of the TEC cover the region $124 < |z| < 282$
 1252 cm. The resolution offered by the outer tracker is about 13-38 μm in the $r\phi$ position
 1253 measurement. The inner four TEC disks use silicon sensors 320 μm thick; those in
 1254 the TOB and the outer three TEC disks use silicon sensors of 500 μm thickness. The
 1255 silicon strips run parallel to the z -axis and the distance between strips varies from 80
 1256 μm in the inner TIB layers to 183 μm in the inner TOB layers; in the endcaps the
 1257 wedge-shaped sensors with radial strips, whose pitch range between 81 μm at small
 1258 radii and 205 μm at large radii.

1259 The whole SST has 15148 silicon modules, 9.3 million silicon strips and cover a
 1260 total active area of about 198 m^2 .

1261 **3.3.4 Electromagnetic calorimeter**

1262 The CMS electromagnetic calorimeter (ECAL) is designed to measure the energy of
 1263 electrons and photons. It is composed of 75848 lead tungstate crystals which have a

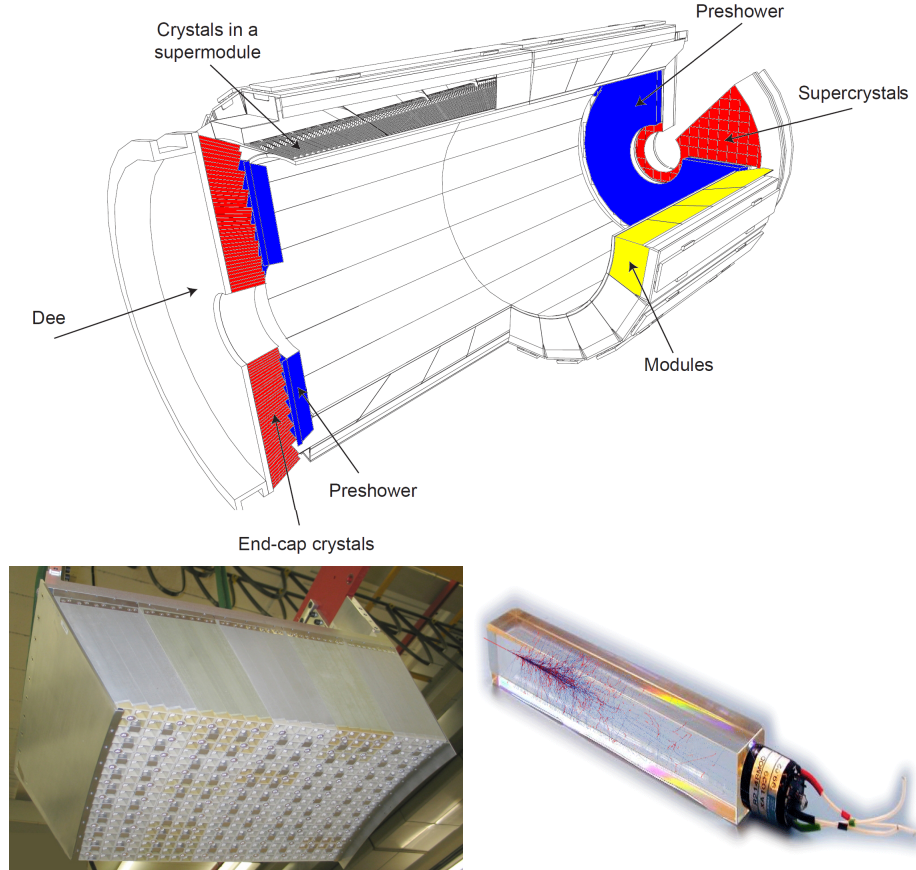


Figure 3.15: Top: CMS ECAL schematic view. Bottom: Module equipped with the crystals (left); ECAL crystal(right) with an artistic representation of an electromagnetic shower [74].

1264 short radiation length (0.89 cm) and fast response, since 80% of the light is emitted
 1265 within 25 ns; however, they are combined with Avalanche photodiodes (APDs) as
 1266 photodetectors given that crystals themselves have a low light yield ($30\gamma/\text{MeV}$). A
 1267 schematic view of the ECAL is shown in Figure 3.15.

1268 Energy is measured when electrons and photons are absorbed by the crystals
 1269 which generates an electromagnetic *shower*, as seen in bottom right picture of the
 1270 Figure 3.15; the shower is seen as a *cluster* of energy which depending on the amount
 1271 of energy deposited can involve several crystals. The ECAL barrel (EB) covers the
 1272 region $|\eta| < 1.479$, using crystals of depth of 23 cm and $2.2 \times 2.2 \text{ cm}^2$ transverse

1273 section; the ECAL endcap (EE) covers the region $1.479 < |\eta| < 3.0$ using crystals of
 1274 depth 22 cm and transverse section of $2.86 \times 2.86 \text{ cm}^2$; the photodetectors used are
 1275 vacuum phototriodes (VPTs). Each EE is divided in two structures called *Dees*.

1276 The preshower detector (ES) is installed in front of the EE and covers the region
 1277 $1.653 < |\eta| < 2.6$. The ES provides a precise measurement of the position of electro-
 1278 magnetic showers, which allows to distinguish electrons and photon signals from π^0
 1279 decay signals. The ES is composed of a layer of lead radiators followed by a layer of
 1280 silicon strip sensors. The lead radiators initiate electromagnetic showers when reached
 1281 by photons and electrons, then, the strip sensors measure the deposited energy and
 1282 the transverse shower profiles. The full ES thickness is 20 cm.

1283 3.3.5 Hadronic calorimeter

1284 Hadrons are not absorbed by the ECAL² but by the hadron calorimeter (HCAL),
 1285 which is made of a combination of alternating brass absorber layers and silicon photo-
 1286 multiplier(SiPM) layers; therefore, particles passing through the scintillator material
 1287 produce showers, as in the ECAL, as a result of the inelastic scattering of the hadrons
 1288 with the detector material. Since the particles are not absorbed in the scintillator,
 1289 their energy is sampled; therefore the total energy is not measured but estimated from
 1290 the energy clusters, which reduces the resolution of the detector. Brass was chosen
 1291 as the absorber material due to its short interaction length ($\lambda_I = 16.42\text{cm}$) and its
 1292 non-magnetivity. Figure 3.16 shows a schematic view of the CMS HCAL.

1293 The HCAL is divided into four sections; the Hadron Barrel (HB), the Hadron
 1294 Outer (HO), the Hadron Endcap (HE) and the Hadron Forward (HF) sections. The
 1295 HB covers the region $0 < |\eta| < 1.4$, while the HE covers the region $1.3 < |\eta| < 3.0$.
 1296 The HF, made of quartz fiber scintillator and steel as absorption material, covers the

² Most hadrons are not absorbed, but few low-energy ones might be.

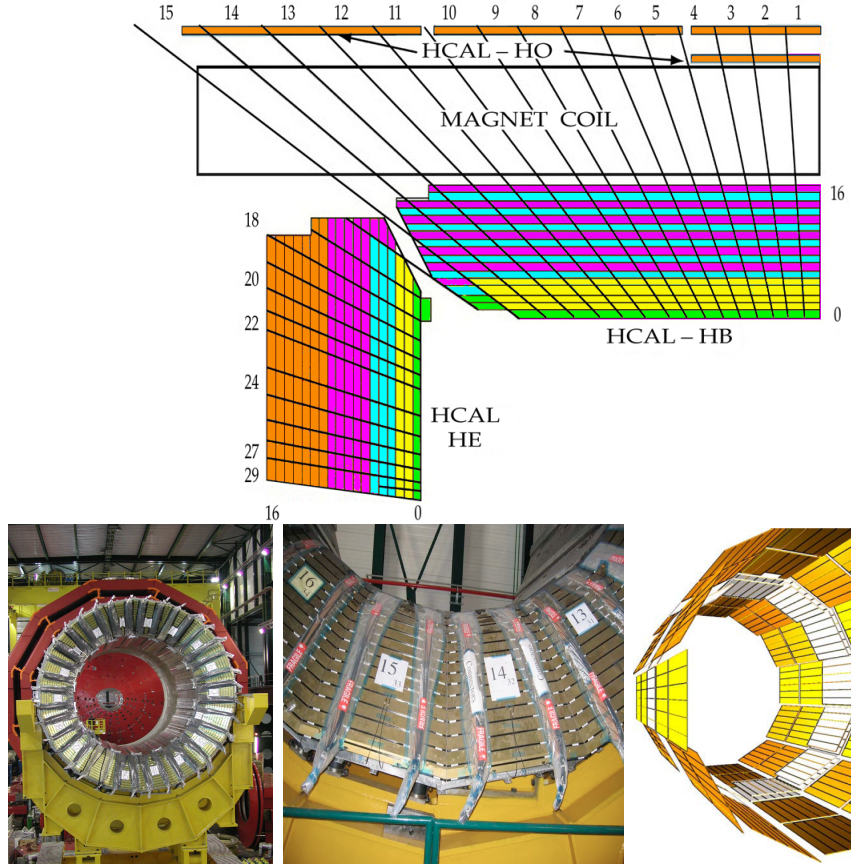


Figure 3.16: Top: CMS HCAL schematic view, the colors indicate the layers that are grouped into the same readout channels. Bottom: picture of a section of the HB; the absorber material is the golden region and scintillators are placed in between the absorber material (left and center). Schematic view of the HO (right). [83,84]

1297 forward region $3.0 < |\eta| < 5.2$. Both the HB and HF are located inside the solenoid.
 1298 The HO is placed outside the magnet as an additional layer of scintillators with the
 1299 purpose of measure the energy tails of particles passing through the HB and the
 1300 magnet (see Figure 3.16 top and bottom right).

1301 3.3.6 Superconducting solenoid magnet

1302 The superconducting magnet installed in the CMS detector is designed to provide
 1303 an intense and highly uniform magnetic field in the central part of the detector.

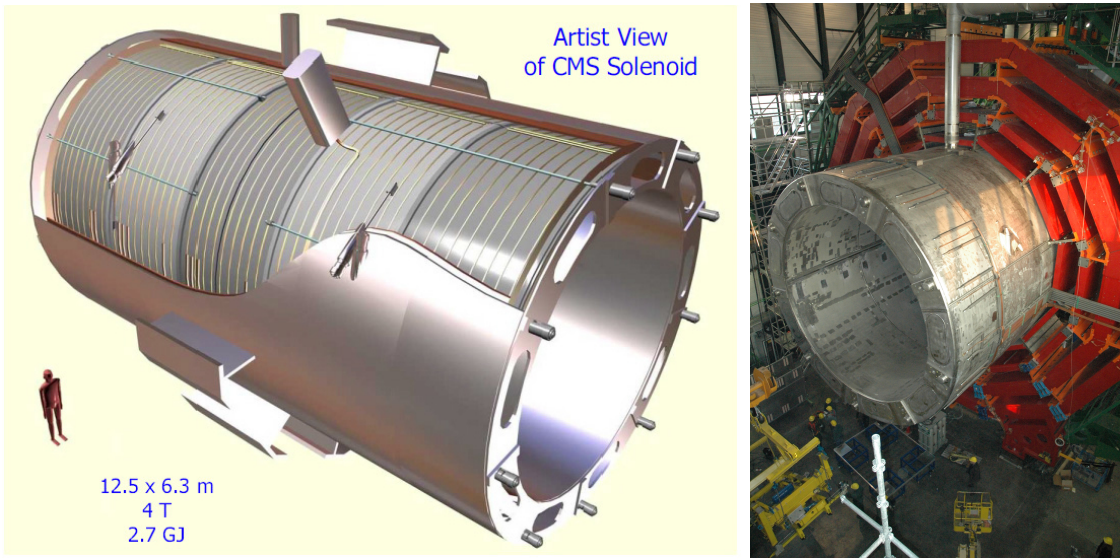


Figure 3.17: Artistic representation of the CMS solenoid magnet(left). The magnet is supported on an iron yoke (right) which also serves as the house of the muon detector and as mechanical support for the whole CMS detector [77].

1304 In fact, the tracking system takes advantage of the bending power of the magnetic
 1305 field to measure with precision the momentum of the particles that traverse it; the
 1306 unambiguous determination of the sign for high momentum muons was a driving
 1307 principle during the design of the magnet. The magnet has a diameter of 6.3 m, a
 1308 length of 12.5 m and a cold mass of 220 t; the generated magnetic field reaches a
 1309 strength of 3.8T. Since it is made of Ni-Tb superconducting cable it has to operate at
 1310 a temperature of 4.7 K by using a helium cryogenic system; the current circulating in
 1311 the cables reaches 18800 A under normal running conditions. The left side of Figure
 1312 3.17 shows an artistic view of the CMS magnet, while the right side shows a transverse
 1313 view of the cold mass where the winding structure is visible.

1314 The yoke (see Figure 3.17), composed of 5 barrel wheels and 6 endcap disks made
 1315 of iron, serves not only as the media for magnetic flux return but also provides housing
 1316 for the muon detector system and structural stability to the full detector.

1317 3.3.7 Muon system

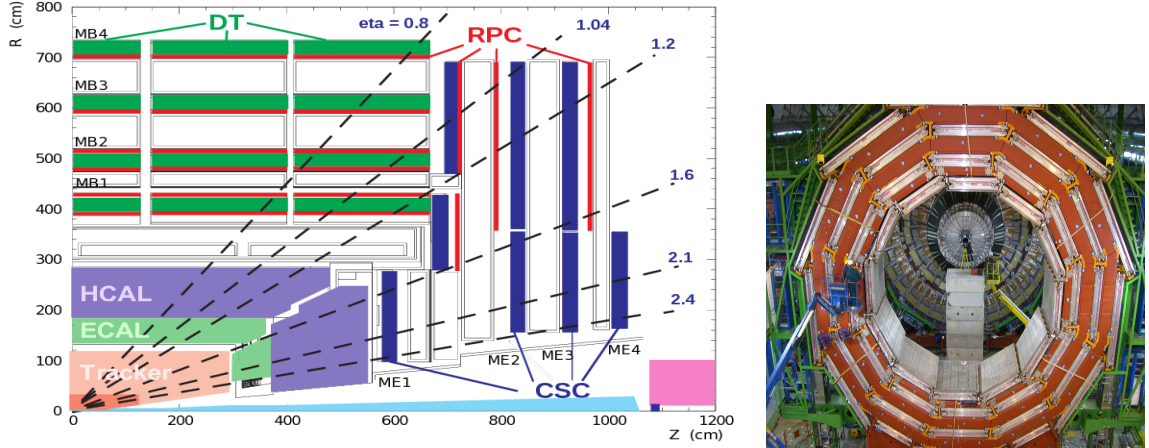


Figure 3.18: Left: CMS muon system schematic view; Right: one of the yoke rings with the muon DTs and RPCs installed; in the back it is possible to see the muon endcap [85].

1318 Muons are the only charged particles able to pass through all the CMS detector
 1319 due to their low ionization energy loss; thus, muons can be separated easily from the
 1320 high amount of particles produced in a pp collision. Also, muons are expected to be
 1321 produced in the decay of several new particles; therefore, good detection of muons
 1322 was one of the leading principles when designing the CMS detector.

1323 The CMS muon detection system (muon spectrometer) is embedded in the return
 1324 yoke as seen in Figure 3.18. It is composed of three different detector types, the drift
 1325 tube chambers (DT), cathode strip chambers (CSC), and resistive plate chambers
 1326 (RPC); DT are located in the central region $\eta < 1.2$ arranged in four layers of drift
 1327 chambers filled with an Ar/CO₂ gas mixture.

1328 The muon endcaps are made of CSCs covering the region $\eta < 2.4$ and filled with
 1329 a mixture of Ar/CO₂/CF₄. The reason behind using a different detector type lies on
 1330 the different conditions in the forward region like the higher muon rate and higher
 1331 residual magnetic field compared to the central region.

1332 The third type of detector used in the muon system is a set of four disks of RPCs

1333 working in avalanche mode. The RPCs provide good spatial and time resolutions. The
 1334 track of high- p_T muon candidates is built combining information from the tracking
 1335 system and the signal from up to six RPCs and four DT chambers.

1336 The muon tracks are reconstructed from the hits in the several layers of the muon
 1337 system.

1338 **3.3.8 CMS trigger system**

1339 CMS expects pp collisions every 25 ns, i.e., an interaction rate of 40 MHz for which
 1340 it is not possible to store the recorded data in full. In order to handle this high event
 1341 rate data, an online event selection, known as triggering, is performed; triggering
 1342 reduces the event rate to 100 Hz for storage and further offline analysis.

1343 The trigger system starts with a reduction of the event rate to 100 kHz in the
 1344 so-called *the level 1 trigger* (L1). L1 is based on dedicated programmable hardware
 1345 like Field Programmable Gate Arrays (FPGAs) and Application Specific Integrated
 1346 Circuits (ASICs), partly located in the detector itself; another portion is located in
 1347 the CMS underground cavern. Hit pattern information from the muon chambers
 1348 and the energy deposits in the calorimeter are used to decide if an event is accepted
 1349 or rejected, according to selection requirements previously defined, which reflect the
 1350 interesting physics processes. Figure 3.19 shows the L1 trigger architecture.

1351 The second stage in the trigger system is called *the high-level trigger* (HLT); events
 1352 accepted by L1 are passed to HLT in order to make an initial reconstruction of them.
 1353 HLT is software based and runs on a dedicated server farm, using selection algorithms
 1354 and high-level object definitions; the event rate at HLT is reduced to 100 Hz. The
 1355 first HLT stage takes information from the muon detectors and the calorimeters to
 1356 make the initial object reconstruction; in the next HLT stage, information from the

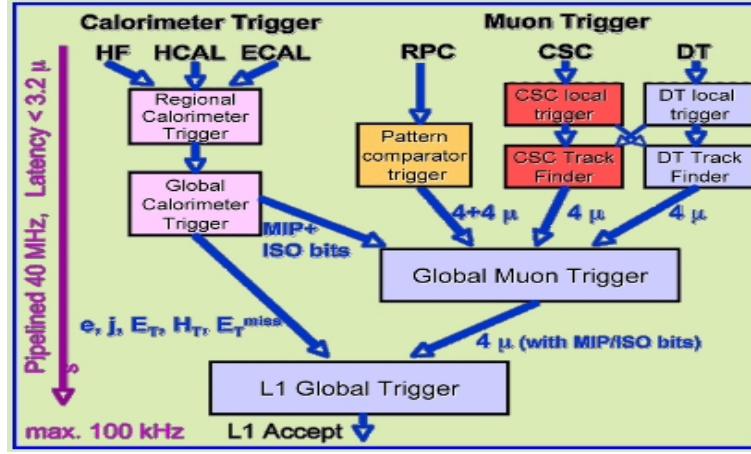


Figure 3.19: CMS Level-1 trigger architecture [86].

pixel and strip detectors is used to do first fast tracking and then full tracking online.
 This initial object reconstruction is used in further steps of the trigger system.

Events and preliminary reconstructed physics objects from HLT are sent to be fully reconstructed at the CERN computing center known also as Tier-0 facility. Again, the pixel detector information provides high-quality seeds for the track reconstruction algorithm offline, primary vertex reconstruction, electron and photon identification, muon reconstruction, τ identification, and b-tagging. After full reconstruction, data sets are made available for offline analyses.

3.3.9 CMS computing

Data coming from the experiment have to be stored and made available for further analysis; in order to cope with all the tasks implied in the offline data processing, like transfer, simulation, reconstruction and reprocessing, among others, a large computing power is required. The CMS computing system is based on the distributed architecture concept, where users of the system and physical computer centers are distributed worldwide and interconnected by high-speed networks.

The worldwide LHC computing grid (WLCG) is the mechanism used to provide

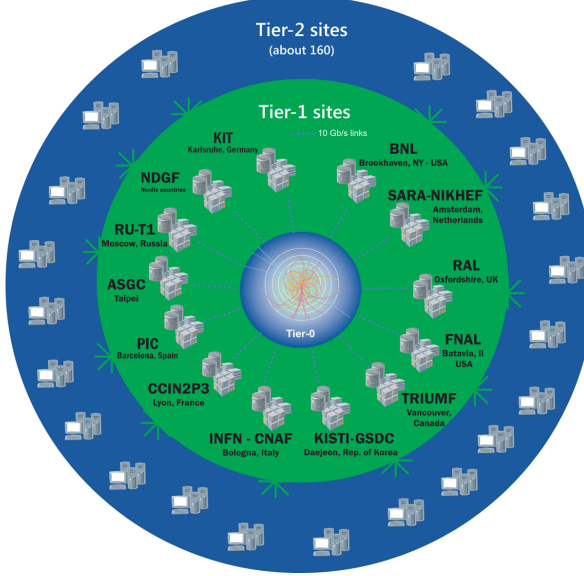


Figure 3.20: WLCG structure. The primary computer centers (Tier-0) are located at CERN (data center) and at the Wigner datacenter in Budapest. Tier-1 is composed of 13 centers and Tier-2 is composed of about 160 centers. [87].

1373 that distributed environment. WLCG is a tiered structure connecting computing
 1374 centers around the world, which provides the necessary storage and computing facil-
 1375 ities. The primary computing centers of the WLCG are located at the CERN and
 1376 the Wigner datacenter in Budapest and are known as Tier-0 as shown in Figure 3.20.
 1377 The main responsibilities for each tier level are [87]

- 1378 • **Tier-0:** initial reconstruction of recorded events and storage of the resulting
 1379 datasets, the distribution of raw data to the Tier-1 centers.
- 1380 • **Tier-1:** provide storage capacity, support for the Grid, safe-keeping of a pro-
 1381 portional share of raw and reconstructed data, large-scale reprocessing and safe-
 1382 keeping of corresponding output, generation of simulated events, distribution
 1383 of data to Tier 2s, safe-keeping of a share of simulated data produced at these
 1384 Tier 2s.
- 1385 • **Tier-2:** store sufficient data and provide adequate computing power for spe-

1386 cific analysis tasks and proportional share of simulated event production and
1387 reconstruction.

1388 Aside from the general computing strategy to manage the huge amount of data
1389 produced by experiments, CMS uses a software framework to perform a variety of
1390 processing, selection and analysis tasks. The central concept of the CMS data model
1391 referred to as *event data model* (EDM) is the *Event*; therefore, an event is the unit
1392 that contains the information from a single bunch crossing, any data derived from
1393 that information like the reconstructed objects, and the details of the derivation.

1394 Events are passed as the input to the *physics modules* that obtain information
1395 from them and create new information; for instance, *event data producers* add new
1396 data into the events, *analyzers* produce an information summary from an event set,
1397 *filters* perform selection and triggering.

1398 CMS uses several event formats with different levels of detail and precision

1399 • **Raw format:** events in this format contain the full recorded information from
1400 the detector as well as trigger decision and other metadata. An extended version
1401 of raw data is used to store information from the CMS Monte Carlo simulation
1402 tools (see Chapter 4). Raw data are stored permanently, occupying about
1403 2MB/event

1404 • **RECO format:** events in this format correspond to raw data that have been
1405 submitted to reconstruction algorithms like primary and secondary vertex re-
1406 construction, particle ID, and track finding. RECO events contain physics ob-
1407 jects and all the information used to reconstruct them; average size is about 0.5
1408 MB/event.

- 1409 • **AOD format:** Analysis Object Data (AOD) is the data format used in the
 1410 physics analyses given that it contains the parameters describing the high-level
 1411 physics objects in addition to enough information to allow a kinematic refitting if
 1412 needed. AOD events are filtered versions of the RECO events to which skimming
 1413 or other filtering have been applied, hence AOD events are subsets of RECO
 1414 events. Requires about 100 kB/event.
- 1415 • **Non-event data** are data needed to interpret and reconstruct events. Some
 1416 of the non-event data used by CMS contains information about the detector
 1417 contraction and condition data like calibrations, alignment, and detector status.

1418 Figure 3.21 shows the data flow scheme between CMS detector and tiers.

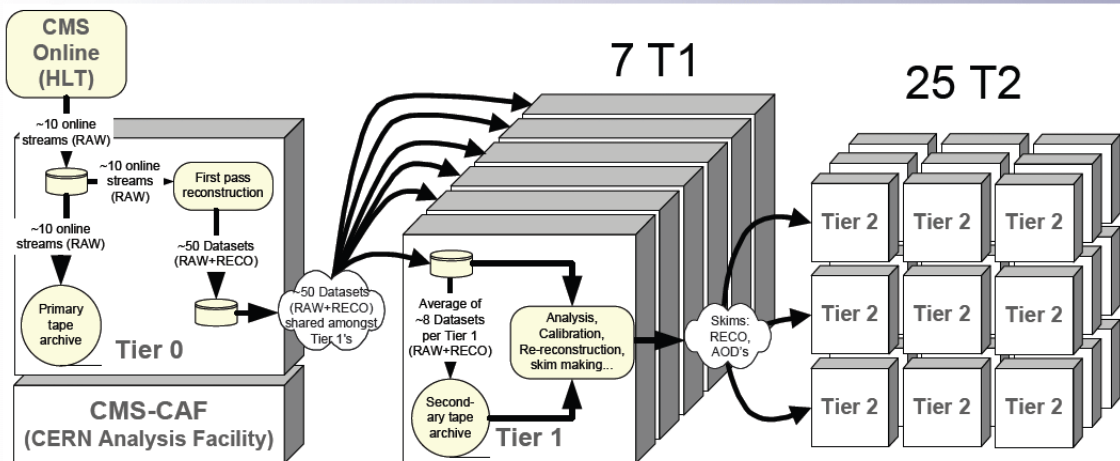


Figure 3.21: Data flow from CMS detector through tiers.

1419 The whole collection of software built as a framework is referred to as *CMSSW*. This
 1420 framework provides the services needed by the simulation, calibration and alignment,
 1421 and reconstruction modules that process event data, so that physicists can perform
 1422 analysis. The CMSSW event processing model is composed of one executable, called
 1423 `cmsRun`, and several plug-in modules which contains all the tools (calibration, recon-

1424 struction algorithms) needed to process an event. The same executable is used for
1425 both detector data and Monte Carlo simulations [88].

1426 **Chapter 4**

1427 **Event generation, simulation and
1428 reconstruction**

1429 The analysis of data recorded by the CMS experiment involves several stages of
1430 data processing in order to interpret the information provided by all the detection
1431 systems; in those stages, the particles produced after the pp collision are identified by
1432 reconstructing their trajectories and measuring their features. In addition, the SM
1433 provides a set of predictions that have to be compared with the experimental results;
1434 however, in most of the cases, theoretical predictions are not directly comparable
1435 to experimental results due to the diverse source of uncertainties introduced by the
1436 experimental setup and theoretical approximations, among others.

1437 The strategy to face these conditions consists of the implementation of theoretical
1438 models and statistical methods in computational algorithms to produce numerical
1439 results that can be compared with the experimental results. These computational
1440 algorithms are commonly known as Monte Carlo (MC) methods and, in the case of
1441 particle physics, they are designed to apply the SM rules and produce predictions
1442 about the physical observables measured in the experiments. Since particle physics is

1443 governed by quantum mechanics principles, predictions cannot be made from single
 1444 events; therefore, a high number of events are *generated* and predictions are produced
 1445 in the form of statistical distributions for the observables. Effects of the detector
 1446 presence are included in the predictions by introducing simulations of the detector
 1447 itself.

1448 This chapter presents a description of the event generation strategy and the tools
 1449 used to perform the detector simulation and physics object reconstruction. A com-
 1450 prehensive review of event generators for LHC physics can be found in Reference [89]
 1451 on which this chapter is based.

1452 4.1 Event generation

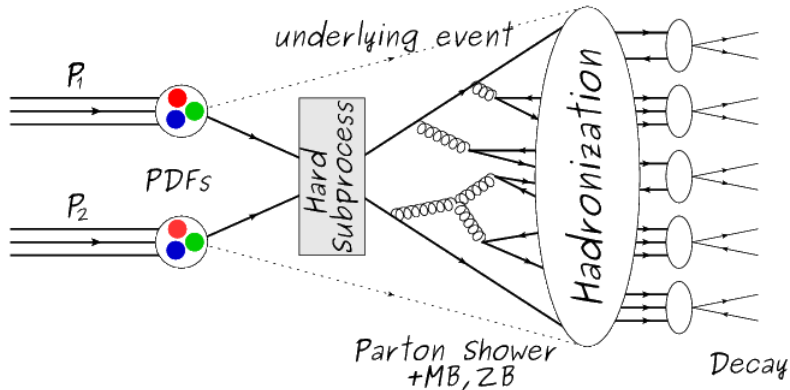


Figure 4.1: Event generation process. The actual interaction is generated in the hard subprocess while the parton shower describes the evolution of the partons from the hard subprocess. Modified from Reference [90].

1453 The event generation is intended to simulate events that mimic the behavior of
 1454 actual events produced in collisions; they obey a sequence of steps from the particle
 1455 collision hard process to the decay process into the final state. Figure 4.1 shows a
 1456 schematic view of the event generation process; the fact that the full process can be
 1457 treated as several independent steps is motivated by the QCD factorization theorem.

1458 Generation starts by taking into account the PDFs of the incoming particles.
 1459 Event generators offer the option to chose from several PDF sets depending on the
 1460 particular process under simulation¹; in the following, pp collisions will be consid-
 1461 ered. The *hard subprocess* describes the actual interaction between partons from the
 1462 incoming protons; it is represented by the matrix element connecting the initial and
 1463 final states of the interaction. Normally, the matrix element can be written as a sum
 1464 over Feynman diagrams with interferences between terms considered in the summa-
 1465 tion. During the generation of the hard subprocess, the production cross section is
 1466 calculated.

1467 The order of the Feynman diagrams involved in the calculation, i.e. the order in
 1468 the perturbation series, determine the order to which the cross section is calculated;
 1469 therefore, radiative corrections are included by considering higher order Feynman
 1470 diagrams where QCD radiation dominates. Currently, cross sections calculated to LO
 1471 do not offer a satisfactory description of the processes, i.e., the results are only reliable
 1472 for the shape of distributions; therefore, NLO calculations have to be performed with
 1473 the implication that the computing time needed is highly increased due to increment
 1474 in the number of diagrams involved and their complexity.

1475 The final parton content of the hard subprocess is subjected to the *parton shower*
 1476 which generates the gluon radiation. Parton showering evolves the partons, i.e., gluons
 1477 split into quark-antiquark pairs and quarks with enough energy radiate gluons giv-
 1478 ing rise to further parton multiplication, following the DGLAP (Dokshitzer-Gribov-
 1479 Lipatov-Altarelli-Parisi) equations [92–94]. Showering continues until the energy scale
 1480 is low enough to reach the non-perturbative limit.

1481 In the simulation of LHC processes that involve b quarks, like the single top quark
 1482 or Higgs associated production, it is necessary to consider that the b quark is heavier

¹ Different PDF sets under customizable conditions can be plotted using the tool in Reference [91].

1483 than the proton; hence, the QCD interaction description is made in two different
 1484 schemes [95]

- 1485 • four-flavor (4F) scheme. b quarks appear only in the final state because they
 1486 are heavier than the proton and therefore they can be produced only from the
 1487 splitting of a gluon into pairs or singly in association with a t quark in high
 1488 energy-scale interactions; hence, during the simulation, the b -PDFs are set to
 1489 zero. Calculations in this scheme are more complicated due to the presence
 1490 of the second b quark but the full kinematics is considered already at LO and
 1491 therefore the accuracy of the description is better.
- 1492 • five-flavor (5F) scheme. b quarks are considered massless, therefore they can
 1493 appear in both initial and final states since they can now be part of the proton;
 1494 thus, during the simulation b -PDFs are not set to zero. In this scheme, calcula-
 1495 tions are simpler than in the 4F scheme and possible logarithmic divergences
 1496 are absorbed by the PDFs through the DGLAP evolution.

1497 In this thesis, the tHq events are generated using the 4F scheme in order to reduce
 1498 uncertainties, while the tHW events are generated using the 5F scheme to eliminate
 1499 LO interference with $t\bar{t}H$ process [48].

1500 Partons involved in the pp collision are the focus of the simulation, however, the
 1501 rest of the partons inside the incoming protons are also affected because the remnants
 1502 are colored objects; also, multiple parton interactions can occur. The hadronization
 1503 of the remnants and multiple parton interactions are known as *underlying event* and
 1504 it has to be included in the simulation. In addition, multiple pp collisions in the same
 1505 bunch crossing (pile-up mentioned in 3.2) occurs, actually in two forms

1506 • *in-time PU* which refers to multiple pp collision in the bunch crossing but that
 1507 are not considered as primary vertices.

1508 • *out-of-time PU* which refers to overlapping pp collisions from consecutive bunch
 1509 crossings; this can occur due to the time delays in the detection systems where
 1510 information from one bunch crossing is assigned to the next or previous one.

1511 While the underlying event effects are included in generation using generator-
 1512 specific tools, PU effects are added to the generation by overlaying minimum-bias
 1513 (MB) and zero-bias (ZB) events to the generated events. MB events are inelastic
 1514 events from real detector data selected by using a loose trigger with as little bias as
 1515 possible, therefore accepting a large fraction of the overall inelastic event; ZB events
 1516 correspond to random events recorded by the detector when collisions are likely. MB
 1517 models in-time PU and ZB models out-of-time PU.

1518 The next step in the generation process is called *hadronization*. Since particles
 1519 with a net color charge are not allowed to exits in isolation, they have to recombine
 1520 to form bound states. This is precisely the process by which the partons resulting
 1521 from the parton shower arrange themselves as color singlets to form hadrons. At
 1522 this step, the energy-scale is low and the strong coupling constant is large, therefore
 1523 hadronization process is non-perturbative and the evolution of the partons is described
 1524 using phenomenological models. Most of the baryons and mesons produced in the
 1525 hadronization are unstable and hence they will decay in the detector.

1526 The last step in the generation process corresponds to the decay of the unstable
 1527 particles generated during hadronization; it is also simulated in the hadronization
 1528 step, based on the known branching ratios.

1529 The generated MC sample is characterized by the number of events in the sample,
 1530 the cross section of the simulated process and the luminosity, related as $\sigma = N_{events}L$;

1531 since the cross section of the generated process is fixed, the luminosity of the MC
 1532 sample varies with the number of events in it. In order to perform a simulation at
 1533 a given luminosity, it is necessary to *weight* the MC sample to the corresponding
 1534 experimental luminosity of interest, such that it will be possible to make predictions
 1535 like the number of events of signal or background that will be produced in a data
 1536 sample corresponding to that luminosity. In this sense, the weight is the ratio between
 1537 the desired luminosity and the original MC sample luminosity.

1538 4.2 Monte Carlo Event Generators

1539 The event generation described in the previous section has been implemented in
 1540 several software packages for which a brief description is given in the following.

- 1541 • **PYTHIA 8.** This program is designed to perform the generation of high
 1542 energy physics events that describes the collisions between particles such as
 1543 electrons and protons. Several theories and models are implemented in it, in
 1544 order to describe physical aspects like hard and soft interactions, parton dis-
 1545 tributions, initial and final-state parton showers, multiple parton interactions,
 1546 beam remnants, hadronization² and particle decay. Thanks to extensive test-
 1547 ing, several optimized parametrizations, known as *tunings*, have been defined
 1548 in order to improve the description of actual collisions to a high degree of pre-
 1549 cision; for analysis at $\sqrt{s} = 13$ TeV, the underlying event CUETP8M1 tune is
 1550 employed [97]. The calculation of the matrix element is performed at LO which
 1551 is not enough for the current required level of precision; therefore, PYTHIA
 1552 is often used for parton shower, hadronization and decays, while other event
 1553 generators are used to generate the matrix element at NLO.

² based in the Lund string model [96]

- 1554 • **MadGraph5_aMC@NLO.** MadGraph is a matrix element generator which
 1555 calculates the amplitudes for all contributing Feynman diagrams of a given
 1556 process but does not provide a parton shower while MC@NLO incorporates
 1557 NLO QCD matrix elements consistently into a parton shower framework; thus,
 1558 MadGraph5_aMC@NLO, as a merger of the two event generators MadGraph5
 1559 and aMC@NLO, is an event generator capable to calculate tree-level and NLO
 1560 cross sections and perform the matching of those with the parton shower. It
 1561 is one of the most frequently used matrix element generators; however, it has
 1562 the particular feature of the presence of negative event weights. These negative
 1563 weights comes from interferences between Feynman diagrams and affect the
 1564 calculation of the cross sections due to the presence of contributions of negative
 1565 sign. Negative weights also affect the reproduction of the properties of the
 1566 objects generated since the effective number of events used in the calculation is
 1567 reduced, but these terms are needed in order to obtain the exact NLO results
 1568 for total rates. [98]
- 1569 • **POWHEG.** It is an NLO matrix element generator where the hardest emis-
 1570 sion of color charged particles is generated in such a way that the negative event
 1571 weights issue of MadGraph5_aMC@NLO is overcome; however, the method re-
 1572 quires an interface with p_T -ordered parton shower³ or a parton shower generator
 1573 where this highest emission can be vetoed in order to avoid double counting of
 1574 this highest-energetic emission. PYTHIA is a commonly matched to POWHEG
 1575 event generator [100].
- 1576 Events resulting from the whole generation process are known as MC events.

³ emissions in the showering are ordered in p_t^2 [99]

¹⁵⁷⁷ **4.3 CMS detector simulation**

¹⁵⁷⁸ After generation, MC events contain the physics of the collisions but they are not
¹⁵⁷⁹ ready to be compared to the events recorded by the experiment since these recorded
¹⁵⁸⁰ events correspond to the response of the detection systems to the interaction with
¹⁵⁸¹ the particles traversing them. The simulation of the CMS detector has to be applied
¹⁵⁸² on top of the event generation; it is simulated with a MC toolkit for the simulation
¹⁵⁸³ of particles passing through matter called Geant4 [101] which is also able to simulate
¹⁵⁸⁴ the electronic signals that would be measured by all detectors inside CMS.

¹⁵⁸⁵ The simulation takes the generated particles contained in the MC events as input,
¹⁵⁸⁶ makes them pass through the simulated geometry, and models physics processes that
¹⁵⁸⁷ particles experience during their passage through matter. The full set of results from
¹⁵⁸⁸ particle-matter interactions corresponds to the *simulated hit*, which contains informa-
¹⁵⁸⁹ tion about the energy loss, momentum, and position. Particles of the input event are
¹⁵⁹⁰ called *primary*, while the particles originating from GEANT4-modeled interactions
¹⁵⁹¹ of primary particles with matter are called *secondary*. Simulated hits are the input
¹⁵⁹² of subsequent modules that emulate the response of the detector readout system and
¹⁵⁹³ triggers. The output from the emulated detection systems and triggers is known as
¹⁵⁹⁴ digitization [101, 102].

¹⁵⁹⁵ The modeling of the CMS detector corresponds to the accurate modeling of the
¹⁵⁹⁶ interaction among particles, the detector material, and the magnetic field. This
¹⁵⁹⁷ simulation procedure includes the following standard steps

- ¹⁵⁹⁸ • Modeling of the Interaction Region.
- ¹⁵⁹⁹ • Modeling of the particle passage through the hierarchy of volumes that compose
¹⁶⁰⁰ CMS detector and of the accompanying physics processes.

1601 • Modeling of the effect of multiple interactions per beam crossing and/or the
 1602 effect of events overlay (pile-up simulation).

1603 • Modeling of the detector's electronics response, signal shape, noise, calibration
 1604 constants (digitization).

1605 In addition to the full simulation, i.e., a detailed detector simulation, a faster
 1606 simulation (FastSim) have been developed, that may be used where much larger
 1607 statistics are required. In FastSim, detector material effects are parametrized and
 1608 included in the hits; those hits are used as input of the same higher-level algorithms⁴
 1609 used to analyze the recorded events. In this way, comparisons between fast and full
 1610 simulations can be performed [104].

1611 After the full detector simulation, the output events can be directly compared
 1612 to events actually recorded in the CMS detector. The collection of MC events that
 1613 reproduces the expected physics for a given process is known as MC sample.

1614 4.4 Event reconstruction

1615 The CMS experiment use the *particle-flow event reconstruction algorithm (PF)* to do
 1616 the reconstruction of particles produced in pp collisions. Next sections will present
 1617 a basic description of the *elements* used by PF (tracker tracks, energy clusters, and
 1618 muon tracks), based on the References [105,106] where more detailed descriptions can
 1619 be found.

⁴ track fitting, calorimeter clustering, b tagging, electron identification, jet reconstruction and calibration, trigger algorithms which will be considered in the next sections

1620 4.4.1 Particle-Flow Algorithm

1621 Each of the several subdetector systems of the CMS detector is dedicated to identify
 1622 a specific type of particle, i.e., photons and electrons are absorbed by the ECAL
 1623 and their reconstruction is based on ECAL information; hadrons are reconstructed
 1624 from clusters in the HCAL while muons are reconstructed from hits in the muon
 1625 chambers. PF is designed to correlate signals from all the detector layers (tracks and
 1626 energy clusters) in order to reconstruct and identify each final state particle and its
 1627 properties as sketched in Figure 4.2.

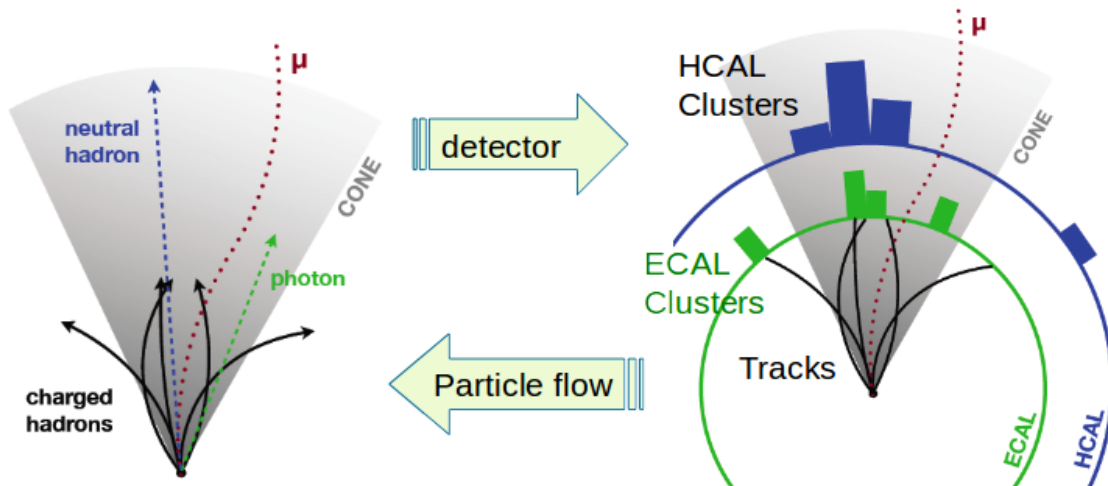


Figure 4.2: Particle flow algorithm. Information from the several CMS detection systems if provided as input to the algorithm which then combine it to identify and reconstruct all the particles in the final state and their properties. Reconstruction of simulated events is also performed by providing information from MC samples, detector and trigger simulation [107].

1628 For instance, a charged hadron is identified by a geometrical connection, known
 1629 as *link*, between one or more calorimeter clusters and a track in the tracker, provided
 1630 there are no hits in the muon system; combining several measurements allows a better
 1631 determination of the energy and charge sign of the charged hadron.

1632 **Charged-particle track reconstruction**

1633 The strategy used by PF in order to reconstruct tracks is called *Iterative Tracking*
 1634 which occurs in four steps:

1635 • Seed generation where initial track candidates are found by looking for a combi-
 1636 nation of hits in the pixel detector, strip tracker, and muon chambers. In total
 1637 ten iterations are performed, each one with a different seeding requirement.
 1638 Seeds are used to estimate the trajectory parameters and uncertainties at the
 1639 time of the full track reconstruction. Seeds are also considered track candidates.

1640 • Track finding using a tracking software known as Combinatorial Track Finder
 1641 (CTF) [108]. The seed trajectories are extrapolated along the expected flight
 1642 path of a charged particle, in agreement to the trajectory parameters obtained
 1643 in the first step, in an attempt to find additional hits that can be assigned to
 1644 the track candidates.

1645 • Track fitting where the found tracks are passed as input to a module which
 1646 provides the best estimate of the parameters of each trajectory.

1647 • Track selection where track candidates are submitted to a selection which dis-
 1648 cards those that fail a set of defined quality criteria.

1649 Iterations differ in the seeding configuration and the final track selection as elab-
 1650 orated in References [105, 106]. In the first iteration, high- p_T tracks and tracks pro-
 1651 duced near to the interaction region are identified and those hits are masked thereby
 1652 reducing the combinatorial complexity. Next, iterations search for more complicated
 1653 tracks, like low- p_T tracks and tracks from b hadron decays, which tend to be displaced
 1654 from the interaction region.

1655 **Vertex reconstruction**

1656 During the track reconstruction, an extrapolation toward to the calorimeters is per-
 1657 formed in order to match energy deposits; that extrapolation is also performed toward
 1658 the beamline in order to find the origin of the track known as *vertex*. The vertex re-
 1659 construction is performed by selecting from the available reconstructed tracks those
 1660 that are consistent with being originated in the interaction region where pp collisions
 1661 are produced. The selection involves a requirement on the number of tracker (pixel
 1662 and strip) hits and the goodness of the track fit.

1663 Selected tracks are clustered using a *deterministic annealing algorithm (DA)*⁵. A
 1664 set of candidate vertices and their associated tracks, resulting from the DA, are then
 1665 fitted with an *adaptive vertex fitter (AVF)* to produce the best estimate of the vertices
 1666 locations.

1667 The p_T of the tracks associated to a reconstructed vertex is added, squared and
 1668 used to organize the vertices; the vertex with the highest squared sum is designated
 1669 as the *primary vertex (PV)* while the rest are designated as PU vertices.

1670 **Calorimeter clustering**

1671 After traversing the CMS tracker system, electrons, photons and hadrons deposit their
 1672 energy in the ECAL and HCAL cells. The PF clustering algorithm aims to provide
 1673 a high detection efficiency even for low-energy particles and an efficient distinction
 1674 between close energy deposits. The clustering runs independently in the ECAL barrel
 1675 and endcaps, HCAL barrel and endcaps, and the two preshower layers, following two
 1676 steps:

- 1677 • cells with an energy larger than a given seed threshold and larger than the energy

⁵ DA algorithm and AVF are described in detail in References [110, 111]

1678 of the neighboring cells are identified as cluster seeds. The neighbor cells are
 1679 those that either share a side with the cluster seed candidate, or the eight closest
 1680 cells including cells that only share a corner with the seed candidate.

- 1681 • cells with at least a corner in common with a cell already in the cluster seed
 1682 and with an energy above a cell threshold are grouped into topological clusters.

1683 Clusters formed in this way are known as *particle-flow clusters*. With this cluster-
 1684 ing strategy, it is possible to detect and measure the energy and direction of photons
 1685 and neutral hadrons as well as differentiate these neutral particles from the charged
 1686 hadron energy deposits. In cases involving charged hadrons for which the track pa-
 1687 rameters are not determined accurately, for instance, low-quality and high- p_T tracks,
 1688 clustering helps in the energy measurements.

1689 Electron track reconstruction

1690 Although the charged-particle track reconstruction described above works for elec-
 1691 trons, they lose a significant fraction of their energy via bremsstrahlung photon radi-
 1692 ation before reaching the ECAL; thus, the reconstruction performance depends on the
 1693 ability to measure also the radiated energy. The reconstruction strategy, in this case,
 1694 requires information from the tracking system and from the ECAL. Bremsstrahlung
 1695 photons are emitted at similar η values to that of the electron but at different values
 1696 of ϕ ; therefore, the radiated energy can be recovered by grouping ECAL clusters in a
 1697 η window over a range of ϕ around the electron direction. The group is called ECAL
 1698 supercluster.

1699 Electron candidates from the track-seeding and ECAL super clustering are merged
 1700 into a single collection which is submitted to a full electron tracking fit with a

1701 Gaussian-sum filter (GSF) [109]. The electron track and its associated ECAL su-
 1702 percluster form a *particle-flow electron*.

1703 **Muon track reconstruction**

1704 Given that the CMS detector is equipped with a muon spectrometer capable of iden-
 1705 tifying and measuring the momentum of the muons traversing it, the muon recon-
 1706 struction is not specific to PF; therefore, three different muon types are defined:

- 1707 • *Standalone muon.* A clustering of the DTs or CSCs hits is performed to form
 1708 track segments; those segments are used as seeds for the reconstruction in the
 1709 muon spectrometer. All DTs, CSCs, and RPCs hits along the muon trajectory
 1710 are combined and fitted to form the full track. The fitting output is called a
 1711 *standalone-muon track*.
- 1712 • *Tracker muon.* Each track in the inner tracker with p_T larger than 0.5 GeV and
 1713 a total momentum p larger than 2.5 GeV is extrapolated to the muon system.
 1714 A *tracker muon track* corresponds to a extrapolated track that matches at least
 1715 one muon segment.
- 1716 • *Global muon.* When tracks in the inner tracker (inner tracks) and standalone-
 1717 muon tracks are matched and turn out to be compatible, their hits are combined
 1718 and fitted to form a *global-muon track*.

1719 Global muons sharing the same inner track with tracker muons are merged into
 1720 a single candidate. PF muon identification uses the muon energy deposits in ECAL,
 1721 HCAL, and HO associated with the muon track to improve the muon identification.

1722 **Particle identification and reconstruction**

1723 PF elements are connected by a linker algorithm that tests the connection between
 1724 any pair of elements; if they are found to be linked, a geometrical distance that
 1725 quantifies the quality of the link is assigned. Two elements may be linked indirectly
 1726 through common elements. Linked elements form *PF blocks* and each PF block may
 1727 contain elements originating from one or more particles. Links can be established
 1728 between tracks, between calorimeter clusters, and between tracks and calorimeter
 1729 clusters. The identification and reconstruction start with a PF block and proceed as
 1730 follows:

1731 • Muons. An *isolated global muon* is identified by evaluating the presence of
 1732 inner track and energy deposits close to the global muon track in the (η, ϕ)
 1733 plane, i.e., at a particular point of the global muon track, inner tracks and
 1734 energy deposits are sought within a radius of $\Delta R = 0.3$ (see eqn. 3.7) from the
 1735 muon track; if they exit and the p_T of the found track added to the E_T of the
 1736 found energy deposit does not exceed 10% of the muon p_T then the global muon
 1737 is an isolated global muon. This isolation condition is stringent enough to reject
 1738 hadrons misidentified as muons.

1739 *Non-isolated global muons* are identified using additional selection requirements
 1740 on the number of track segments in the muon system and energy deposits along
 1741 the muon track. Muons inside jets are identified with more stringent criteria
 1742 in isolation and momentum as described in Reference [112]. The PF elements
 1743 associated with an identified muon are masked from the PF block.

1744 • Electrons are identified and reconstructed as described above plus some addi-
 1745 tional requirements on fourteen variables like the amount of energy radiated,

1746 the distance between the extrapolated track position at the ECAL and the po-
 1747 sition of the associated ECAL supercluster, among others, which are combined
 1748 in an specialized multivariate analysis strategy that improves the electron iden-
 1749 tification. Tracks and clusters used to identify and reconstruct electrons are
 1750 masked in the PF block.

- 1751 ● Isolated photons are identified from ECAL superclusters with E_T larger than 10
 1752 GeV, for which the energy deposited at a distance of 0.15, from the supercluster
 1753 position on the (η, ϕ) plane, does not exceed 10% of the supercluster energy;
 1754 note that this is an isolation requirement. In addition, there must not be links
 1755 to tracks. Clusters involved in the identification and reconstruction are masked
 1756 in the PF block.
- 1757 ● Bremsstrahlung photons and prompt photons tend to convert to electron-positron
 1758 pairs inside the tracker, therefore, a dedicated finder algorithm is used to link
 1759 tracks that seem to originate from a photon conversion; in case those two tracks
 1760 are compatible with the direction of a bremsstrahlung photon, they are also
 1761 linked to the original electron track. Photon conversion tracks are also masked
 1762 in the PF block.
- 1763 ● The remaining elements in the PF block are used to identify hadrons. In the
 1764 region $|\eta| \leq 2.5$, neutral hadrons are identified with HCAL clusters not linked
 1765 to any track while photons from neutral pion decays are identified with ECAL
 1766 clusters without links to tracks. In the region $|\eta| > 2.5$ ECAL clusters linked to
 1767 HCAL clusters are identified with a charged or neutral hadron shower; ECAL
 1768 clusters with no links are identified with photons. HCAL clusters not used yet,
 1769 are linked to one or more unlinked tracks and to an unlinked ECAL in order to

1770 reconstruct charged-hadrons or a combination of photons and neutral hadrons
 1771 according to certain conditions on the calibrated calorimetric energy.

- 1772 • Charged-particle tracks may be linked together when they converge to a *sec-*
 1773 *ondary vertex (SV)* displaced from the IP where the PV and PU vertices are
 1774 reconstructed; at least three tracks are needed in that case, of which at most
 1775 one has to be a track with hits in tracker region between a PV and the SV.

1776 The linker algorithm, as well as the whole PF algorithm, has been validated and
 1777 commissioned; results from that validation are presented in Reference [105].

1778 Jet reconstruction

1779 Quarks and gluons may be produced in the pp collisions, therefore, their hadronization
 1780 will be seen in the detector as a shower of hadrons and their decay products in the
 1781 form of a *jet*. The anti- k_t algorithm [113] is used to perform the jet reconstruction
 1782 by clustering those PF particles within a cone (see Figure 4.3); previously, isolated
 1783 electrons, isolated muons, and charged particles associated with other interaction
 1784 vertices were excluded from the clustering.

1785 The anti- k_t algorithm proceeds in a sequential recombination of PF particles; the
 1786 distance between particles i and j (d_{ij}) and the distance between particles and the
 1787 beam are defined as

$$d_{ij} = \min \left(\frac{1}{k_{ti}^2}, \frac{1}{k_{tj}^2} \right) \frac{\Delta_{ij}^2}{R^2}$$

$$d_{iB} = \frac{1}{k_{ti}^2} \quad (4.1)$$

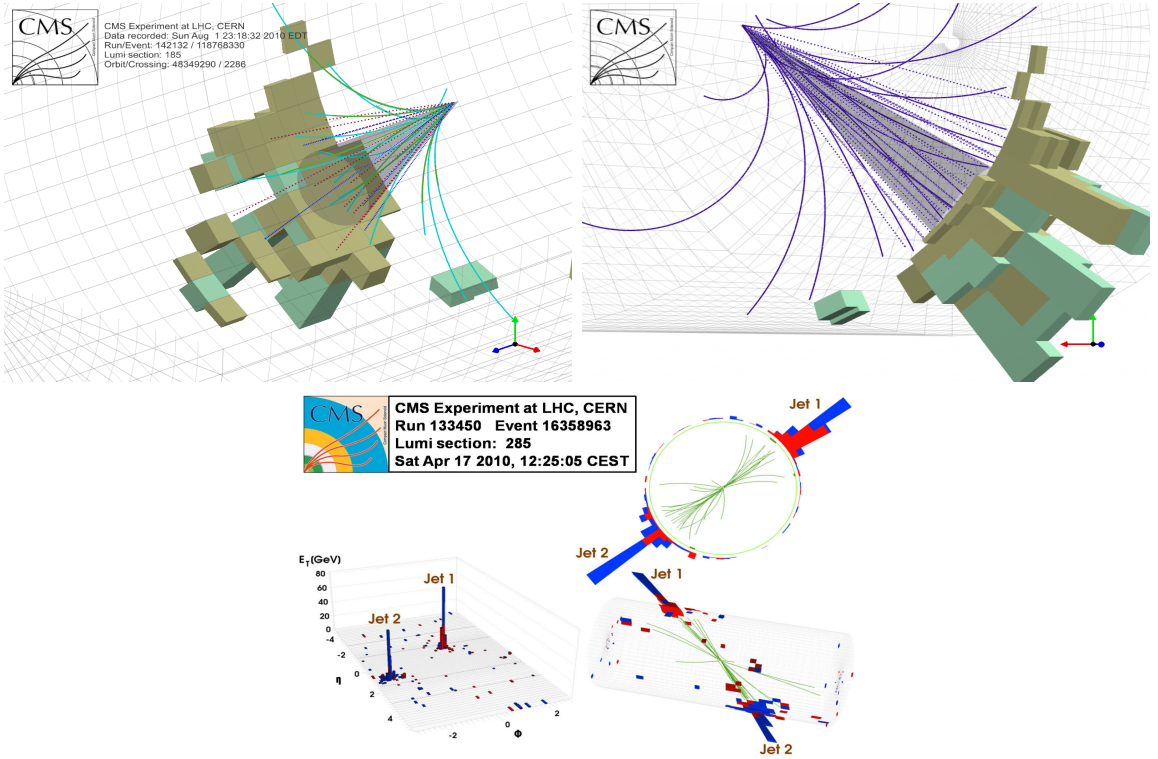


Figure 4.3: Jet reconstruction performed by the anti- k_t algorithm. Top: Two different views of a CMS recorded event are presented. Continuous lines correspond to tracks left by charged particles in the tracker while dotted lines are the imaginary paths followed by neutral particles. The green cubes represent the ECAL cells while the blue ones represent the HCAL cells; in both cases, the height of the cube represent the amount of energy deposited in the cells [114]. Bottom: Reconstruction of a recorded event with two jets [115].

where $\Delta_{ij}^2 = (y_i - y_j)^2 + (\phi_i - \phi_j)^2$, k_{ti} , y_i and ϕ_i are the transverse momentum, rapidity and azimuth of particle i respectively and R is the called jet radius. For all the remaining PF particles, after removing the isolated ones, d_{ij} and d_{iB} are calculated⁶ and the smallest is identified; if it is a d_{ij} , particles i and j are replaced with a new object whose momentum is the vectorial sum of the combined particles. If the smallest distance is a d_{iB} the clustering process ends, the object i (which at this stage should be a combination of several PF particles) is declared as a *Particle-flow-jet* (PF jet) and all the associated PF particles are removed from the detector. The clustering

⁶ Notice that this is a combinatorial calculation.

1796 process is repeated until no PF particles remain.

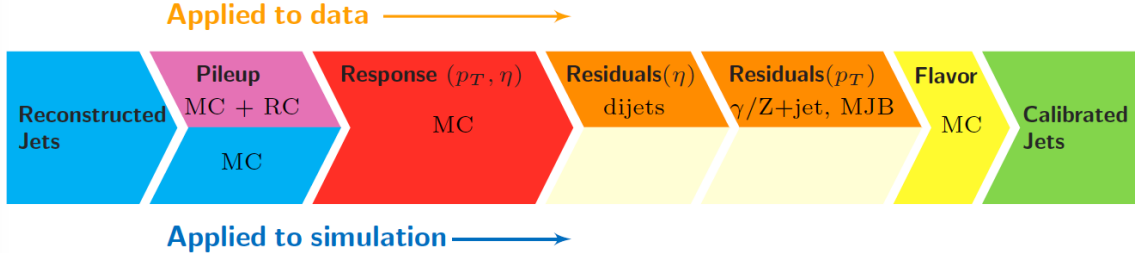


Figure 4.4: Jet energy correction diagram. Correction levels are applied sequentially in the indicated fixed order [117].

1797 Even though jets can be reconstructed efficiently, there are some effects that
 1798 are not included in the reconstruction that lead to discrepancies between the re-
 1799 constructed results and the predicted results; in order to overcome these discrep-
 1800 ancies, a factorized model has been designed in the form of jet energy corrections
 1801 (JEC) [116,117] applied sequentially as shown in the diagram of Figure 4.4.

1802 At each level, the jet four-momentum is multiplied by a scale factor based on jet
 1803 properties, i.e., η , flavor, etc.

- 1804 • Level 1 correction removes the energy coming from pile-up. The scale factor is
 1805 determined using a MC sample of QCD dijet (2 jets) events with and without
 1806 pileup overlay; it is parametrized in terms of the offset energy density ρ , jet
 1807 area A , jet η and jet p_T . Different corrections are applied to data and MC due
 1808 to the detector simulation.
- 1809 • MC-truth correction accounts for differences between the reconstructed jet en-
 1810 ergy and the MC particle-level energy. The correction is determined on a QCD
 1811 dijet MC sample and is parametrized in terms of the jet p_T and η .
- 1812 • Residuals correct remaining small differences within jet response in data and
 1813 MC. The Residuals η -dependent correction compares jets of similar p_T in the

1814 barrel reference region. The Residuals p_T -dependent corrects the jet absolute
 1815 scale (JES vs p_T).

- 1816 • Jet-flavor corrections are derived in the same way as MC-truth corrections but
 1817 using QCD pure flavor samples.

1818 ***b*-tagging of jets**

1819 A particular feature of the hadrons containing bottom quarks (*b*-hadrons) is that
 1820 their lifetime is long enough to travel some distance before decaying, but it is not as
 1821 long as those of light quark hadrons; therefore, when looking at the hadrons produced
 1822 in pp collisions, *b*-hadrons decay typically inside the tracker rather than reaching the
 1823 calorimeters as some light-hadrons do. As a result, a *b*-hadron decay gives rise to a
 1824 displaced vertex (secondary vertex) with respect to the primary vertex as shown in
 1825 Figure 4.5; the SV displacement is in the order of a few millimeters. A jet resulting
 1826 from the decay of a *b*-hadron is called *b* jet; other jets are called light jets.

1827

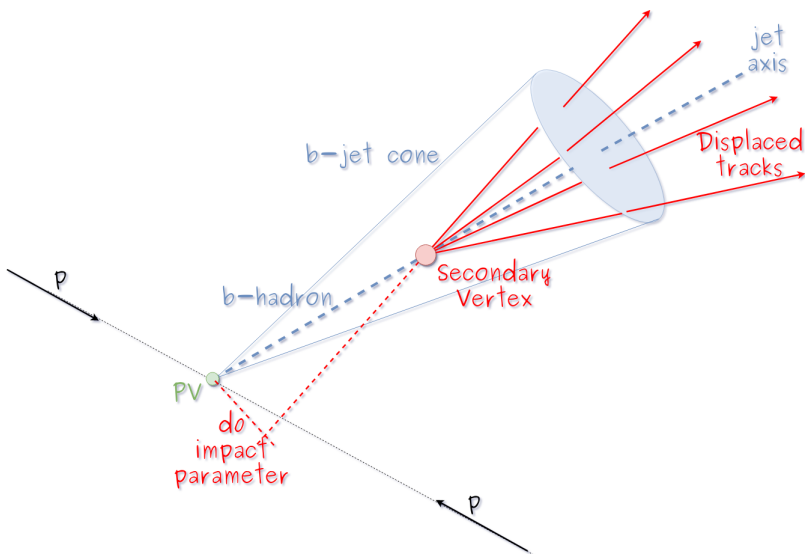


Figure 4.5: Secondary vertex in a *b*-hadron decay.

Several methods to identify b -jets (b -tagging) have been developed; the method used in this thesis is known as *Combined Secondary Vertex* algorithm in its second version (CSVv2) [118]. By using information of the impact parameter, the reconstructed secondary vertices, and the jet kinematics as input in a multivariate analysis that combines the discrimination power of each variable in one global discriminator variable, three working points (references): loose, medium and tight, are defined which quantify the probabilities of mistag jets from light quarks as jets from b quarks; 10, 1 and 0.1 % respectively. Although the mistagging probability decreases with the working point strength, the efficiency to correctly tag b -jets also decreases as 83, 69 and 49 % for the respective working point; therefore, a balance needs to be achieved according to the specific requirements of the analysis.

4.4.1.1 Missing transverse energy

The fact that proton bunches carry momentum along the z -axis only, implies that for each event it is expected that the momentum in the transverse plane is balanced. Imbalances are quantified by the missing transverse energy (MET) and are attributed to several sources including particles escaping undetected through the beam pipe, neutrinos produced in weak interactions processes which do not interact with the detector and thus escaping without leaving a sign, or even undiscovered particles predicted by models beyond the SM.

The PF algorithm assigns the negative sum of the momenta of all reconstructed PF particles to the *particle-flow MET* according to

$$\vec{E}_T = - \sum_i \vec{p}_{T,i} \quad (4.2)$$

JEC are propagated to the calculation of the \vec{E}_T as described in Reference [119].

1850 **4.4.2 Event reconstruction examples**

1851 Figures 4.6-4.8 show the results of the reconstruction performed on three recorded
 1852 events. Descriptions are taken directly from the source.

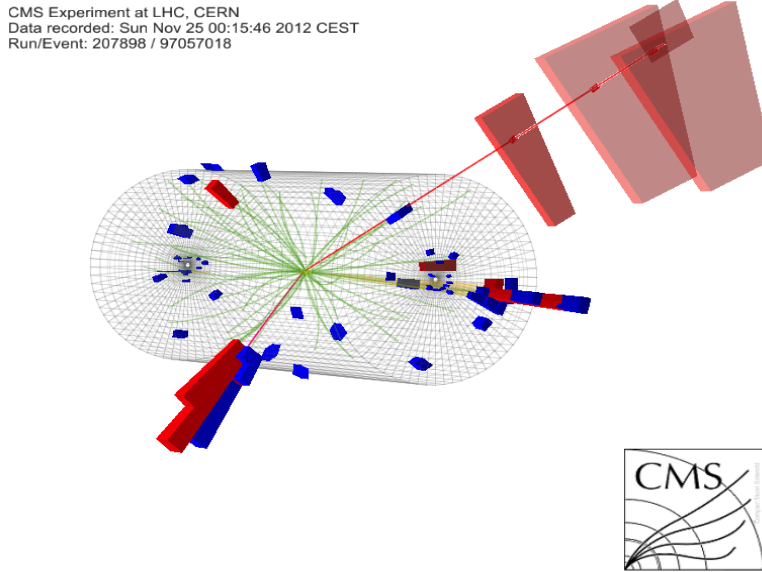


Figure 4.6: HIG-13-004 Event 1 reconstruction results; “HIG-13-004 Event 1: Event recorded with the CMS detector in 2012 at a proton-proton center-of-mass energy of 8 TeV. The event shows characteristics expected from the decay of the SM Higgs boson to a pair of τ leptons. Such an event is characterized by the production of two forward-going jets, seen here in opposite endcaps. One of the τ decays to a muon (red lines on the right) and neutrinos, while the other τ decays into a charged hadron and a neutrino.” [120].

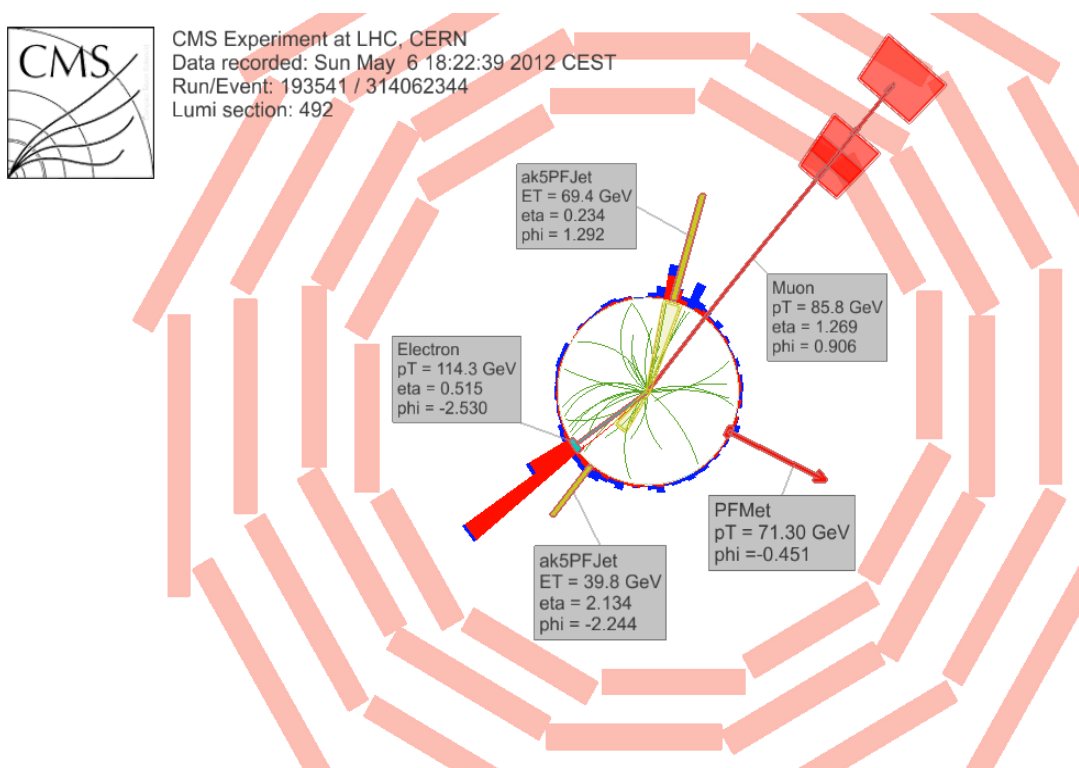


Figure 4.7: $e\mu$ event reconstruction results; “An $e\mu$ event candidate selected in 8 TeV data, as seen from the direction of the proton beams. The kinematics of the main objects used in the event selection are highlighted: two isolated leptons and two particle-flow jets. The reconstructed missing transverse energy is also displayed for reference” [121].

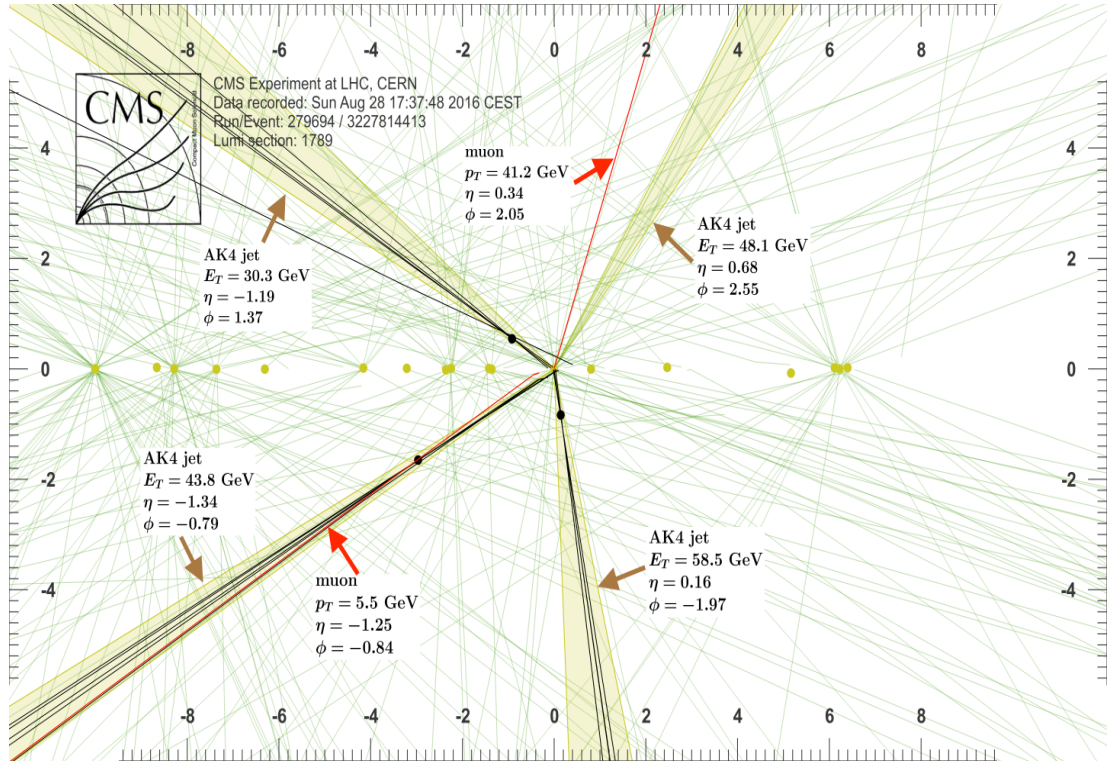


Figure 4.8: Recorded event reconstruction results; “Recorded event (ρ - z projection) with three jets with $p_T > 30$ GeV with one displaced muon track in 2016 data collected at 13 TeV. Each of the three jets has a displaced reconstructed vertex. The jet with $p_T(j) = 43.8$ GeV, $\eta(j) = -1.34$, $\phi(j) = -0.79$ contains muon with $p_T(\mu) = 5.5$ GeV, $\eta(\mu) = -1.25$, $\phi(\mu) = -0.84$. Event contains reconstructed isolated muon with $p_T(\mu) = 41.2$ GeV, $\eta(\mu) = 0.34$, $\phi(\mu) = 2.05$ and MET with $p_T = 72.5$ GeV, $\phi = -0.32$. Jet candidates for a b -jet from top quark leptonic and hadronic decays are tagged by CSVv2T algorithm. One of the other two jets is tagged by CharmT algorithm. Tracks with $p_T > 0.5$ GeV are shown. The number of reconstructed primary vertices is 18. Reconstructed $m_T(W)$ is 101.8 GeV. Beam spot position correction is applied. Reconstructed primary vertices are shown in yellow color, while reconstructed displaced vertices and associated tracks are presented in black color. Dimensions are given in cm” [122].

1853 **Chapter 5**

1854 **Statistical methods**

1855 In the course of analyzing the data sets provided by the CMS experiment and used in
1856 this thesis, several statistical tools have been employed; in this chapter, a description
1857 of these tools will be presented, starting with the general statement of the multivariate
1858 analysis method, followed by the particularities of the Boosted Decision Trees (BDT)
1859 method and its application to the classification problem. Statistical inference methods
1860 used will also be presented. This chapter is based mainly on the references [123–125].

1861 **5.1 Multivariate analysis**

1862 Multivariate data analysis (MVA) makes reference to statistical techniques that an-
1863 alyze data containing information of more than one variable, commonly taking into
1864 account the effects of all variables on the response of the particular variable under
1865 investigation, i.e., considering all the correlations between variables. MVA is em-
1866 ployed in a variety of fields like consumer and market research, quality control and
1867 process optimization. From a MVA it is possible to identify the dominant patterns
1868 in the data, like groups, outliers and trends, and determine to which group a set of

1869 values belong; in the particle physics context, MVA methods are used to perform the
 1870 selection of certain type of events, from a large data set, using a potentially large
 1871 number of measurable properties for each event.

1872 Processes with small cross section, as the tHq process, normally are hidden behind
 1873 more common processes; therefore, the data set results in a subset of events with
 1874 characteristic features of interest (signal) mixed in randomly with a much larger
 1875 number of SM events that can mimic these features of interest (background) which
 1876 implies that it is not possible to say with certainty that a given event is signal or
 1877 background. In that sense, the problem can be formulated as one where a set of
 1878 events have to be classified according to some features; these features correspond to
 1879 the measurements of several parameters like energy or momentum, organized in a
 1880 set of *input variables*. The measurements for each event can be written in a vector
 1881 $\mathbf{x} = (x_1, \dots, x_n)$ for which

- 1882 • Signal hypotheses $\rightarrow f(\mathbf{x}|s)$ is the probability density (*likelihood function*) that
 1883 \mathbf{x} is the set of measured values given that the events is a signal event.
- 1884 • Background hypotheses $\rightarrow f(\mathbf{x}|b)$ is the probability density (*likelihood function*)
 1885 that \mathbf{x} is the set of measured values given that the event is a background event.

1886 Figure 5.1 shows three ways to perform a classification of events for which mea-
 1887 surements of two properties, two input variables, have been performed; blue circles
 1888 represent signal events while red triangles represent background events. The classi-
 1889 fication on (a) is *cut-based* requiring $x_1 < c_1$ and $x_2 < c_2$; usually the cut values are
 1890 chosen according to some knowledge about the event process. In (b), the classification
 1891 is performed by stating a cut involving a linear function of the input variables and
 1892 so the boundary, while in (c) the the relationship between the input variables is not
 1893 linear thus the boundary is not linear either.

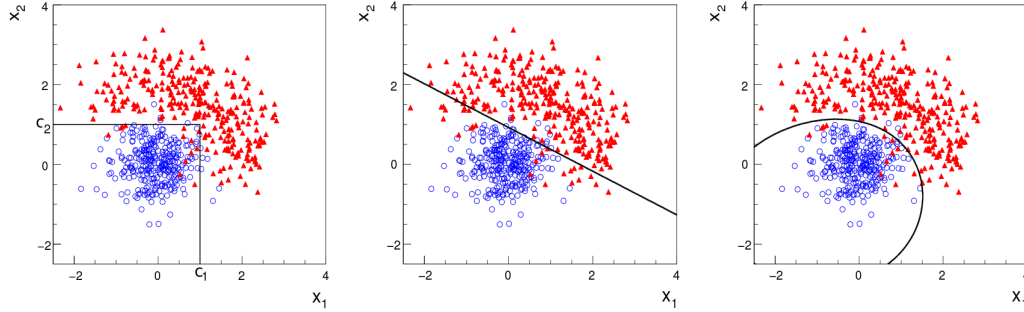


Figure 5.1: Scatter plots-MVA event classification. Distribution of two input variables x_1 and x_2 measured for a set of events; blue circles represent signal events and red triangles represent background events. The classification is based on (a) cuts, (b) linear boundary, and (c) nonlinear boundary [123]

1894 The boundary can be parametrized in terms of the input variables such that the
 1895 cut is set on the parametrization instead of on the variables, i.e., $y(\mathbf{x}) = y_{cut}$ with
 1896 y_{cut} a constant; thus, the acceptance or rejection of an event is based on what side
 1897 of the boundary is the event located. If $y(\mathbf{x})$ has functional form, it can be used to
 1898 determine the probability distribution functions $p(y|s)$ and $p(y|b)$ and then perform
 1899 a scalar test statistic with a single cut on the scalar variable y .

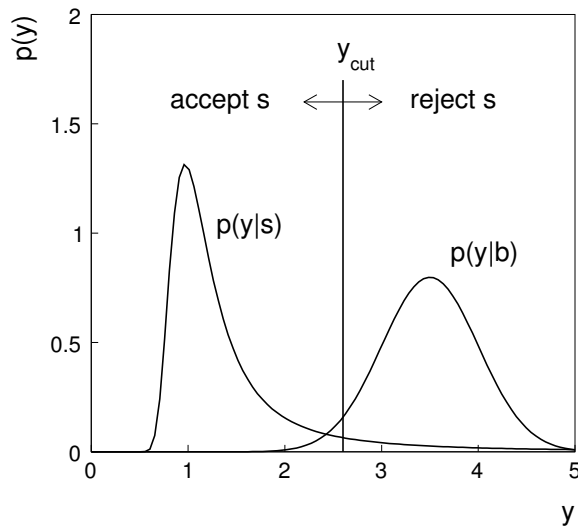


Figure 5.2: Distributions of the scalar test statistic $y(\mathbf{x})$ under the signal and background hypotheses. [123]

1900 Figure 5.2 illustrates what would be the probability distribution functions under
 1901 the signal and background hypotheses for a scalar test statistic with a cut on the
 1902 classifier y . Notice that the tails of the distributions indicate that some signal events
 1903 fall on the rejection region and some background events fall on the acceptance region;
 1904 therefore, it is convenient to define the *efficiency* with which events of a given type
 1905 are accepted, thus, the signal and background efficiencies are given by

$$\varepsilon_s = P(\text{accept event}|s) = \int_A f(\mathbf{x}|s) d\mathbf{x} = \int_{-\infty}^{y_{\text{cut}}} p(y|s) dy , \quad (5.1)$$

$$\varepsilon_b = P(\text{accept event}|b) = \int_A f(\mathbf{x}|b) d\mathbf{x} = \int_{-\infty}^{y_{\text{cut}}} p(y|b) dy , \quad (5.2)$$

1906 where A is the acceptance region. Under these conditions, the background hypothesis
 1907 corresponds to the *null hypothesis* (H_0), the signal hypothesis corresponds to the
 1908 *alternative hypothesis* (H_1), the background efficiency is the significance level of the
 1909 test, and signal efficiency is the power of the test; what is sought in an analysis is to
 1910 maximize the power of the test relative to the significance level.

1911 5.1.1 Decision trees

1912 For this thesis, the implementation of the MVA strategy, described above, is per-
 1913 formed through decision trees by using the TMVA software package [124] included in
 1914 the the ROOT analysis framework [126]. In a simple picture, a decision tree classifies
 1915 events according to their input variables values by setting a cut on each input variable
 1916 and checking which events are on which side of the cut, just as proposed in the MVA
 1917 strategy, but in addition, as a machine learning algorithm, decision trees offer the
 1918 possibility to be trained and then perform the classification efficiently.

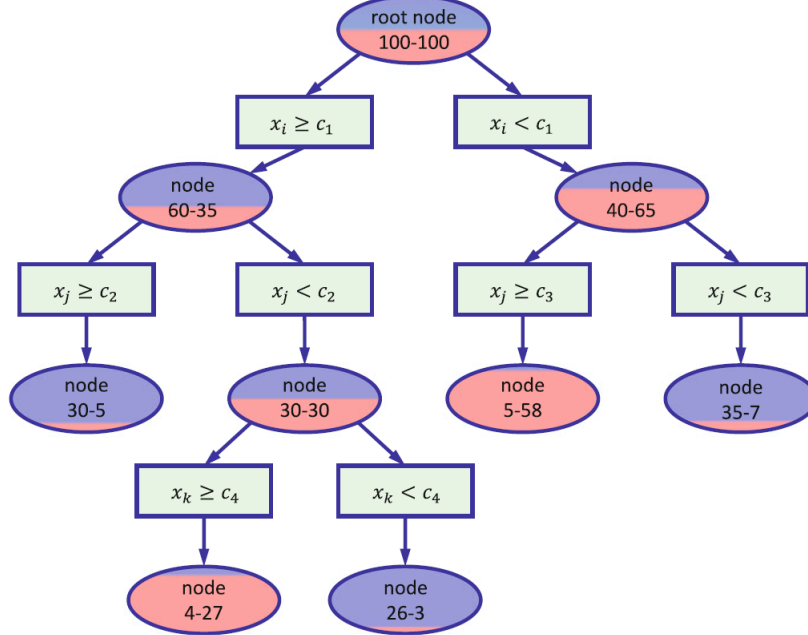


Figure 5.3: Example of a decision tree. Each node is fed with a MC sample mixing signal and background events (left-right numbers); nodes colors represent the relative amount of signal/background events [125].

1919 The training or growing of a decision tree is the process that defines the rules for
 1920 classifying events; this process is represented in figure 5.3 and consist of several steps

1921 • take MC samples of signal and background events and split them into two parts
 1922 each; first parts form the training sample which will be used in the decision tree
 1923 training, while the second parts form the test sample which will be used for
 1924 testing the final classifier obtained from the training. Each event has associated
 1925 a set of input variables $\mathbf{x} = (x_1, \dots, x_n)$ which serve to distinguish between signal
 1926 and background events. The training sample is taken in at the root *node*.

1927 • pick one variable, say x_i
 1928 • pick one value of x_i , each event has its own value of x_i , and split the training
 1929 sample into two subsamples B_1 and B_2 ; B_1 contains events for which $x_i < c_1$

1930 while B_2 contains the rest of the training events;

1931 • scan all possible values of x_i and find the splitting value that provides the *best*
 1932 classification¹, i.e., B_1 is mostly made of signal events while B_2 is mostly made
 1933 of background events.

1934 • It is possible that variables other than the picked one produce a better classi-
 1935 fication, hence, all the variables have to be evaluated. Pick the next variable,
 1936 say x_j , and repeat the scan over its possible values.

1937 • At the end, all the variables and their values will have been scanned, the *best*
 1938 variable and splitting value will have been identified, say x_1, c_1 , and there will
 1939 be two nodes fed with the subsamples B_1 and B_2 .

1940 Nodes are further split by repeating the decision process until: a given number of
 1941 final nodes is obtained, nodes are largely dominated by either signal or background
 1942 events, or nodes has too few events to continue. Final nodes are called *leaves* and they
 1943 are classified as signal or background leaves according to the class of the majority of
 1944 events in them. Each *branch* in the tree corresponds to a sequence of cuts.

1945 The quality of the classification at each node is evaluated through a separation
 1946 criteria; there are several of them but the *Gini Index* (G) is the one used in the
 1947 decision trees trained for the analysis in this thesis. G is written in terms of the
 1948 purity (P), i.e. the fraction of signal events, of the samples after the separation is
 1949 made; it is given by

$$G = P(1 - P) \quad (5.3)$$

¹ Quality of the classification will be treated in the next paragraph.

1950 notice that $P=0.5$ at the root node while $G=0$ for pure leaves. For a node A split
 1951 into two nodes B_1 and B_2 the G gain is

$$\Delta G = G(A) - G(B_1) - G(B_2) \quad (5.4)$$

1952 the *best* classification corresponds to that for which the gain of G is maximized; hence,
 1953 the scanning over all event's variables and their values is of capital importance.

1954 In order to provide a numerical output for the classification, events in a sig-
 1955 nal(background) leaf are assigned an score of 1(-1) each, defining in this way the
 1956 decision tree *classifier or weak learner* as

$$f(\mathbf{x}) = \begin{cases} 1 & \mathbf{x} \text{ in signal region,} \\ -1 & \mathbf{x} \text{ in background region.} \end{cases}$$

1957 Figure 5.4 shows an example of the classification of a sample of events, containing
 1958 two variables, performed by a decision tree.

1959 5.1.2 Boosted decision trees (BDT).

1960 Event misclassification occurs when a training event ends up in the wrong leaf, i.e., a
 1961 signal event ends up in a background leaf or a background event ends up in a signal
 1962 leaf. A way to correct it is to assign a weight to the misclassified events and train
 1963 a second tree using the reweighted events; the event reweighting is performed by a
 1964 boosting algorithm, events with increased weight are known as *boosted* events, in such
 1965 a way that when used in the training of a new decision tree they get correctly classified.
 1966 The process is repeated iteratively adding a new tree to a forest and creating a set
 1967 of classifiers which are combined to create the next classifier; the final classifier offers

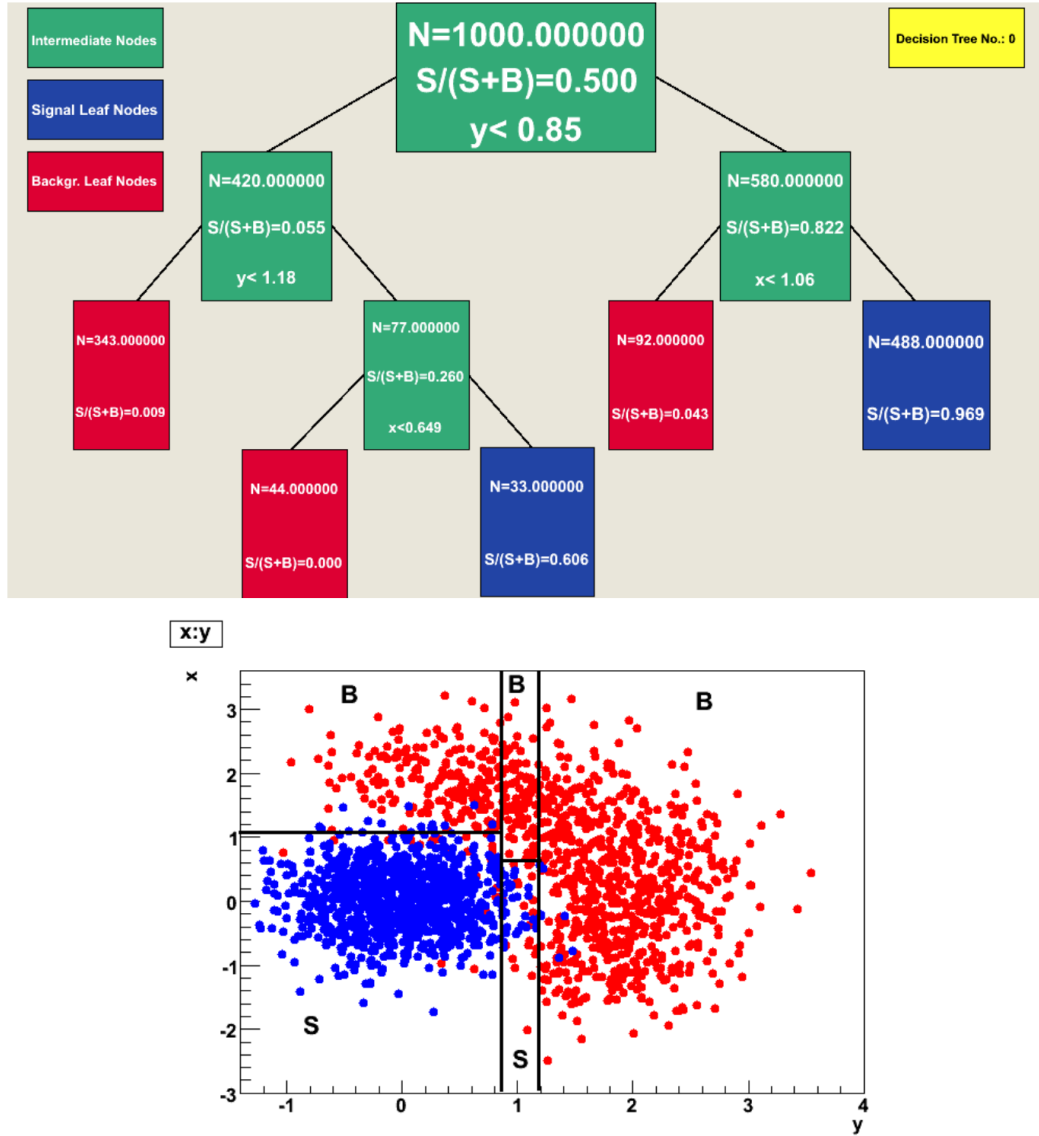


Figure 5.4: Example of a decision tree output. Each leaf, blue for signal events and red for background events, represent a region in the variables phase space [127].

1968 more stability² and has a smaller misclassification rate than any individual ones. The
 1969 resulting tree collection is known as a *boosted decision tree (BDT)*.
 1970 Thus, purity of the sample is generalized to

² Decision trees suffer from sensitivity to statistical fluctuations in the training sample which may leads to very different results with an small change in the training samples.

$$P = \frac{\sum_s w_s}{\sum_s w_s + \sum_b w_b} \quad (5.5)$$

1971 where w_s and w_b are the weights of the events; the Gini index is also generalized

$$G = \left(\sum_i^n w_i \right) P(1 - P) \quad (5.6)$$

1972 with n the number of events in the node. The final score of an event, after pass-
 1973 ing through the forest, is calculated as the renormalized sum of all the individual
 1974 (possibly weighted) scores; thus, high(low) score implies that the event is most likely
 1975 signal(background).

1976 The boosting procedure, implemented in the *Gradient boosting* algorithm used
 1977 in this thesis, produce a classifier $F(\mathbf{x})$ which is the weighted sum of the individual
 1978 classifiers obtained after each iteration,i.e.,

$$F(\mathbf{x}) = \sum_{m=1}^M \beta_m f(\mathbf{x}; a_m) \quad (5.7)$$

1979 where M is the number of trees in the forest. The *loss function* $L(F, y)$ represent the
 1980 deviation between the classifier $F(\mathbf{x})$ response and the true value y obtained from the
 1981 training sample (1 for signal events and -1 for background event), according to

$$L(F, y) = \ln(1 + e^{-2F(\mathbf{x})y}) \quad (5.8)$$

1982 thus, the reweighting is employed to ensure the minimization of the loss function;
 1983 a more detailed description of the minimization procedure can be found in reference
 1984 [128]. The final classifier output is later used as a final discrimination variable, labeled
 1985 as *BDT output/response*.

1986 **5.1.3 Overtraining.**

1987 Decision trees offer the possibility to have as many nodes as wished in order to
 1988 reduce the misclassification to zero (in theory); however, when a classifier is too much
 1989 adjusted to a particular training sample, the classifier response to a slightly different
 1990 sample may leads to a completely different classification results; this effect is known
 1991 as *overtraining*.

1992 An alternative to reduce the overtraining in BDTs consist in pruning the tree by
 1993 removing statistically insignificant nodes after the tree growing is completed but this
 1994 option is not available for BDTs with gradient boosting in the TMVA-toolkit, there-
 1995 fore, the overtraining has to be reduced by tuning the algorithm, number of nodes,
 1996 minimum number of events in the leaves, etc. The overtraining can be evaluated
 1997 by comparing the responses of the classifier when running over the training and test
 1998 samples.

1999 **5.1.4 Variable ranking.**

2000 BDTs have the couple of particular advantages related to the input variables; on one
 2001 side, they are relatively insensitive to the number of input variables used in the vector
 2002 \mathbf{x} . The ranking of the BDT input variables is determined by counting the number of
 2003 times a variable is used to split decision tree nodes; in addition, the separation gain-
 2004 squared achieved in the splitting and the number of events in the node are accounted
 2005 by applying a weighting to that number. Thus, those variables with small or no power
 2006 to separate signal and background events are rarely chosen to split the nodes,i.e., are
 2007 effectively ignored.

2008 On the other side, variables correlations play an important role for some MVA
 2009 methods like the Fisher discriminant algorithm in which the first step consist of

2010 performing a linear transformation to a phase space where the correlations between
 2011 variables are removed; in case of BDT algorithm, correlations do not affect the per-
 2012 formance.

2013 **5.1.5 BDT output example.**

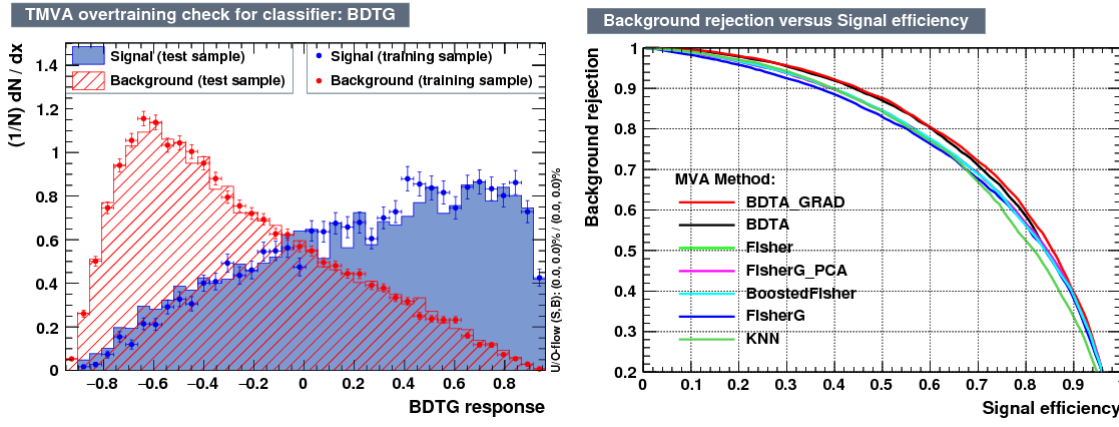


Figure 5.5: Left: Output distributions for the gradient boosted decision tree (BDTG) classifier using a sample of signal($pp \rightarrow tHq$) and background($pp \rightarrow t\bar{t}$) events. Right: Background rejection vs signal efficiency (ROC curves) for various MVA classifiers running over the same sample used to produce the plot on the left.

2014 Left side of figure 5.5 shows the BDT output distributions for signal($pp \rightarrow tHq$)
 2015 and background($pp \rightarrow t\bar{t}$) events; this plot is the equivalent to the one showed in
 2016 figure 5.2. A forest with 800 trees, maximum depth per tree = 3, and gradient
 2017 boosting have been used as training parameters. The BDTG classifier offers a good
 2018 separation power; while there is a small overtraining in the signal distribution, the
 2019 background distribution seems to be well predicted which might indicate that the
 2020 sample is composed of more background than signal events.

2021 Right side of figure 5.5 shows the background rejection vs signal efficiency curves
 2022 for several combinations of MVA classifiers-boosting algorithms; these curves are
 2023 known as ROC curves and give an indication of the performance of the classifier. The

2024 best performance is achieved with the BDTG classifier (BDTA_GRAD).

2025 5.2 Statistical inference.

2026 Once events are classified, the next step consists in finding the parameters that define
 2027 the likelihood functions $f(\mathbf{x}|s), f(\mathbf{x}|b)$ for signal and background events respectively.
 2028 In general, likelihood functions depend not only on the measurements but also on
 2029 parameters (θ_m) that define their shapes; the process of estimating these *unknown*
 2030 *parameters* and their uncertainties from the experimental data is called *inference*.
 2031 The likelihood function for N the events the in a sample is the combination of all the
 2032 likelihoods functions

$$L(\boldsymbol{\theta}) = \prod_{i=1}^N f(\mathbf{x}^i | \boldsymbol{\theta}) = \prod_{i=1}^N f(x_1^i, \dots, x_n^i; \theta_1, \dots, \theta_m) \quad (5.9)$$

2033 Thus, the estimation of the unknown parameters from experimental data samples
 2034 is written in terms of a central value using the notation

$$\theta = \hat{\theta} \pm \delta\theta \quad (5.10)$$

2035 where the interval $[\hat{\theta} + \delta\theta, \hat{\theta} - \delta\theta]$ is called *confidence interval*; it is usually inter-
 2036 preted, in the limit of infinite number of experiments, as the interval where the true
 2037 value of the unknown parameter θ is contained with a probability of 0.6827 (if no
 2038 other convention is stated).

2039 5.2.1 Nuisance parameters.

2040 The unknown parameter vector $\boldsymbol{\theta}$ is made of two types of parameters: on one side,
 2041 those parameters that provide information about the physical observables of interest

2042 for the experiment (*parameters of interest*); on the other side, the *nuisance parameters*
 2043 that are not of direct interest for the experiment but that needs to be included in
 2044 the analysis in order to achieve a satisfactory description of the data. They represent
 2045 effects of the detector response like the finite resolutions of the detection systems,
 2046 miscalibrations, and in general any source of uncertainty introduced in the analysis.

2047 In some cases the nuisance parameters are estimated using dedicated data samples,
 2048 for instance data from test beams for calibration purposes, when MC samples are
 2049 not suitable. The nuisance parameter uncertainties produce *systematic uncertainties*
 2050 while the uncertainties associated to fluctuations in data and related to the estimation
 2051 of the parameters of interest produce *statistical uncertainties*.

2052 5.2.2 Maximum likelihood estimation method

2053 The function that produce the estimate of a parameter is called *estimator*, there-
 2054 fore, estimators are usually constructed using mathematical procedures encoded in
 2055 algorithms. The estimation method used in this thesis is the *Maximum Likelihood*
 2056 *Estimation* method (MLE); it is based on the combined likelihood function defined
 2057 by eqn. 5.9 and the procedure seeks for the parameter set that corresponds to the
 2058 maximum value of the combined likelihood function, i.e., the *maximum likelihood*
 2059 *estimator* of the unknown parameter vector $\boldsymbol{\theta}$ is the function that produce the vec-
 2060 tor $\hat{\boldsymbol{\theta}}$ for which the likelihood function $L(\boldsymbol{\theta})$ evaluated at the measured sample \mathbf{x} is
 2061 maximum.

2062 Usually, the logarithm of the likelihood function is used in the numerical algo-
 2063 rithms implementations in order to avoid underflow the numerical precision of the
 2064 computers due to the product of low likelihoods. In addition, it is usual minimize the
 2065 negative logarithm of the likelihood function instead of maximizing the logarithm of

2066 it because in this way the procedure consist of differentiate a sum of therms and set
 2067 the sum to zero; therefore

$$F(\boldsymbol{\theta}) = -\ln L(\boldsymbol{\theta}) = -\sum_{i=1}^N f(\mathbf{x}^i | \boldsymbol{\theta}). \quad (5.11)$$

2068 The minimization process is performed by the software MINUIT [129] imple-
 2069 mented in the ROOT analysis framework. In case of large data samples the compu-
 2070 tational resources needed to calculate the likelihood function are too big; therefore,
 2071 the parameter estimation is performed using binned distributions of the variables of
 2072 interest for which the *binned likelihood function* is given by

$$L(data|\mu, \theta) = \prod_{i=1} \frac{(\mu s_i(\theta) + b_i(\theta))^{n_i}}{n_i!} e^{-\mu s_i(\theta) - b_i(\theta)}, \quad (5.12)$$

2073 with s_i and b_i the expected number of signal and background yields for bin i respec-
 2074 tively, n_i is the observed number of events in the bin i and $\mu = \sigma/\sigma_{SM}$ is the signal
 2075 strength. Notice that the number of entries per bin follows a Poisson distribution.
 2076 The analysis presented in this thesis is based on the binned distribution of the ratio
 2077 signal/background obtained from the BDT outputs.

2078 5.2.3 Hypothesis test

2079 The test statistic mentioned in section 5.1 involving
 2080 ; it is achieved, according to the Neyman-Pearson lemma [130],
 2081 by defining the acceptance region such that, for \mathbf{x} inside the region, the likelihood
 2082 ratio, i.e., the ratio of probability distribution functions for signal and background,

2083 **5.3 exclusion limits**

2084 **5.4 asymptotic limits**

2085 **Chapter 6**

2086 **Search for production of a Higgs
2087 boson and a single top quark in
2088 multilepton final states in pp
2089 collisions at $\sqrt{s} = 13$ TeV**

2090 **6.1 Introduction**

2091 The Higgs boson discovery, supported on experimental observations and theoretical
2092 predictions made about the SM, gives the clue of the way in that elementary particles
2093 acquire mass through the Higgs mechanism; therefore, knowing the Higgs mass, the
2094 Higgs-boson and Higgs-fermion couplings can be tested. In order to test the Higgs-top
2095 coupling, several measurements have been performed, as stated in the chapter 2, but
2096 they are limited to measure the square of the coupling; however, the production of a
2097 Higgs boson in association with a single top quark (tH) not only offers access to the
2098 sign of the coupling, but also, to the CP phase of the Higgs couplings.

2099 This chapter presents the search for the associated production of a Higgs boson
 2100 and a single top quark events, focusing on leptonic signatures provided by the Higgs
 2101 decay modes to WW , ZZ , and $\tau\tau$; the 13 TeV dataset produced in 2016, which
 2102 corresponds to an integrated luminosity of 35.9fb^{-1} , is used. Constraints on the sign
 2103 of the Higgs-top coupling (y_t) have been derived from the decay rate of Higgs boson
 2104 to photon pairs [50] and from the cross section for associated production of Higgs and
 2105 Z bosons via gluon fusion [131], with recent results disfavoring negative signs of the
 2106 coupling [44, 59, 132]. It expands previous analyses performed at 8 TeV [133, 134] and
 2107 searches for associated production of $t\bar{t}$ pair and a Higgs boson in the multilepton final
 2108 state channel [135]; it also complements searches in other decay channels targeting
 2109 $H \rightarrow b\bar{b}$ [136].

2110 As shown in section 2.5, the SM cross section of the associated production of a
 2111 Higgs boson and a single top quark (tHq) process is driven by a destructive interfer-
 2112 ence between two contributions (see Figure 2.15), where the Higgs couples to either
 2113 the W boson or the top quark; however, if the sign of the Higgs-top coupling is flipped
 2114 with respect to the SM prediction, a large enhancement of the cross section occurs,
 2115 making this analysis sensitive to such deviation. A second process, where the Higgs
 2116 boson and top quark are accompanied by a W boson (tHW) has similar behavior,
 2117 albeit with a weaker interference pattern and lower contribution to the tH cross sec-
 2118 tion, therefore, a combination of both processes would increase the sensitivity; in
 2119 this analysis both contributions are combined and referred as tH channel. A third
 2120 contribution comes from $t\bar{t}H$ process. The purpose of this analysis is to investigate
 2121 the exclusion of the presence of the $tH + t\bar{t}H$ processes under the assumption of the
 2122 anomalous Higgs-top coupling modifier ($\kappa_t = -1$). The analysis exploits signatures
 2123 with two leptons of the same sign (*2lss channel*) and three leptons (*3l channel*) in
 2124 the final state.

2125 The first sections present the characteristic tHq signature as well as the expected
 2126 backgrounds. The MC samples, data sets, and the physics object definitions are
 2127 then defined. Following, the background predictions, the signal extraction, and the
 2128 statistical treatment of the selected events as well as the systematic uncertainties are
 2129 described. The final section present the results for the exclusion limits as a function
 2130 of the ratio of κ_t and the dimensionless modifier of the Higgs-vector boson κ_V .

2131 6.2 tHq signature

2132 In order to select events of tHq process, its features are translated into a set of
 2133 selection rules; figure 6.1 shows the Feynman diagram and an schematic view of the
 2134 tHq process from the pp collision to the final state configuration. A single top quark
 2135 is produced accompanied by a light quark, denoted as q ; this light quark is produced
 2136 predominantly in the forward region of the detector. The Higgs boson which can
 2137 be either emitted by the exchanged W boson or directly by the singly produced top
 2138 quark.

2139 The top quark and Higgs boson decay after their production in the detector due to
 2140 their high masses/low lifetimes. The Higgs boson is required to decay into a W boson
 2141 pair¹. The top quark almost always decays into a bottom quark and a W boson, as
 2142 encoded in the CMK matrix. The W bosons are required to decay hadronically in
 2143 the 2lss channel case and leptonically in the 3l channel case, while τ leptons are not
 2144 reconstructed separately and only their leptonic decays into either electrons or muons
 2145 are considered in this analysis.

2146 In summary, the signal process is characterized by a the final state with

- 2147 • one light-flavored forward jet,

¹ ZZ and $\tau\tau$ decays are also include in the analysis but they are not separately reconstructed

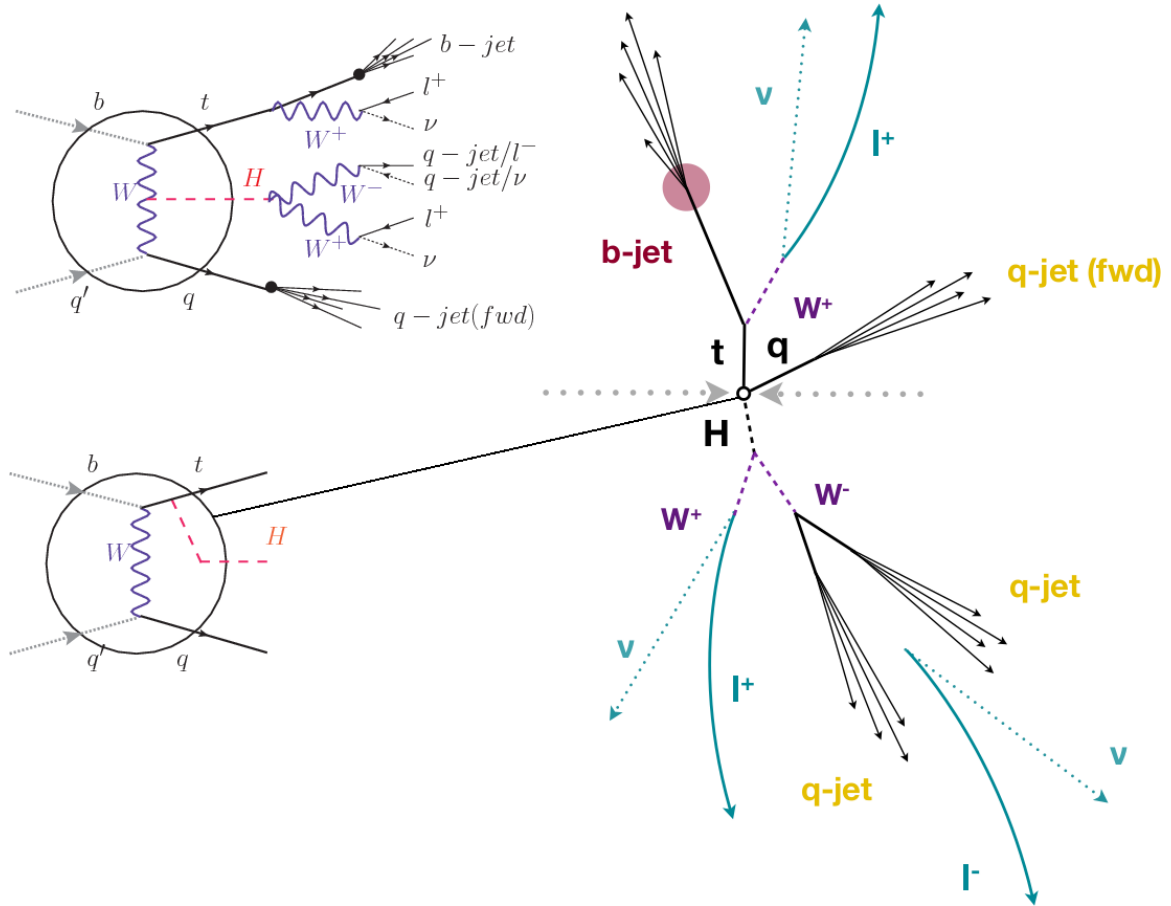


Figure 6.1: tHq event signature. Left: Feynman diagram including the whole evolution up to the final state for the case of the Higgs boson emitted by the W boson (top); Feynman diagram for the case where the Higgs boson is emitted by the top quark. Right: Schematic view as it would be seen in the detector; the circle in the Feynman diagrams on the left corresponds to the circle in the center of the schematic view as indicated by the line connecting them. In the 2lss channel, one of the W bosons from the Higgs boson decays to two light-quark jets while in the 3l channel both W bosons decays to leptons.

- 2148 • one central b-jet,
 - 2149 • 2lss channel \rightarrow two leptons of the same sign, two neutrinos and two light (often
2150 soft) jets,
 - 2151 • 3l channel \rightarrow three leptons, three neutrinos and no central light-flavored jets,
- 2152 The presence of neutrinos is inferred from the presence of MET. The analysis has

2153 been made public by CMS as a Physics Analysis Summary [137] combining the result
 2154 for the three lepton and two lepton same-sign channels. Currently, an effort to turn
 2155 the analysis into a paper is ongoing.

2156 **6.3 Background processes**

2157 The background processes are those that can mimic the signal signature or at least
 2158 can be reconstructed as that as a result of certain circumstances. The backgrounds
 2159 can be classified as

- 2160 • Irreducible backgrounds where genuine prompt leptons are produced in on-
 2161 shell W and Z boson decays; they can be reliably estimated directly from MC
 2162 simulated events, using higher-order cross sections or data control regions for
 2163 the overall normalization.
- 2164 • Reducible backgrounds where at least one of the leptons is *non-prompt*, i.e., pro-
 2165 duced within a hadronic jet, either a genuine lepton from heavy flavor decays.
 2166 misreconstructed jets, also known as *mis-ID leptons* or *fake leptons*, are consid-
 2167 ered non-prompt leptons as well. These non-prompt leptons leave tracks and
 2168 hits in the detection systems as would a prompt lepton, but correlating those
 2169 hits with nearby jets could be a way of removing them. Reducible backgrounds
 2170 are not well predicted by simulation, and are estimated using data-driven meth-
 2171 ods.

2172 The main sources of background events in the case of tHq process are $t\bar{t}$ process
 2173 and $t\bar{t} + X(X = W, Z, \gamma)$ processes, here represented together as $t\bar{t}V$ process. Figure
 2174 6.2 shows the signature for $t\bar{t}$ and $t\bar{t}W$ processes;

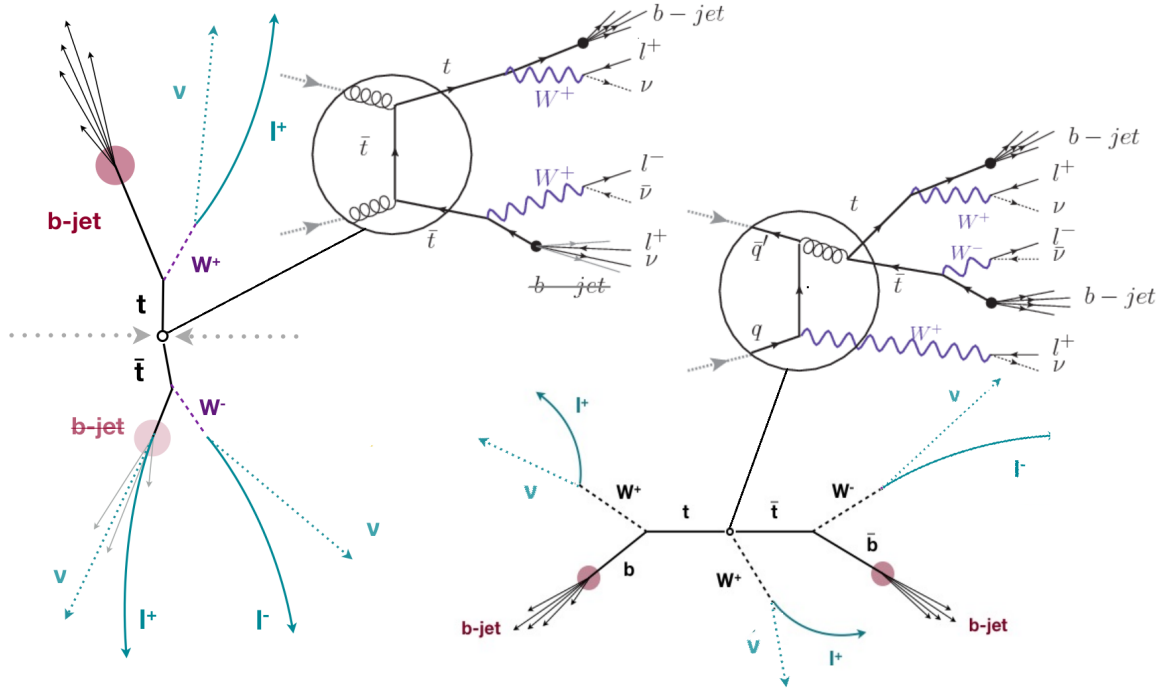


Figure 6.2: $t\bar{t}$ (left) and $t\bar{t}W$ (right) events signature as they would be seen in the detector; the Feynman diagrams including the whole evolution up to the final state are also showed. The $t\bar{t}$ process signature is very similar to that of the signal process with one fake lepton and no forward activity. The $t\bar{t}W$ process present a higher b-jet multiplicity compared to the signal process, a prompt lepton and no forward activity.

2175 The largest contribution to irreducible backgrounds involving prompt leptons
 2176 comes from $t\bar{t}W$, $t\bar{t}Z$, processes for which the number of ($b-$)jets (($b-$)jet multiplicity)
 2177 is higher than that of the signal events, while for other contributing background
 2178 events, WZ , ZZ , and rare SM processes like $W^\pm W^\pm qq$, $t\bar{t}t\bar{t}$, tZq , tZW , WWW ,
 2179 WWZ , WZZ , ZZZ , the ($b-$)jet multiplicity is lower compared to that of the signal
 2180 events. None of the irreducible backgrounds present activity in the forward region of
 2181 the detector.

2182 On the side of the reducible backgrounds, the largest contribution comes from the
 2183 $t\bar{t}$ events which have a very similar signature to the signal events but does not present
 2184 activity in the forward region of the detector either; A particular feature of the $t\bar{t}$
 2185 events is their charge-symmetry which is also a difference with the signal events.

2186 The charge misidentification plays an important role in the the 2lss channel since
 2187 leptons in processes like $t\bar{t}$ + jets or Z + jets can be charge misidentified, leading to
 2188 backgrounds increments. An identification variable have been designed in order to
 2189 reject this type of background events.

2190 **6.4 Data and MC Samples**

2191 Technical developments on the event generator side allow for an event-wise reweight-
 2192 ing that can change the event kinematics based on specific generation parameters.
 2193 This way not only the case of $C_t = \sqrt{2}$, but a whole range of κ_t and κ_V values can
 2194 be investigated.

2195 The data considered in this analysis were collected by the CMS experiment dur-
 2196 ing 2016 and correspond to a total integrated luminosity of $35.9 fb^{-1}$. Only periods
 2197 when the CMS magnet was on were considered when selecting the data samples, that
 2198 corresponds to the 23 Sep 2016 (Run B to G) and PromptReco (Run H) versions
 2199 of the datasets. The MC samples used in this analysis correspond to the RunI-
 2200 ISummer16MiniAODv2 campaign produced with CMSSW 80X. The two signal sam-
 2201 ples (for tHq and tHW) were produced with MG5_aMC@NLO (version 5.222), in
 2202 leading-order order mode, and are normalized to next-to-leading-order cross sections,
 2203 see Tab. 6.1. Each sample is generated with a set of event weights corresponding to
 2204 different values of κ_t and κ_V couplings as shown in Tab. 6.2.

2205 **6.4.1 Full 2016 dataset and MC samples**

2206 Different MC generators were used to generate the background processes. The dom-
 2207 inant sources ($t\bar{t}$, $t\bar{t}W$, $t\bar{t}Z$, $t\bar{t}H$) were produced using AMC@NLO interfaced to
 2208 PYTHIA8, and are scaled to NLO cross sections. Other processes are simulated us-

Sample	σ [pb]	BF
/THQ_Hincl_13TeV-madgraph-pythia8_TuneCUETP8M1/	0.7927	0.324
/THW_Hincl_13TeV-madgraph-pythia8_TuneCUETP8M1/	0.1472	1.0

Table 6.1: Signal samples and their cross section and branching fraction used in this analysis. See Ref. [146] for more details.

2209 ing POWHEG interfaced to PYTHIA, or bare PYTHIA (see table 6.3 and [135] for
 2210 more details).

2211 6.4.2 Triggers

2212 We consider online-reconstructed events triggered by one, two, or three leptons.
 2213 Single-lepton triggers are included to boost the acceptance of events where the p_T of
 2214 the sub-leading lepton falls below the threshold of the double-lepton triggers. Ad-
 2215 ditionally, by including double-lepton triggers in the ≥ 3 lepton category, as well
 2216 as single-lepton triggers in all categories, we increase the efficiency, considering the
 2217 logical “or” of the trigger decisions of all the individual triggers in a given category.
 2218 Tab. 6.5 shows the lowest-threshold non-prescaled triggers present in the High-Level
 2219 Trigger (HLT) menus for both Monte-Carlo and data in 2016.

2220 Trigger efficiency scale factors

2221 The efficiency of events to pass the trigger is measured in simulation (trivially using
 2222 generator information) and in the data (using event collected by an uncorrelated
 2223 MET trigger). Small differences between the data and MC efficiencies are corrected
 2224 by applying scale factors as shown in Tab. 6.6. The exact procedure and control plots
 2225 are documented in [140] for the current analysis.

		<i>tHq</i>		<i>tHW</i>		
κ_V	κ_t	sum of weights	cross section [pb]	sum of weights	cross section [pb]	LHE weights
1.0	-3.0	35.700022	2.991	11.030445	0.6409	LHEweight_wgt[446]
1.0	-2.0	20.124298	1.706	5.967205	0.3458	LHEweight_wgt[447]
1.0	-1.5	14.043198	1.205	4.029093	0.2353	LHEweight_wgt[448]
1.0	-1.25	11.429338	0.9869	3.208415	0.1876	LHEweight_wgt[449]
1.0	-1.0		0.7927		0.1472	
1.0	-0.75	7.054998	0.6212	1.863811	0.1102	LHEweight_wgt[450]
1.0	-0.5	5.294518	0.4723	1.339886	0.07979	LHEweight_wgt[451]
1.0	-0.25	3.818499	0.3505	0.914880	0.05518	LHEweight_wgt[452]
1.0	0.0	2.627360	0.2482	0.588902	0.03881	LHEweight_wgt[453]
1.0	0.25	1.719841	0.1694	0.361621	0.02226	LHEweight_wgt[454]
1.0	0.5	1.097202	0.1133	0.233368	0.01444	LHEweight_wgt[455]
1.0	0.75	0.759024	0.08059	0.204034	0.01222	LHEweight_wgt[456]
1.0	1.0	0.705305	0.07096	0.273617	0.01561	LHEweight_wgt[457]
1.0	1.25	0.936047	0.0839	0.442119	0.02481	LHEweight_wgt[458]
1.0	1.5	1.451249	0.1199	0.709538	0.03935	LHEweight_wgt[459]
1.0	2.0	3.335034	0.2602	1.541132	0.08605	LHEweight_wgt[460]
1.0	3.0	10.516125	0.8210	4.391335	0.2465	LHEweight_wgt[461]
1.5	-3.0	45.281492	3.845	13.426212	0.7825	LHEweight_wgt[462]
1.5	-2.0	27.606715	2.371	7.809713	0.4574	LHEweight_wgt[463]
1.5	-1.5	20.476088	1.784	5.594971	0.3290	LHEweight_wgt[464]
1.5	-1.25	17.337465	1.518	4.635978	0.2749	LHEweight_wgt[465]
1.5	-1.0	14.483302	1.287	3.775902	0.2244	LHEweight_wgt[466]
1.5	-0.75	11.913599	1.067	3.014744	0.1799	LHEweight_wgt[467]
1.5	-0.5	9.628357	0.874	2.352505	0.1410	LHEweight_wgt[468]
1.5	-0.25	7.627574	0.702	1.789184	0.1081	LHEweight_wgt[469]
1.5	0.0	5.911882	0.5577	1.324946	0.08056	LHEweight_wgt[470]
1.5	0.25	4.479390	0.4365	0.959295	0.05893	LHEweight_wgt[471]
1.5	0.5	3.331988	0.3343	0.692727	0.04277	LHEweight_wgt[472]
1.5	0.75	2.469046	0.2558	0.525078	0.03263	LHEweight_wgt[473]
1.5	1.0	1.890565	0.2003	0.456347	0.02768	LHEweight_wgt[474]
1.5	1.25	1.596544	0.1689	0.486534	0.02864	LHEweight_wgt[475]
1.5	1.5	1.586983	0.1594	0.615638	0.03509	LHEweight_wgt[476]
1.5	2.0	2.421241	0.2105	1.170602	0.06515	LHEweight_wgt[477]
1.5	3.0	7.503280	0.5889	3.467546	0.1930	LHEweight_wgt[478]
0.5	-3.0	27.432685	2.260	8.929074	0.5136	LHEweight_wgt[479]
0.5	-2.0	13.956013	1.160	4.419093	0.2547	LHEweight_wgt[480]
0.5	-1.5	8.924438	0.7478	2.757611	0.1591	LHEweight_wgt[481]
0.5	-1.25	6.835341	0.5726	2.075247	0.1204	LHEweight_wgt[482]
0.5	-1.0	5.030704	0.4273	1.491801	0.08696	LHEweight_wgt[483]
0.5	-0.75	3.510528	0.2999	1.007273	0.05885	LHEweight_wgt[484]
0.5	-0.5	2.274811	0.1982	0.621663	0.03658	LHEweight_wgt[485]
0.5	-0.25	1.323555	0.1189	0.334972	0.01996	LHEweight_wgt[486]
0.5	0.0	0.656969	0.06223	0.147253	0.008986	LHEweight_wgt[487]
0.5	0.25	0.274423	0.02830	0.058342	0.003608	LHEweight_wgt[488]
0.5	0.5	0.176548	0.01778	0.068404	0.003902	LHEweight_wgt[489]
0.5	0.75	0.363132	0.03008	0.177385	0.009854	LHEweight_wgt[490]
0.5	1.0	0.834177	0.06550	0.385283	0.02145	LHEweight_wgt[491]
0.5	1.25	1.589682	0.1241	0.692099	0.03848	LHEweight_wgt[492]
0.5	1.5	2.629647	0.2047	1.097834	0.06136	LHEweight_wgt[493]
0.5	2.0	5.562958	0.4358	2.206057	0.1246	LHEweight_wgt[494]
0.5	3.0	14.843102	1.177	5.609519	0.3172	LHEweight_wgt[495]

Table 6.2: κ_V and κ_t combinations generated for the two signal samples and their NLO cross sections. The *tHq* cross section is multiplied by the branching fraction of the enforced leptonic decay of the top quark (0.324). See also Ref. [146].

Sample	σ [pb]
TTWJetsToLNu_TuneCUETP8M1_13TeV-amcatnloFXFX-madspin-pythia8	0.2043
TTZToLLNuNu_M-10_TuneCUETP8M1_13TeV-amcatnlo-pythia8	0.2529
ttHJetToNonbb_M125_13TeV_amcatnloFXFX_madspin_pythia8_mWCutfix /store/cmst3/group/susy/gpetrucc/13TeV/u/TTLL_m1to10_LO_NoMS_for76X/	0.2151 0.0283
WGToLNuG_TuneCUETP8M1_13TeV-madgraphMLM-pythia8	585.8
ZGTo2LG_TuneCUETP8M1_13TeV-amcatnloFXFX-pythia8	131.3
TGJets_TuneCUETP8M1_13TeV_amcatnlo_madspin_pythia8	2.967
TGJets_TuneCUETP8M1_13TeV_amcatnlo_madspin_pythia8	2.967
TTGJets_TuneCUETP8M1_13TeV-amcatnloFXFX-madspin-pythia8	3.697
WpWpJJ_EWK-QCD_TuneCUETP8M1_13TeV-madgraph-pythia8	0.03711
ZZZ_TuneCUETP8M1_13TeV-amcatnlo-pythia8	0.01398
WWZ_TuneCUETP8M1_13TeV-amcatnlo-pythia8	0.1651
WZZ_TuneCUETP8M1_13TeV-amcatnlo-pythia8	0.05565
WW_DoubleScattering_13TeV-pythia8	1.64
tZq_ll_4f_13TeV-amcatnlo-pythia8_TuneCUETP8M1	0.0758
ST_tWll_5f_LO_13TeV-MadGraph-pythia8	0.01123
TTTT_TuneCUETP8M1_13TeV-amcatnlo-pythia8	0.009103
WZTo3LNu_TuneCUETP8M1_13TeV-powheg-pythia8	4.4296
ZZTo4L_13TeV_powheg_pythia8	1.256
TTJets_SingleLeptFromTbar_TuneCUETP8M1_13TeV-madgraphMLM-pythia8	182.1754
TTJets_SingleLeptFromT_TuneCUETP8M1_13TeV-madgraphMLM-pythia8	182.1754
TTJets_DiLept_TuneCUETP8M1_13TeV-madgraphMLM-pythia8	87.3
DYJetsToLL_M-10to50_TuneCUETP8M1_13TeV-amcatnloFXFX-pythia8	18610
DYJetsToLL_M-50_TuneCUETP8M1_13TeV-madgraphMLM-pythia8	6024
WJetsToLNu_TuneCUETP8M1_13TeV-amcatnloFXFX-pythia8	61526.7
ST_tW_top_5f_inclusiveDecays_13TeV-powheg-pythia8_TuneCUETP8M1	35.6
ST_tW_antitop_5f_inclusiveDecays_13TeV-powheg-pythia8_TuneCUETP8M1	35.6
ST_t-channel_4f_leptonDecays_13TeV-amcatnlo-pythia8_TuneCUETP8M1	70.3144
ST_t-channel_antitop_4f_leptonDecays_13TeV-powheg-pythia8_TuneCUETP8M1	26.2278
ST_s-channel_4f_leptonDecays_13TeV-amcatnlo-pythia8_TuneCUETP8M1	3.68064
WWTo2L2Nu_13TeV-powheg	10.481

Table 6.3: List of background samples used in this analysis (CMSSW 80X). In the first section of the table are listed the samples of the processes for which we use the simulation to extract the final yields and shapes, in the second section the samples of the processes we will estimate from data. The MC simulation is used to design the data driven methods and derive the associated systematics.

Sample	σ [pb]
ttWJets_13TeV_madgraphMLM	0.6105
ttZJets_13TeV_madgraphMLM	0.5297/0.692

Table 6.4: Leading-order $t\bar{t}W$ and $t\bar{t}Z$ samples used in the signal BDT training.

Same-sign dilepton (==2 muons)
HLT_Mu17_TrkIsoVVL_Mu8_TrkIsoVVL_DZ_v*
HLT_Mu17_TrkIsoVVL_TkMu8_TrkIsoVVL_DZ_v*
HLT_IsoMu22_v*
HLT_IsoTkMu22_v*
HLT_IsoMu22_eta2p1_v*
HLT_IsoTkMu22_eta2p1_v*
HLT_IsoMu24_v*
HLT_IsoTkMu24_v*
Same-sign dilepton (==2 electrons)
HLT_Ele23_Ele12_CaloIdL_TrackIdL_IsoVL_DZ_v*
HLT_Ele27_eta2p1_WP Loose_Gsf_v*
HLT_Ele27_WPTight_Gsf_v*
HLT_Ele25_eta2p1_WPTight_Gsf_v*
Same-sign dilepton (==1 muon, ==1 electron)
HLT_Mu23_TrkIsoVVL_Ele8_CaloIdL_TrackIdL_IsoVL_v*
HLT_Mu8_TrkIsoVVL_Ele23_CaloIdL_TrackIdL_IsoVL_v*
HLT_Mu23_TrkIsoVVL_Ele8_CaloIdL_TrackIdL_IsoVL_DZ_v*
HLT_Mu8_TrkIsoVVL_Ele23_CaloIdL_TrackIdL_IsoVL_DZ_v*
HLT_IsoMu22_v*
HLT_IsoTkMu22_v*
HLT_IsoMu22_eta2p1_v*
HLT_IsoTkMu22_eta2p1_v*
HLT_IsoMu24_v*
HLT_IsoTkMu24_v*
HLT_Ele27_WPTight_Gsf_v*
HLT_Ele25_eta2p1_WPTight_Gsf_v*
HLT_Ele27_eta2p1_WP Loose_Gsf_v*
Three lepton and Four lepton
HLT_DiMu9_Ele9_CaloIdL_TrackIdL_v*
HLT_Mu8_DiEle12_CaloIdL_TrackIdL_v*
HLT_TripleMu_12_10_5_v*
HLT_Ele16_Ele12_Ele8_CaloIdL_TrackIdL_v*
HLT_Mu23_TrkIsoVVL_Ele8_CaloIdL_TrackIdL_IsoVL_v*
HLT_Mu23_TrkIsoVVL_Ele8_CaloIdL_TrackIdL_IsoVL_DZ_v*
HLT_Mu8_TrkIsoVVL_Ele23_CaloIdL_TrackIdL_IsoVL_v*
HLT_Mu8_TrkIsoVVL_Ele23_CaloIdL_TrackIdL_IsoVL_DZ_v*
HLT_Ele23_Ele12_CaloIdL_TrackIdL_IsoVL_DZ_v*
HLT_Mu17_TrkIsoVVL_Mu8_TrkIsoVVL_DZ_v*
HLT_Mu17_TrkIsoVVL_TkMu8_TrkIsoVVL_DZ_v*
HLT_IsoMu22_v*
HLT_IsoTkMu22_v*
HLT_IsoMu22_eta2p1_v*
HLT_IsoTkMu22_eta2p1_v*
HLT_IsoMu24_v*
HLT_IsoTkMu24_v*
HLT_Ele27_WPTight_Gsf_v*
HLT_Ele25_eta2p1_WPTight_Gsf_v*
HLT_Ele27_eta2p1_WP Loose_Gsf_v*

Table 6.5: Table of high-level triggers that we consider in the analysis.

Category	Scale Factor
ee	1.01 ± 0.02
e μ	1.01 ± 0.01
$\mu\mu$	1.00 ± 0.01
3l	1.00 ± 0.03

Table 6.6: Trigger efficiency scale factors and associated uncertainties, shown here rounded to the nearest percent.

2226 6.5 Object Identification

2227 In this section, the specific definitions of the physical objects in terms of the numerical
 2228 values assigned to the reconstruction parameters are presented; thus, the provided
 2229 details summarize and complement the descriptions presented in previous chapters.
 2230 The object reconstruction and selection strategy used in this thesis is inherited from
 2231 the analyses in references [135, 140], thus, the information provided in this section is
 2232 extracted from those documents unless other references are stated.

2233 6.5.1 Jets and b -jet tagging.

2234 In this analysis, jets are reconstructed by clustering PF candidates using the anti- k_t
 2235 algorithm with parameter distance $\Delta R = 0.4$; those charged hadrons that are not
 2236 consistent with the selected primary vertex are discarded from the clustering. The
 2237 jet energy is then corrected for the varying response of the detector as a function
 2238 of transverse momentum p_T and pseudorapidity η . Jets are selected for use in the
 2239 analysis only if they have $p_T > 25$ GeV and are separated from any selected leptons
 2240 by $\Delta R > 0.4$.

2241 Jets coming from the primary vertex and jets coming from pile-up vertices are
 2242 distinguished using a MVA discriminator based on the differences in the jet shapes,
 2243 in the relative multiplicity of charged and neutral components, and in the different
 2244 fraction of transverse momentum which is carried by the hardest components. Jet

2245 tracks are also required to be compatible with the primary vertex.

2246 Jets originated from the hadronization of a b quark are selected using a MVA
 2247 likelihood discriminant which uses track-based lifetime information and reconstructed
 2248 secondary vertices (CSV algorithm). Only jets within the CMS tracker acceptance
 2249 ($\eta < 2.4$) are identified with this tool. Data samples are used to measure the efficiency
 2250 of the b -jet tagging and the probability to misidentify jets from light quarks or gluons;
 2251 in both cases the measurements are parametrized as a function of the jet p_T and η
 2252 and later used to correct differences between the data and MC simulation in the b
 2253 tagging performance, by applying per-jet weights to the simulation, dependent on
 2254 the jet p_T , η , b tagging discriminator, and flavor (from simulation truth) [138]. The
 2255 per-event weight is taken as the product of the per-jet weights, including those of the
 2256 jets associated to the leptons. The weights are derived on $t\bar{t}$ and Z+jets events.

2257 Two working points are defined, based on the CSV algorithm output: *loose*' work-
 2258 ing point (CSV>0.46) with a b signal tagging efficiency of about 83% and a mistagging
 2259 rate of about 8%; and *medium* working point (CSV>0.80) with b -tagging efficiency of
 2260 about 69% and mistagging rate of order 1% [139]. Tagging of jets from charm quarks
 2261 have efficiencies of about 40% and 18% for loose and medium working points re-
 2262 spectively. Separate scale factors are applied to jets originating from bottom/charm
 2263 quarks and from light quarks in simulated events to match the tagging efficiencies
 2264 measured in the data.

2265 6.5.2 Missing Energy MET.

2266 As stated in section 4.4.1.1, the MET vector is calculated as the negative of the vector
 2267 sum of transverse momenta of all PF candidates in the event and its magnitude is
 2268 referred to as E_T^{miss} . Due to pile-up interactions, the performance in determining

2269 MET is degraded; in order to correct for that, the energy from the selected jets and
 2270 leptons that compose the event is assigned to the variable H_T^{miss} . It is calculated in
 2271 the same way as E_T^{miss} and although it has worse resolution than E_T^{miss} , it is more
 2272 robust in the sense that it does not rely on the soft part of the event. The event
 2273 selection uses a linear discriminator based on the two variables given by

$$E_T^{miss} LD = 0.00397 * E_T^{miss} + 0.00265 * H_T^{miss} \quad (6.1)$$

2274 taking advantage of the fact that the correlation between E_T^{miss} and H_T^{miss} is less
 2275 for events with instrumental missing energy than for events with real missing energy.
 2276 The working point $E_T^{miss} LD > 0.2$ was chosen to ensure a good signal efficiency while
 2277 keeping a good background rejection.

2278 6.5.3 Lepton reconstruction and identification

2279 Two types of leptons are defined in this analysis: *signal leptons* are those coming from
 2280 W, Z and τ decays which usually are isolated from other particles; *background leptons*
 2281 are defined as leptons produced in b -jet hadron decays, light-jets misidentification,
 2282 and photon conversions.

2283 The process of reconstruction and identification of electron and muon candidates
 2284 was described in chapter4, hence, the identification variables used in order to retain
 2285 the highest possible efficiency for signal leptons while maximizing the rejection of
 2286 background leptons are listed and described in the following sections ².

2287 The identification variables include not only observables related directly to the re-
 2288 constructed leptons themselves, but also to the clustered energy deposits and charged
 2289 particles in a cone around the lepton direction (jet-related variables); an initial loose

² the studies performed to optimize the identification are far from the scope of this thesis, therefore, only general descriptions are provided

2290 preselection of leptons candidates is performed and then an MVA discriminator, re-
 2291 fered to as *lepton MVA* discriminator, is used to distinguish signal leptons from
 2292 background leptons.

2293 **Muons.**

2294 The Physics Objects Groups (POG) at CMS, are in charge of studying and defining
 2295 the set of selection criteria applied on the course of reconstruction and identification
 2296 of particles. These selection criteria are implemented in the CMS framework in the
 2297 form of several object identification working points according to the strength of the
 2298 requirements.

2299 The muon candidates are reconstructed by combining information from the tracker
 2300 system and the muon detection system of CMS detector and the POG defined three
 2301 working points for muon identification *MuonID* [141];

- 2302 • *POG Loose Muon ID* is a particle identified as a muon by the PF event re-
 2303 construction and also reconstructed either as a global-muon or as an arbitrated
 2304 tracker-muon. This identification criteria is designed to be highly efficient for
 2305 prompt muons and for muons from heavy and light quark decays; it can be com-
 2306 plemented by applying impact parameter cuts in analyses with prompt muon
 2307 signals.
- 2308 • *POG Medium Muon ID* is a Loose muon with additional track-quality and
 2309 muon-quality (spatial matching between the individual measurements in the
 2310 tracker and the muon system) requirements. This identification criteria is de-
 2311 signed to be highly efficient in the separation of the muons coming from decay
 2312 in flight of heavy quarks and muons coming from B meson decays as well as
 2313 prompt muons. An additional category *MVA Prompt ID* is defined in this iden-

2314 tification criteria directed to discriminated muons from B mesons and prompt
 2315 muons (from W,Z and τ decays). The Medium ID provides the same fake rate as
 2316 the Tight Muon ID but a higher efficiency on prompt and B-decays muons. [142]

- 2317 • *POG Tight Muon ID* is a global muon with additional muon-quality require-
 2318 ments Tight Muon ID selects a subset of the PF muons.

2319 Only muons within the muon system acceptance $|\eta| < 2.4$ and minimum p_T of 5
 2320 GeV are considered.

2321 **Electrons.**

2322 Electrons are reconstructed using information from the tracker and from the electro-
 2323 magnetic calorimeter and identified by an MVA algorithm (*MVA eID* discriminant)
 2324 using the shape of the calorimetric shower variables like the shape in η and ϕ , the clus-
 2325 ter circularity, widths along η and ϕ ; track-cluster matching variables like E_{tot}/p_{in} ,
 2326 E_{Ele}/p_{out} , $\Delta\eta_{in}$, $\Delta\eta_{out}$, $\Delta\phi_{in}$, $1/E - 1/p$; and track quality variables like ξ^2 of the
 2327 GSF tracks, the number of hits used by the GSF filter [143].

2328 A loose selection based on η -dependent cuts on this discriminant is used to prese-
 2329 lect electron candidates, the full shape of the discriminant is used in the lepton MVA
 2330 selection to separate signal leptons from background leptons (described in section
 2331 6.5.3).

2332 In order to reject electrons from photon conversions, electron candidates with
 2333 missing hits in the pixel tracker layers or matched to a conversion secondary vertex
 2334 are discarded. Electrons are selected for the analysis if they have $p_T > 7$ GeV and
 2335 are located within the tracker system acceptance region ($|\eta| < 2.5$).

2336 **Lepton vertexing and pile-up rejection.**

2337 The impact parameter in the transverse plane d_0 , impact parameter along the z
 2338 axis d_z , and the impact parameter significance in the detector space SIP_{3D} , are
 2339 considered to perform the identification and rejection of pile-up, misreconstructed
 2340 tracks, and background leptons from b-hadron decays; pile-up and misreconstructed
 2341 track mitigation is achieved by imposing loose cuts on the impact parameter variables.
 2342 The full shape of the those variables is used in a lepton MVA classifier to achieve the
 2343 best separation between the signal and the background leptons.

2344 **Lepton isolation.**

2345 PF is able to recognize leptons from two different sources: on one side, leptons from
 2346 the decays of heavy particles, such as W and Z bosons, which are normally isolated
 2347 in space from the hadronic activity in the event; on the other side, leptons from the
 2348 decays of hadrons and jets misidentified as leptons, which are not isolated as the
 2349 former. For highly boosted systems, like the lepton and the b -jet generated in the
 2350 semileptonic decay of a boosted top, the decay products tend to be more closer and
 2351 sometimes they even overlap; thus, the PF standard definition of isolation in terms of
 2352 the separation between the lepton candidates and other PF objects in the η - ϕ plane,

$$\Delta R = \sqrt{(\eta^l - \eta^i)^2 + (\phi^l - \phi^i)^2} < 0.3 \quad (6.2)$$

2353 which considers all the neutral, charged hadrons and photons in a cone around the
 2354 leptons, is refocused to the local isolation of the leptons through the mini-isolation
 2355 I_{mini} [144] defined as the sum of particle flow candidates p_T within a cone around

2356 the lepton, corrected for the effects of pileup and divided by the lepton p_T

$$I_{mini} = \frac{\sum_R p_T(h^\pm) - \max \left(0, \sum_R p_T(h^0) + p_T(\gamma) - \rho \mathcal{A} \left(\frac{R}{0.3} \right)^2 \right)}{p_T(l)} \quad (6.3)$$

2357 where ρ is the pileup energy density, h^\pm, h^0, γ, l , represent the charged hadron, neutral
 2358 hadrons, photons, and the lepton, respectively. The radius R of the cone depends on
 2359 the p_T of the lepton according to

$$R = \frac{10\text{GeV}}{\min(\max(p_T(l), 50\text{GeV}), 200\text{GeV})}, \quad (6.4)$$

2360 The p_T dependence of the cone size allows for greater signal efficiency. Setting a
 2361 cut on I_{mini} below a given threshold ensures that the lepton is locally isolated, even
 2362 in boosted systems. The effect of pileup is mitigated using the so-called effective area
 2363 correction \mathcal{A} listed in Table 6.7.

$ \eta $ range	$\mathcal{A}(e)$ neutral/charged	$\mathcal{A}(\mu)$ neutral/charged
0.0 - 0.8	0.1607 / 0.0188	0.1322 / 0.0191
0.8 - 1.3	0.1579 / 0.0188	0.1137 / 0.0170
1.3 - 2.0	0.1120 / 0.0135	0.0883 / 0.0146
2.0 - 2.2	0.1228 / 0.0135	0.0865 / 0.0111
2.2 - 2.5	0.2156 / 0.0105	0.1214 / 0.0091

Table 6.7: Effective areas, for electrons and muons used to mitigate the effect of pileup by using the so-called effective area correction.

2364 A loose cut on I_{mini} is applied to pre-select the muon and electron candidates;
 2365 however, the full shape is used in the lepton MVA discriminator when performing the
 2366 signal lepton selection.

2367 **Jet-related variables.**

2368 In order to reject misidentified leptons from b -jets, mostly coming from $t\bar{t}$ +jets,
 2369 Drell-Yan+jets, and W+jets events, the vertexing and isolation described in previous
 2370 sections are complemented with additional variables related to the closest recon-
 2371 structed jet to the lepton, i.e., the PF jets reconstructed³ around the leptons with
 2372 $\Delta R = \sqrt{(\eta^l - \eta^{jet})^2 + (\phi^l - \phi^{jet})^2} < 0.5$. The identification variables used in the lep-
 2373 ton MVA discriminator are the ratio p_T^l/p_T^{jet} , the CSV b-tagging discriminator value
 2374 of the jet, the number of charged tracks of the jet, and the relative p_T given by

$$p_T^{rel} = \frac{(\vec{p}_{jet} - \vec{p}_l) \cdot \vec{p}_l}{\|\vec{p}_{jet} - \vec{p}_l\|}. \quad (6.5)$$

2375 **LeptonMVA discriminator.**

2376 Electrons and muons passing the basic selection process described above are referred
 2377 to as *loose leptons*. Additional discrimination between signal leptons and background
 2378 leptons is crucial considering that the rate of $t\bar{t}$ production is much larger than the
 2379 signal, hence, an overwhelming background from $t\bar{t}$ production. To maximally ex-
 2380 ploit the available information in each event to that end, the dedicated lepton MVA
 2381 discriminator, based on a boosted decision tree (BDT) algorithm, has been built so
 2382 that all the identification variables can be used together.

2383 The lepton MVA discriminator training is performed using simulated signal Loose
 2384 leptons from the $t\bar{t}H$ MC sample and fake leptons from the $t\bar{t}$ +jets MC sample,
 2385 separately for muons and electrons. The input variables used include vertexing, iso-
 2386 lation and jet-related variables, the p_T and η of the lepton, the electron MVA eID
 2387 discriminator and the muon segment-compatibility variables. An additional require-
 2388 ment known as *tight-charge* requirement, is imposed by comparing two independent

³ charged hadrons from PU vertices are not removed prior to the jet clustering.

measurement of the charge, one from the ECAL supercluster and the other from the tracker; thus, the consistency in the measurements of the electron charge is ensured so that events with a wrong electron charge assignment are rejected; this variable is particularly used in the 2lss channel to suppress opposite-sign events for which the charge of one of the leptons has been mismeasured. The tight-charge requirement for muons is represented by the requirement of a consistently well measured track transverse momentum given by $\Delta p_T/p_T < 0.2$. Leptons are selected for the final analysis if they pass a given threshold of the BDT output, and are referred to as *tight leptons* in the following.

The validation of the lepton MVA algorithm and the lepton identification variables is performed using data in various control regions; the details about that validation are not discussed here but can be found in Reference [140].

Selection definitions

Electron and muon object identification is defined in three different sets of selections criteria; the *Loose*, *Fakeable Object*, and *Tight* selection. These three levels of selection are designed to serve for event level vetoes, the fake rate estimation application region, and the final signal selection, respectively. The p_T of fakeable objects is defined as $0.85 \times p_T(\text{jet})$, where the jet is the one associated to the lepton object. This mitigates the dependence of the fake rate on the momentum of the fakeable object and thereby improves the precision of the method.

Tables 6.8 and 6.9 list the full criteria for the different selections of muons and electrons.

In addition to the previously defined requirements for jets, they are required to be separated from any lepton candidates passing the fakeable object selections by $\Delta R > 0.4$.

Cut	Loose	Fakeable object	Tight
$ \eta < 2.4$	✓	✓	✓
p_T	$> 5\text{GeV}$	$> 15\text{GeV}$	$> 15\text{GeV}$
$ d_{xy} < 0.05$ (cm)	✓	✓	✓
$ d_z < 0.1$ (cm)	✓	✓	✓
$\text{SIP}_{3D} < 8$	✓	✓	✓
$I_{\text{mini}} < 0.4$	✓	✓	✓
is Loose Muon	✓	✓	✓
jet CSV	—	< 0.8484	< 0.8484
is Medium Muon	—	—	✓
tight-charge	—	—	✓
lepMVA > 0.90	—	—	✓

Table 6.8: Requirements on each of the three muon selections. In the cases where the cut values change between the selections, those values are listed in the table. Otherwise, whether the cut is applied is indicated.

Cut	Loose	Fakeable Object	Tight
$ \eta < 2.5$	✓	✓	✓
p_T	$> 7\text{GeV}$	$> 15\text{GeV}$	$> 15\text{GeV}$
$ d_{xy} < 0.05$ (cm)	✓	✓	✓
$ d_z < 0.1$ (cm)	✓	✓	✓
$\text{SIP}_{3D} < 8$	✓	✓	✓
$I_{\text{mini}} < 0.4$	✓	✓	✓
MVA eID $> (0.0, 0.0, 0.7)$	✓	✓	✓
$\sigma_{in\eta} < (0.011, 0.011, 0.030)$	—	✓	✓
H/E $< (0.10, 0.10, 0.07)$	—	✓	✓
$\Delta\eta_{in} < (0.01, 0.01, 0.008)$	—	✓	✓
$\Delta\phi_{in} < (0.04, 0.04, 0.07)$	—	✓	✓
$-0.05 < 1/E - 1/p < (0.010, 0.010, 0.005)$	—	✓	✓
p_T^{ratio}	—	$> 0.5^\dagger / -$	—
jet CSV	—	$< 0.3^\dagger / < 0.8484$	< 0.8484
tight-charge	—	—	✓
conversion rejection	—	—	✓
Number of missing hits	< 2	$= 0$	$= 0$
lepton MVA > 0.90	—	—	✓

Table 6.9: Criteria for each of the three electron selections. In cases where the cut values change between selections, those values are listed in the table. Otherwise, whether the cut is applied is indicated. In some cases, the cut values change for different η ranges. These ranges are $0 < |\eta| < 0.8$, $0.8 < |\eta| < 1.479$, and $1.479 < |\eta| < 2.5$ and the respective cut values are given in the form (value₁, value₂, value₃). For the two p_T^{ratio} and CSV rows, the cuts marked with a \dagger are applied to leptons that fail the lepton MVA cut, while the loose cut value is applied to those that pass the lepton MVA cut.

2414 6.5.4 Lepton selection efficiency

2415 Efficiencies of reconstruction and selecting loose leptons are measured both for muons
 2416 and electrons using a tag and probe method on both data and MC, using $Z \rightarrow \ell^+ \ell^-$
 2417 [145]. The scale factors are derived from the ratio of efficiencies $\varepsilon_i(p_T, \eta)$ measured
 2418 for a given lepton in data/MC, according to

$$\rho(p_T, \eta) = \frac{\varepsilon_{\text{data}}(p_T, \eta)}{\varepsilon_{\text{MC}}(p_T, \eta)}. \quad (6.6)$$

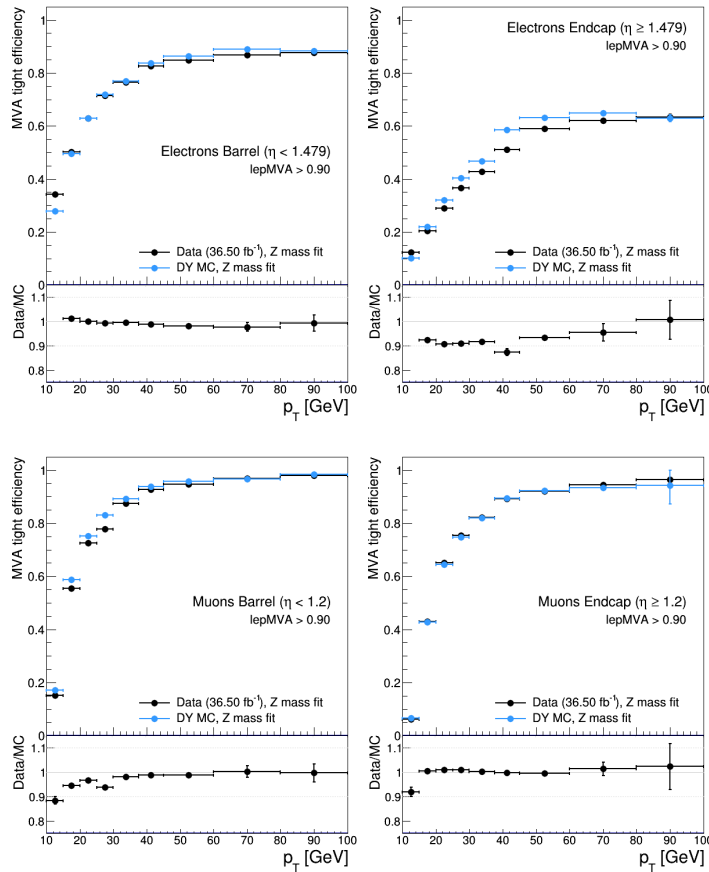


Figure 6.3: Tight vs loose selection efficiencies for electrons (top), and muons (bottom), for the 2lss definition, i.e., including the tight-charge requirement.

2419 The scale factor for each event is used to correct the weight of the event in the

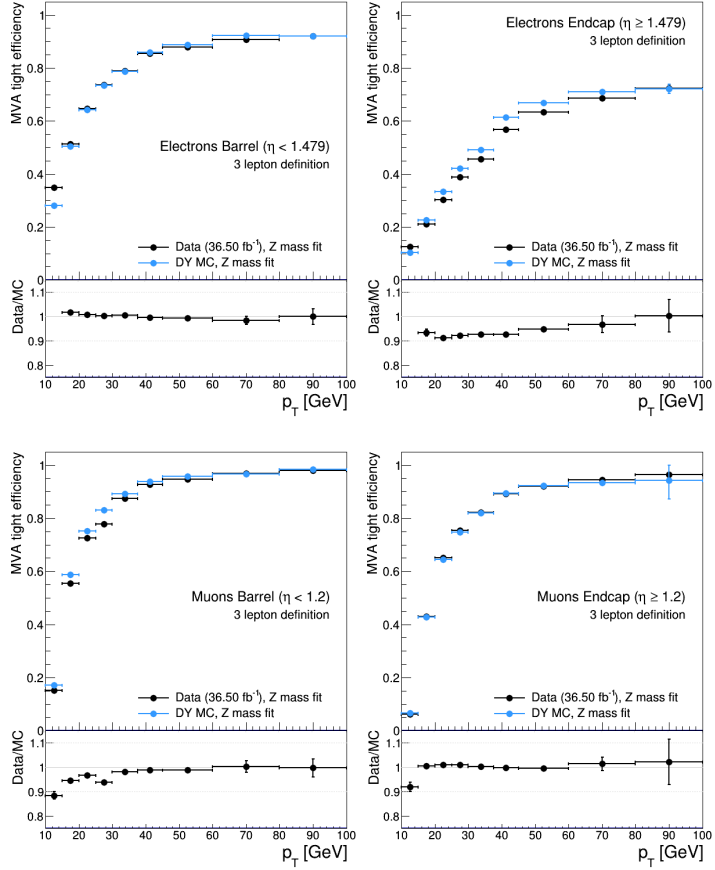


Figure 6.4: Tight vs loose selection efficiencies for electrons (top), and muons (bottom), for the 3l channel not including the tight-charge requirement.

2420 full sample; therefore, the full simulation correction is given by the product of all
 2421 the individual scale factors. The scale factors used in this thesis are inherited from
 2422 the reference [140] which in turns inherited them from leptonic SUSY analyses using
 2423 equivalent lepton selections.

2424 The efficiency of applying the tight selection as defined in Tables 6.8 and 6.9, on the
 2425 loose leptons are determined by using a tag and probe method on a sample of Drell-
 2426 Yan enriched events. Figures 6.3 and 6.4 show the efficiencies for the 2lss channel and
 2427 3l channel respectively. Efficiencies in the 2lss channel have been produced including
 2428 the tight-charge requirement, while for the 3l channel it is not included. Number

2429 of passed and failed probes are determined from a fit to the invariant mass of the
 2430 dilepton system.

2431 Simulation is corrected using these scale factors; note that they depends on η and
 2432 p_T .

2433 **6.6 Event selection**

2434 .

2435 .

2436 .

2437 .

2438 .

2439 .

2440 .

2441 .

2442 .

2443 . . .

2444 The analysis is designed to efficiently identify and select prompt leptons from
 2445 on-shell W and

2446 Z boson decays and to reject non-prompt leptons from b quark decays and spurious
 2447 lepton

2448 signatures from hadronic jets. Events are then selected in the various lepton
 2449 channels, and are

2450 required to contain hadronic jets, some of which must be consistent with b quark
 2451 hadronization. Finally, the signal yield is extracted by simultaneously fitting the
 2452 output of two dedicated

2453 multivariate discriminants (trained to separate the tHq signal from the two dom-
 2454 inant backgrounds) in all categories

2455 . Multivariate techniques are used to discriminate the signal from the dominant
 2456 backgrounds. The analysis yields a 95% confidence level (C.L.) upper limit on the
 2457 combined $tH + ttH$ production cross section times branching ratio of 0.64 pb, with
 2458 an expected limit of 0.32 pb, for a scenario with $kt = \sqrt{1.0}$ and $kV = 1.0$. Values
 2459 of kt outside the range of $\sqrt{1.25}$ to $\sqrt{1.60}$ are excluded at 95% C.L., assuming kV
 2460 $= 1.0$.

2461 Dont forget to mention previous constrains to ct check reference ?? and references
 2462 <https://link.springer.com/content/pdf/10.1007%2FJHEP01%282013%29088.pdf> (para-
 2463 graph after eq 2)

2464 We selects events with three leptons and a b -jet tagged jet in the final state. The tHq
 2465 signal contribution is then determined in a fit of the observed data to two multivariate
 2466 classifier outputs, each trained to discriminate against one of the two dominant back-
 2467 grounds of events with non-prompt leptons from $t\bar{t}$ and of associated production of $t\bar{t}$
 2468 and vector bosons ($t\bar{t}W$, $t\bar{t}Z$). The fit result is then used to set an upper limit on the
 2469 combined $t\bar{t}H$, tHq and tHW production cross section, as a function of the relative
 2470 coupling strengths of Higgs and top quark and Higgs and W boson, respectively.

2471 **6.7 Background predictions**

2472 The modeling of reducible and irreducible backgrounds in this analysis uses the exact
 2473 methods, analysis code, and ROOT trees used for the $t\bar{t}H$ multilepton analysis. We
 2474 give a brief description of the methods and refer to the documentation of that analysis
 2475 in Refs. [135, 140] for any details.

2476 The backgrounds in three-lepton final states can be split in two broad categories:

irreducible backgrounds with genuine prompt leptons (i.e. from on-shell W and Z boson decays); and reducible backgrounds where at least one of the leptons is “non-prompt”, i.e. produced within a hadronic jet, either a genuine lepton from heavy flavor decays, or simply mis-reconstructed jets.

Irreducible backgrounds can be reliably estimated directly from Monte-Carlo simulated events, using higher-order cross sections or data control regions for the overall normalization. This is done in this analysis for all backgrounds involving prompt leptons: $t\bar{t}W$, $t\bar{t}Z$, $t\bar{t}H$, WZ , ZZ , $W^\pm W^\pm qq$, $t\bar{t}t\bar{t}$, tZq , tZW , WWW , WWZ , WZZ , ZZZ .

Reducible backgrounds, on the other hand, are not well predicted by simulation, and are estimated using data-driven methods. In the case of non-prompt leptons, a fake rate method is used,

Additional identification criteria are applied for electrons with p_T greater than 30 GeV to mimic the identification applied at trigger level in order to ensure consistency between the measurement region and application region of the fake-rate.

where the contribution to the final selection is estimated by extrapolating from a sideband (or “application region”) with a looser lepton definition (the fakeable object definitions in Tabs. 6.8 and 6.9) to the signal selection. The tight-to-loose ratios (or “fake rates”) are measured in several background dominated data events with dedicated triggers, subtracting the residual prompt lepton contribution using MC. Non-prompt leptons in our signal regions are predominantly produced in $t\bar{t}$ events, with a much smaller contribution, from Drell–Yan production. The systematic uncertainty on the normalization of the non-prompt background estimation is on the order of 50%, and thereby one of the dominant limitations on the performance of multilepton analyses in general and this analysis in particular. It consists of several individual sources, such as the result of closure tests of the method using simulated

2503 events, limited statistics in the data control regions due to necessary prescaling of
 2504 lepton triggers, and the uncertainty in the subtraction of residual prompt leptons
 2505 from the control region.

2506 The fake background where the leptons pass the looser selection are weighted
 2507 according to how many of them fail the tight criteria. Events with a single failing
 2508 lepton are weighted with the factor $f/(1-f)$ for the estimate to the tight selection
 2509 region, where f is the fake rate. Events with two failing leptons are given the negative
 2510 weight $-f_i f_j / (1-f_i)(1-f_j)$, and for three leptons the weight is positive and equal
 2511 to the product of $f/(1-f)$ factor evaluated for each failing lepton.

2512 Figures 6.5 show the distributions of some relevant kinematic variables, normalized
 2513 to the cross section of the respective processes and to the integrated luminosity.

2514 6.8 Signal discrimination

2515 The tHq signal is separated from the main backgrounds using a boosted decision
 2516 tree (BDT) classifier, trained on simulated signal and background events. A set
 2517 of discriminating variables are given as input to the BDT which produces a output
 2518 distribution maximizing the discrimination power. Table 6.10 lists the input variables
 2519 used while Figures 6.6 show their distributions for the relevant signal and background
 2520 samples, for the three lepton channel. Two BDT classifiers are trained for the two
 2521 main backgrounds expected in the analysis: events with prompt leptons from $t\bar{t}W$ and
 2522 $t\bar{t}Z$ (also referred to as $t\bar{t}V$), and events with non-prompt leptons from $t\bar{t}$. The datasets
 2523 used in the training are the tHq signal (see Tab. 6.1), and LO MADGRAPH samples
 2524 of $t\bar{t}W$ and $t\bar{t}Z$, in an admixture proportional to their respective cross sections (see
 2525 Tab. 6.4).

2526 The MVA analysis consist of two stages: first a “training” where the MVA method

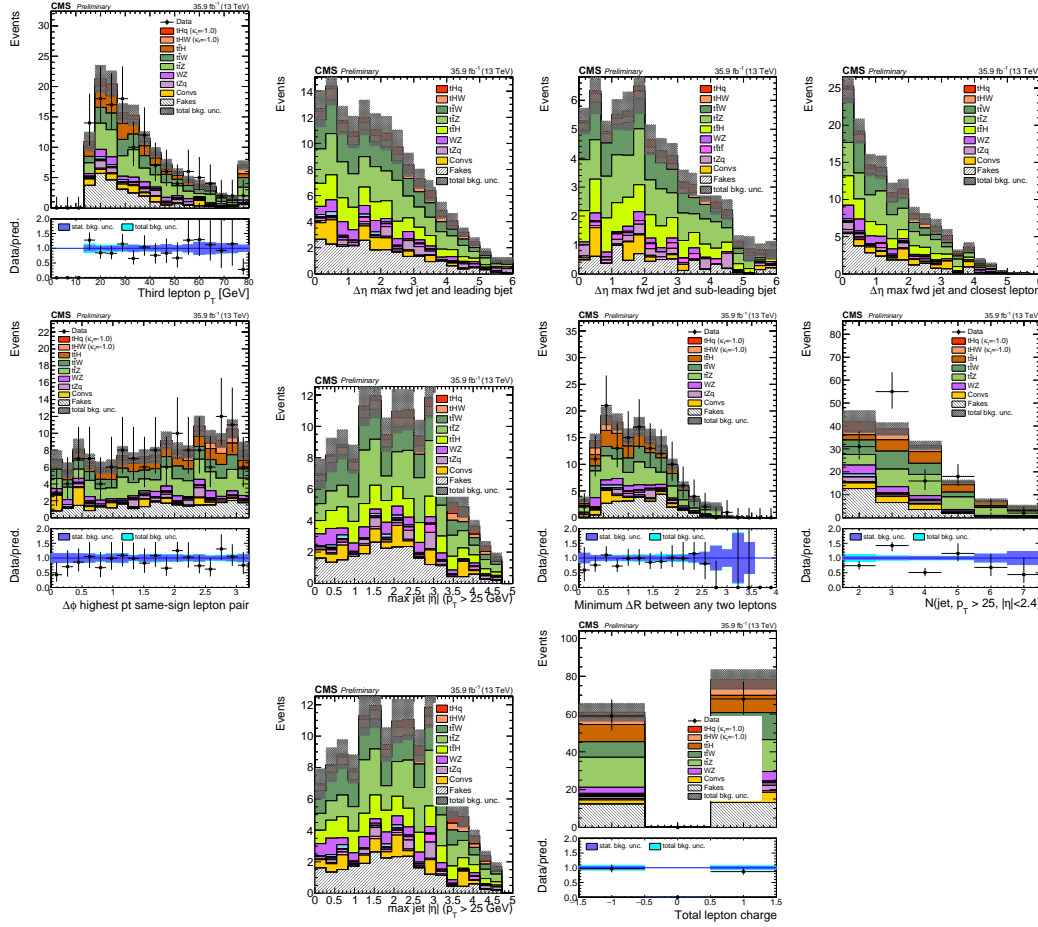


Figure 6.5: Distributions of input variables to the BDT for signal discrimination, three lepton channel, normalized to their cross section and to 35.9 fb^{-1} .

is trained to discriminate between simulated signal and background events, then a “test” stage where the trained algorithm is used to classify different events from the samples. The sample is obtained from a pre-selection (see Tab. ?? with pre-selection cuts). Figures 6.7 show the input variables distributions as seen by the MVA algorithm. Note that in contrast to the distributions in Fig. 6.6 only the main backgrounds ($t\bar{t}$ from simulation, $t\bar{t}V$) are included.

Note that splitting the training in two groups reveals that some variables show opposite behavior for the two background sources; potentially screening the discrimination power if they were to be used in a single discriminant. For some other variables

Variable name	Description
nJet25	Number of jets with $p_T > 25$ GeV, $ \eta < 2.4$
MaxEtaJet25	Maximum $ \eta $ of any (non-CSV-loose) jet with $p_T > 25$ GeV
totCharge	Sum of lepton charges
nJetEta1	Number of jets with $ \eta > 1.0$, non-CSV-loose
detaFwdJetBJet	$\Delta\eta$ between forward light jet and hardest CSV loose jet
detaFwdJet2BJet	$\Delta\eta$ between forward light jet and second hardest CSV loose jet (defaults to -1 in events with only one CSV loose jet)
detaFwdJetClosestLep	$\Delta\eta$ between forward light jet and closest lepton
dphiHighestPtSSPair	$\Delta\phi$ of highest p_T same-sign lepton pair
minDRll	minimum ΔR between any two leptons
Lep3Pt/Lep2Pt	p_T of the 3 rd lepton (2 nd for ss2l)

Table 6.10: MVA input discriminating variables

2536 the distributions are similar in both background cases.

2537 From table 6.10, it is clear that the input variables are correlated to some extend.
 2538 These correlations play an important role for some MVA methods like the Fisher
 2539 discriminant method in which the first step consist of performing a linear transfor-
 2540 mation to an phase space where the correlations between variables are removed. In
 2541 case a boosted decision tree (BDT) method however, correlations do not affect the
 2542 performance. Figure 6.9 show the linear correlation coefficients for signal and back-
 2543 ground for the two training cases (the signal values are identical by construction). As
 2544 expected, strong correlations appears for variables related to the forward jet activity.
 2545 Same trend is seen in case of the same sign dilepton channel in Figure ??.

2546 6.8.1 Classifiers response

2547 Several MVA algorithms were evaluated to determine the most appropriate method
 2548 for this analysis. The plots in Fig. 6.10 (top) show the background rejection as a
 2549 function of the signal efficiency for $t\bar{t}$ and $t\bar{t}V$ trainings (ROC curves) for the different

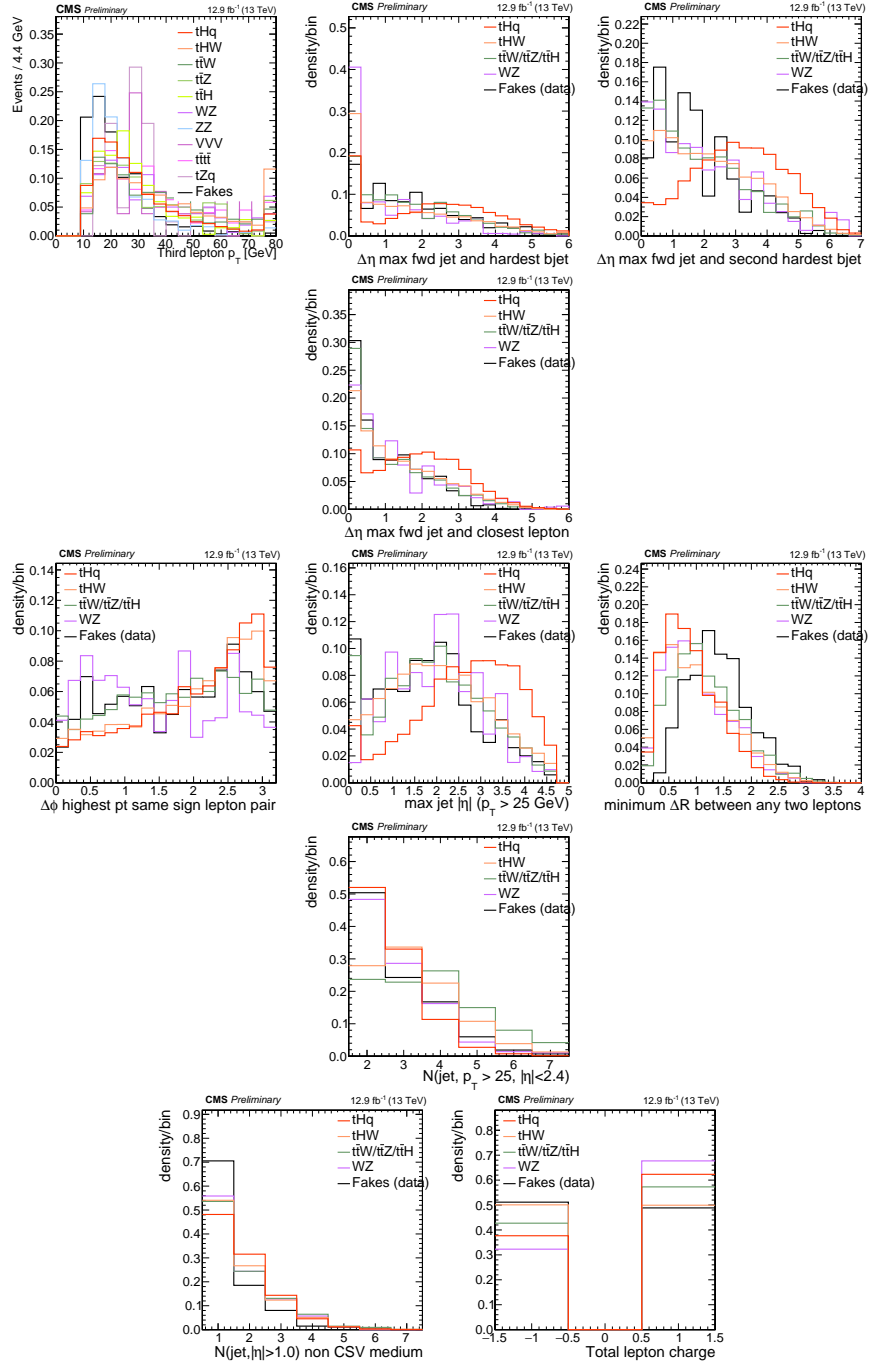


Figure 6.6: Distributions of input variables to the BDT for signal discrimination, three lepton channel.

2550 algorithms that were evaluated.

2551 In both cases the gradient boosted decision tree (“BDTA_GRAD”) classifier offers

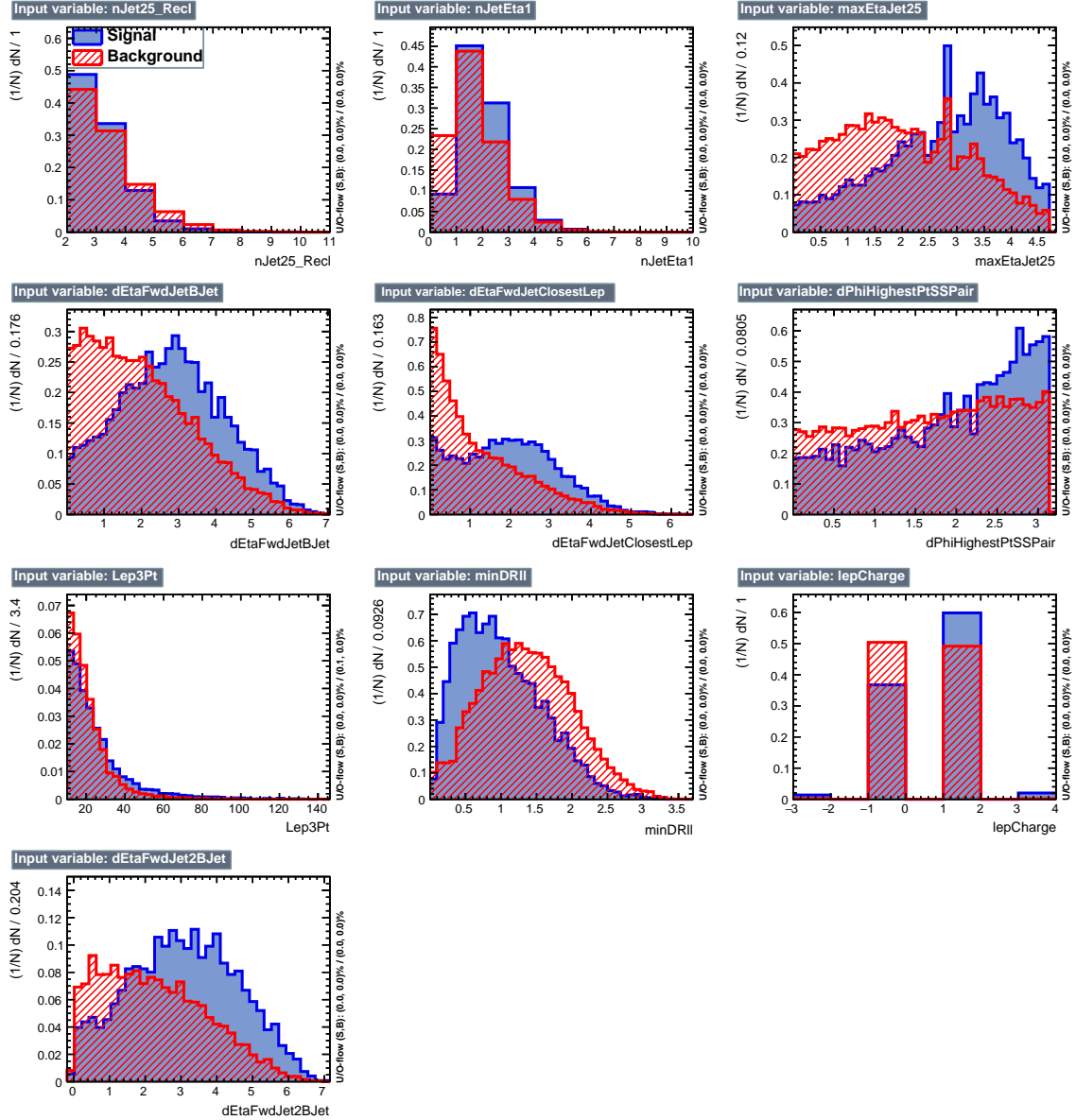


Figure 6.7: BDT inputs as seen by TMVA (signal, in blue, is tHq , background, in red, is $t\bar{t}$) for the three lepton channel, discriminated against $t\bar{t}$ (fakes) background.

the best results, followed by an adaptive BDT classifier (“BDTA”). The BDTA_GRAD classifier output distributions for signal and backgrounds are shown on the bottom of Fig. 6.10. As expected, a good discrimination power is obtained using default discriminator parameter values, with minimal overtraining. TMVA provides a ranking of the input variables by their importance in the classification process, shown in Tab. 6.11.

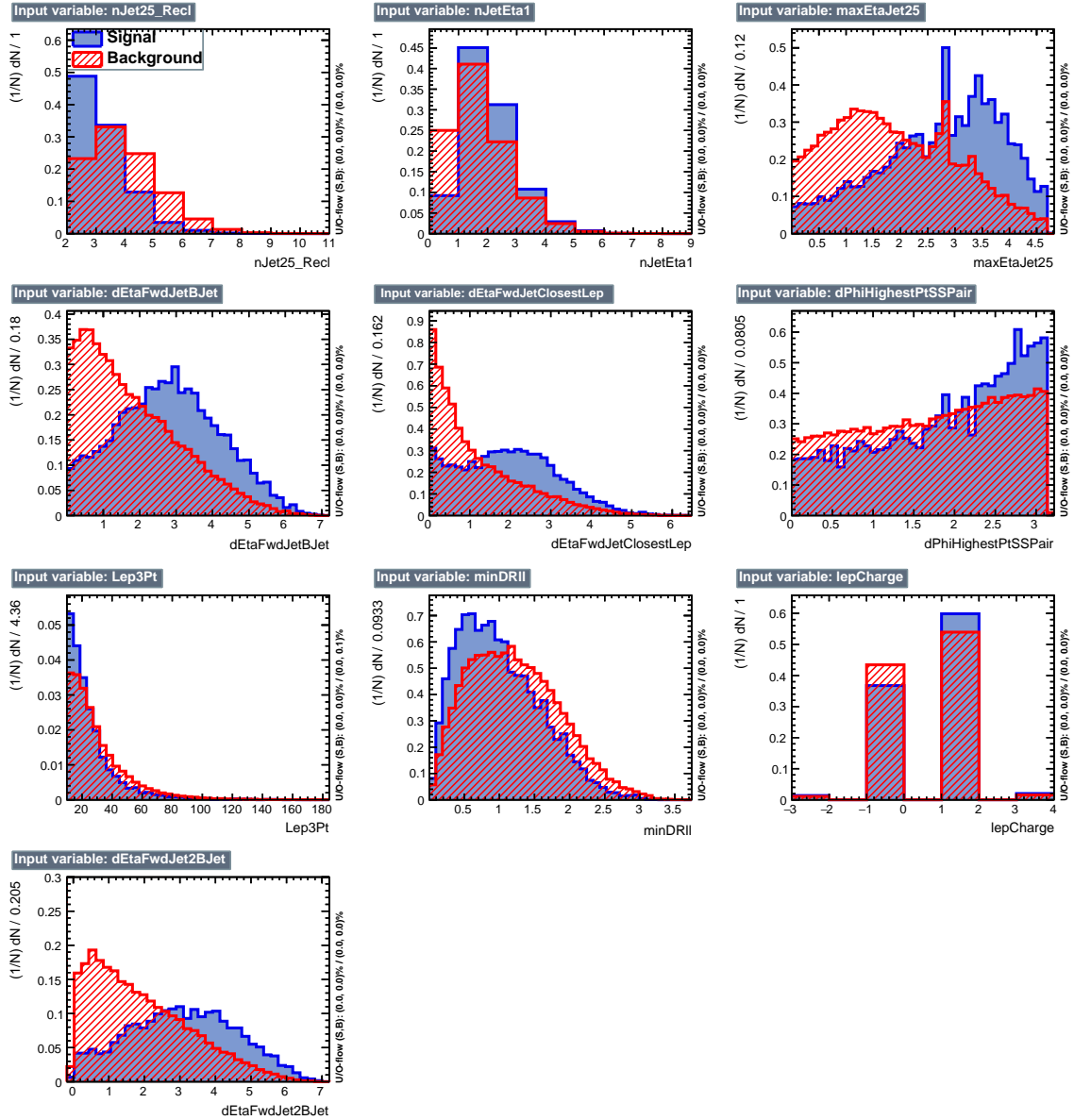


Figure 6.8: BDT inputs as seen by TMVA (signal, in blue, is tHq , background, in red, is $t\bar{t}W+t\bar{t}Z$) for the three lepton channel, discriminated against $t\bar{t}V$ background.

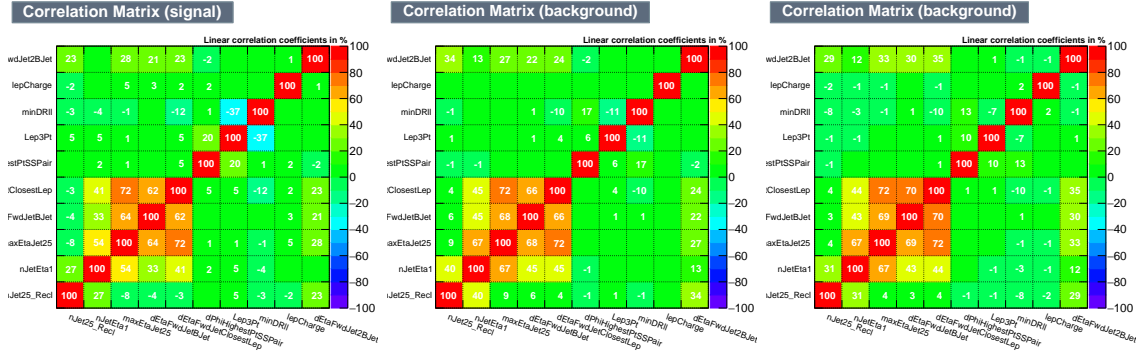


Figure 6.9: Signal (left), $t\bar{t}$ background (middle), and $t\bar{t}V$ background (right.) correlation matrices for the input variables in the TMVA analysis for the three lepton channel.

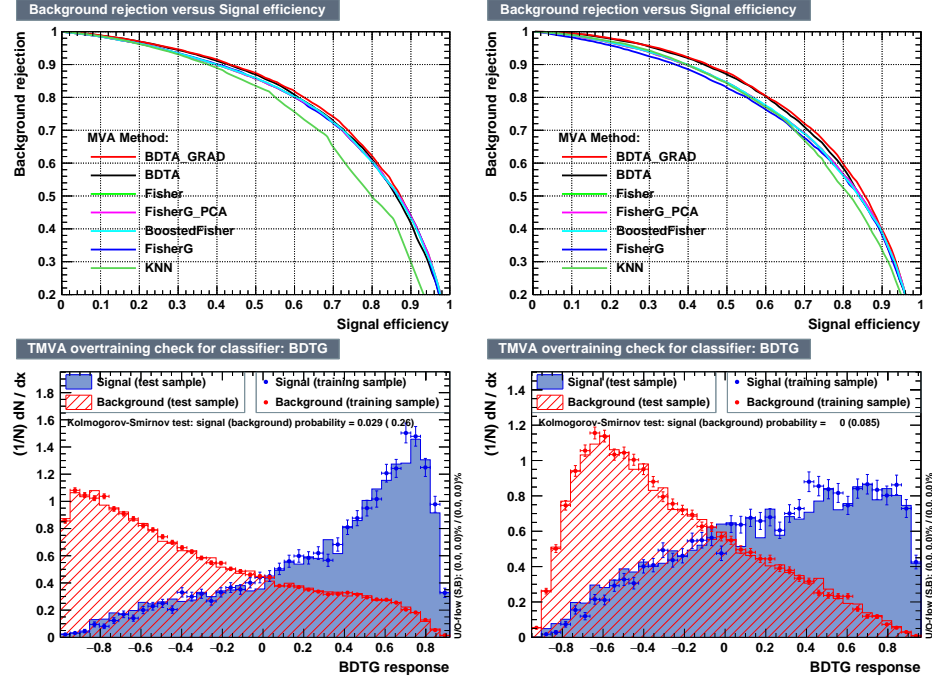


Figure 6.10: Top: background rejection vs signal efficiency (ROC curves) for various MVA classifiers (top) in the three lepton channel against $t\bar{t}V$ (left) and $t\bar{t}$ (right). Bottom: classifier output distributions for the gradient boosted decision trees, for training against $t\bar{t}V$ (left) and against $t\bar{t}$ (right).

2558 6.9 Additional discriminating variables

2559 Two additional discriminating variables were tested considering the fact that the
 2560 forward jet in the background could come from the pileup; since we have a real forward

ttbar training			ttV training		
Rank	Variable	Importance	Variable	Importance	Importance
1	minDRll	1.329e-01	dEtaFwdJetBJet	1.264e-01	
2	dEtaFwdJetClosestLep	1.294e-01	Lep3Pt	1.224e-01	
3	dEtaFwdJetBJet	1.209e-01	maxEtaJet25	1.221e-01	
4	dPhiHighestPtSSPair	1.192e-01	dEtaFwdJet2BJet	1.204e-01	
5	Lep3Pt	1.158e-01	dEtaFwdJetClosestLep	1.177e-01	
6	maxEtaJet25	1.121e-01	minDRll	1.143e-01	
7	dEtaFwdJet2BJet	9.363e-02	dPhiHighestPtSSPair	9.777e-02	
8	nJetEta1	6.730e-02	nJet25_Recl	9.034e-02	
9	nJet25_Recl	6.178e-02	nJetEta1	4.749e-02	
10	lepCharge	4.701e-02	lepCharge	4.116e-02	

Table 6.11: TMVA input variables ranking for BDTA_GRAD method for the trainings in the three lepton channel. For both trainings the rankings show almost the same 5 variables in the first places.

```

TMVA.Types.kBDT
NTrees=800
BoostType=Grad
Shrinkage=0.10
!UseBaggedGrad
nCuts=50
MaxDepth=3
NegWeightTreatment=PairNegWeightsGlobal
CreateMVAPdfs

```

Table 6.12: TMVA configuration used in the BDT training.

2561 jet in the signal, it could give some improvement in the discriminating power. The
 2562 additional variables describe the forward jet momentum (fwdJetPt25) and the forward
 2563 jet identification(fwdJetPUID). Distributions for these variables in the three lepton
 2564 channel are shown in the figure 6.11. The forward jet identification distribution show
 2565 that for both, signal and background, jets are mostly real jets.

2566 The testing was made including in the MVA input one variable at a time, so we
 2567 can evaluate the dicrimination power of each variable, and then both simultaneously.
 2568 fwdJetPUID was ranked in the last place in importance (11) in both training (ttV
 2569 and tt) while fwdJetPt25 was ranked 3 in the ttV training and 7 in the tt training.
 2570 When training using 12 variables, fwdJetPt25 was ranked 5 and 7 in the ttV and tt

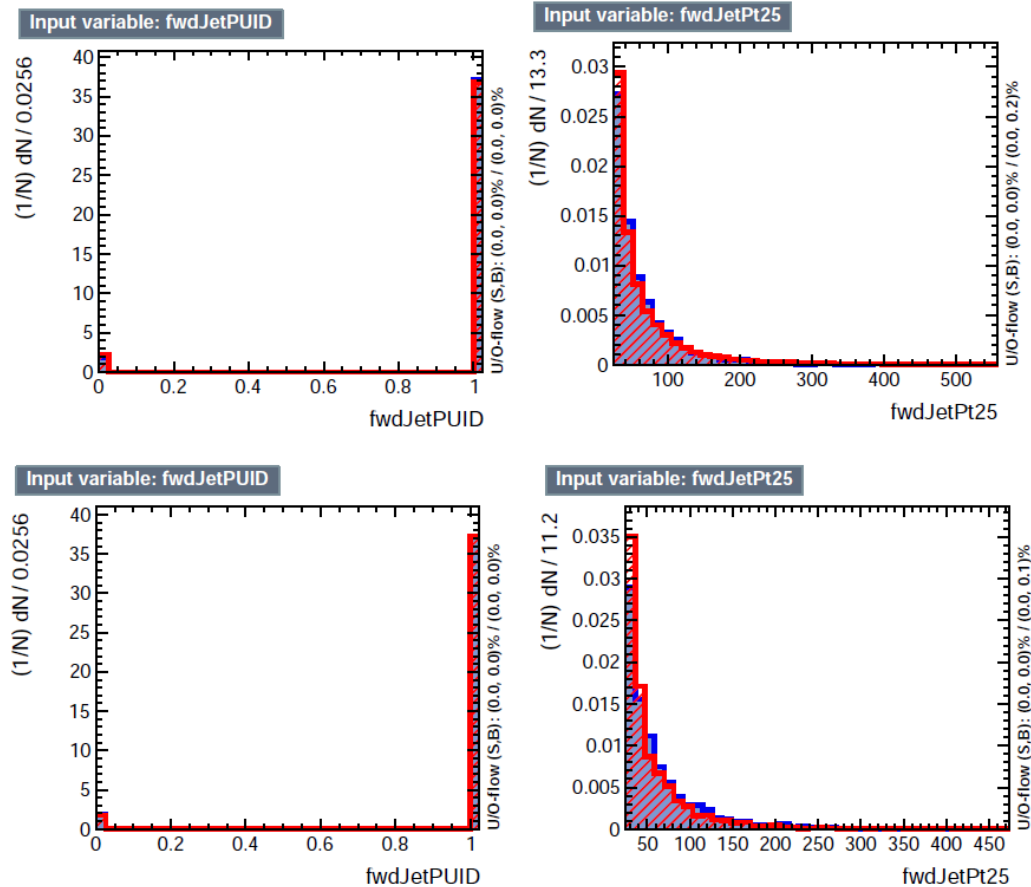


Figure 6.11: Additional discriminating variables distributions for ttv training (Top row) and tt training (bottom row) in the three lepton channel. The origin of the jets in the forward jet identification distribution is tagged as 0 for “pileup jets” while “real jets” are tagged as 1.

2571 trainings respectively, while `fwdJetPUID` was ranked 12 in both cases.

2572 The improvement in the discrimination performance provided by the additional
 2573 variables is about 1%, so it was decided not to include them in the procedure. Table
 2574 6.13 show the ROC-integral for all the testing cases we made.

ROC-integral	
base 10 var ttv	0.848
+ fwdJetPUID ttv	0.849
+ fwdJetPt25 ttv	0.856
12 var ttv	0.856
<hr/>	
base 10 var tt	0.777
+ fwdJetPUID tt	0.777
+ fwdJetPt25 tt	0.787
12 var	0.787

Table 6.13: ROC-integral for all the testing cases we made in the evaluation of the additional variables discriminating power. The improvement in the discrimination performance provided by the additional variables is about 1%

2575 **References**

- 2576 [1] J. Schwinger. "Quantum Electrodynamics. I. A Covariant Formulation". Phys-
2577 ical Review. 74 (10): 1439-61, (1948). <https://doi.org/10.1103/PhysRev.74.1439>
- 2579 [2] R. P. Feynman. "Space-Time Approach to Quantum Electrodynamics". Physical
2580 Review. 76 (6): 769-89, (1949). <https://doi.org/10.1103/PhysRev.76.769>
- 2581 [3] S. Tomonaga. "On a Relativistically Invariant Formulation of the Quantum
2582 Theory of Wave Fields". Progress of Theoretical Physics. 1 (2): 27-42, (1946).
2583 <https://doi.org/10.1143/PTP.1.27>
- 2584 [4] D.J. Griffiths, "Introduction to electrodynamics". 4th ed. Pearson, (2013).
- 2585 [5] F. Mandl, G. Shaw. "Quantum field theory." Chichester, Wiley (2009).
- 2586 [6] F. Halzen, and A.D. Martin, "Quarks and leptons: An introductory course in
2587 modern particle physics". New York: Wiley, (1984) .
- 2588 [7] File: Standard_Model_of_Elementary_Particle_dark.svg. (2017, June 12)
2589 Wikimedia Commons, the free media repository. Retrieved November 27, 2017
2590 from <https://www.collegiate-advanced-electricity.com/single-post/2017/04/10/The-Standard-Model-of-Particle-Physics>.

- 2592 [8] E. Noether, "Invariante Variationsprobleme", Nachrichten von der Gesellschaft
2593 der Wissenschaften zu Göttingen, mathematisch-physikalische Klasse, vol. 1918,
2594 pp. 235-257, (1918).
- 2595 [9] C. Patrignani et al. (Particle Data Group), Chin. Phys. C, 40, 100001 (2016)
2596 and 2017 update.
- 2597 [10] M. Goldhaber, L. Grodzins, A.W. Sunyar "Helicity of Neutrinos", Phys. Rev.
2598 109, 1015 (1958).
- 2599 [11] Palanque-Delabrouille N et al. "Neutrino masses and cosmology with Lyman-
2600 alpha forest power spectrum", JCAP 11 011 (2015).
- 2601 [12] M. Gell-Mann. "A Schematic Model of Baryons and Mesons". Physics Letters.
2602 8 (3): 214-215 (1964).
- 2603 [13] G. Zweig. "An SU(3) Model for Strong Interaction Symmetry and its Breaking"
2604 (PDF). CERN Report No.8182/TH.401 (1964).
- 2605 [14] G. Zweig. "An SU(3) Model for Strong Interaction Symmetry and its Breaking:
2606 II" (PDF). CERN Report No.8419/TH.412(1964).
- 2607 [15] M. Gell-Mann. "The Interpretation of the New Particles as Displaced Charged
2608 Multiplets". Il Nuovo Cimento 4: 848. (1956).
- 2609 [16] T. Nakano, K. Nishijima. "Charge Independence for V-particles". Progress of
2610 Theoretical Physics 10 (5): 581-582. (1953).
- 2611 [17] N. Cabibbo, "Unitary symmetry and leptonic decays" Physical Review Letters,
2612 vol. 10, no. 12, p. 531, (1963).

- 2613 [18] M.Kobayashi, T.Maskawa, “CP-violation in the renormalizable theory of weak
2614 interaction,” Progress of Theoretical Physics, vol. 49, no. 2, pp. 652-657, (1973).
- 2615 [19] File: Weak Decay (flipped).svg. (2017, June 12). Wikimedia Com-
2616 mons, the free media repository. Retrieved November 27, 2017
2617 from [https://commons.wikimedia.org/w/index.php?title=File:
2618 Weak_Decay_\(flipped\)\.svg&oldid=247498592](https://commons.wikimedia.org/w/index.php?title=File:Weak_Decay_(flipped)\.svg&oldid=247498592).
- 2619 [20] Georgia Tech University. Coupling Constants for the Fundamental Forces(2005).
2620 Retrieved January 10, 2018, from [http://hyperphysics.phy-astr.gsu.edu/
2621 hbase/Forces/couple.html#c2](http://hyperphysics.phy-astr.gsu.edu/hbase/Forces/couple.html#c2)
- 2622 [21] M. Strassler. (May 31, 2013).The Strengths of the Known Forces. Retrieved Jan-
2623 uary 10, 2018, from [https://profmattstrassler.com/articles-and-posts/
2624 particle-physics-basics/the-known-forces-of-nature/
2625 the-strength-of-the-known-forces/](https://profmattstrassler.com/articles-and-posts/particle-physics-basics/the-known-forces-of-nature/the-strength-of-the-known-forces/)
- 2626 [22] S.L. Glashow. “Partial symmetries of weak interactions”, Nucl. Phys. 22 579-
2627 588, (1961).
- 2628 [23] A. Salam, J.C. Ward. “Electromagnetic and weak interactions”, Physics Letters
2629 13 168-171, (1964).
- 2630 [24] S. Weinberg, “A model of leptons”, Physical Review Letters, vol. 19, no. 21, p.
2631 1264, (1967).
- 2632 [25] M. Peskin, D. Schroeder, “An introduction to quantum field theory”. Perseus
2633 Books Publishing L.L.C., (1995).
- 2634 [26] A. Pich. “The Standard Model of Electroweak Interactions” <https://arxiv.org/abs/1201.0537>

- 2636 [27] G. Arnison et al. (UA1 Collaboration), Phys. Lett. B 122, 103 (1983).
- 2637 [28] M. Banner et al. (UA2 Collaboration), Phys. Lett. B 122, 476 (1983).
- 2638 [29] G. Arnison et al. (UA1 Collaboration), Phys. Lett. B 126, 398 (1983).
- 2639 [30] P. Bagnaia et al. (UA2 Collaboration), Phys. Lett. B 129, 130 (1983).
- 2640 [31] F.Bellaiche. (2012, 2 September). “What’s this Higgs boson anyway?”. Retrieved
2641 from: <https://www.quantum-bits.org/?p=233>
- 2642 [32] M. Endres et al. Nature 487, 454-458 (2012) doi:10.1038/nature11255
- 2643 [33] F. Englert, R. Brout. “Broken Symmetry and the Mass of Gauge
2644 Vector Mesons”. Physical Review Letters. 13 (9): 321-23.(1964)
2645 doi:10.1103/PhysRevLett.13.321
- 2646 [34] P.Higgs. “Broken Symmetries and the Masses of Gauge Bosons”. Physical Re-
2647 view Letters. 13 (16): 508-509,(1964). doi:10.1103/PhysRevLett.13.508.
- 2648 [35] G.Guralnik, C.R. Hagen and T.W.B. Kibble. “Global Conservation Laws
2649 and Massless Particles”. Physical Review Letters. 13 (20): 585-587, (1964).
2650 doi:10.1103/PhysRevLett.13.585.
- 2651 [36] CMS collaboration. “Observation of a new boson at a mass of 125 GeV with
2652 the CMS experiment at the LHC”. Physics Letters B. 716 (1): 30-61 (2012).
2653 arXiv:1207.7235. doi:10.1016/j.physletb.2012.08.021
- 2654 [37] ATLAS collaboration. “Observation of a New Particle in the Search for the Stan-
2655 dard Model Higgs Boson with the ATLAS Detector at the LHC”. Physics Letters
2656 B. 716 (1): 1-29 (2012). arXiv:1207.7214. doi:10.1016/j.physletb.2012.08.020.

- 2657 [38] ATLAS collaboration; CMS collaboration (26 March 2015). “Combined Mea-
 2658 surement of the Higgs Boson Mass in pp Collisions at $\sqrt{s}=7$ and 8 TeV with
 2659 the ATLAS and CMS Experiments”. Physical Review Letters. 114 (19): 191803.
 2660 arXiv:1503.07589. doi:10.1103/PhysRevLett.114.191803.
- 2661 [39] LHC InternationalMasterclasses“When protons collide”. Retrieved from http://atlas.physicsmasterclasses.org/en/zpath_protoncollisions.htm
- 2663 [40] CMS Collaboration, “SM Higgs Branching Ratios and Total Decay Widths (up-
 2664 date in CERN Report4 2016)”. <https://twiki.cern.ch/twiki/bin/view/LHCPhysics/CERNYellowReportPageBR> , last accessed on 17.12.2017.
- 2666 [41] R.Grant V. “Determination of Higgs branching ratios in $H \rightarrow W^+W^- \rightarrow l\nu jj$
 2667 and $H \rightarrow ZZ \rightarrow l^+l^-jj$ channels”. Physics Department, University of Ten-
 2668 nessee (Dated: October 31, 2012). Retrieved from <http://aesop.phys.utk.edu/ph611/2012/projects/Riley.pdf>
- 2670 [42] LHC Higgs Cross Section Working Group, Denner, A., Heinemeyer, S. et al.
 2671 “Standard model Higgs-boson branching ratios with uncertainties”. Eur. Phys.
 2672 J. C (2011) 71: 1753. <https://doi.org/10.1140/epjc/s10052-011-1753-8>
- 2673 [43] D. de Florian et al., LHC Higgs Cross Section Working Group,
 2674 CERNâš2017âš002-M, arXiv:1610.07922[hep-ph] (2016).
- 2675 [44] ATLAS and CMS Collaborations, “Measurements of the Higgs boson produc-
 2676 tion and decay rates and constraints on its couplings from a combined ATLAS
 2677 and CMS analysis of the LHC pp collision data at $\sqrt{s} = 7$ and 8 TeV,” (2016).
 2678 CERN-EP-2016-100, ATLAS-HIGG-2015-07, CMS-HIG-15-002.

- 2679 [45] J. A. Aguilar-Saavedra, R. Benbrik, S. Heinemeyer, and M. Perez-Victoria,
2680 “Handbook of vector-like quarks: Mixing and single production”, Phys. Rev. D
2681 88 (2013) 094010, doi:10.1103/PhysRevD.88.094010, arXiv:1306.0572.
- 2682 [46] A. Greljo, J. F. Kamenik, and J. Kopp, “Disentangling flavor vio-
2683 lation in the top-Higgs sector at the LHC”, JHEP 07 (2014) 046,
2684 doi:10.1007/JHEP07(2014)046, arXiv:1404.1278.
- 2685 [47] F. Demartin, F. Maltoni, K. Mawatari, and M. Zaro, “Higgs production in
2686 association with a single top quark at the LHC,” European Physical Journal C,
2687 vol. 75, p. 267, (2015). doi:10.1140/epjc/s10052-015-3475-9, arXiv:1504.00611.
- 2688 [48] F. Demartin, B. Maier, F. Maltoni, K. Mawatari, and M. Zaro, “tWH associated
2689 production at the LHC”, European Physical Journal C, vol. 77, p. 34, (2017).
2690 arXiv:1607.05862
- 2691 [49] F. Maltoni, K. Paul, T. Stelzer, and S. Willenbrock, “Associated production
2692 of Higgs and single top at hadron colliders”, Phys.Rev. D64 (2001) 094023,
2693 [hep-ph/0106293].
- 2694 [50] S. Biswas, E. Gabrielli, F. Margaroli, and B. Mele, “Direct constraints on the
2695 top-Higgs coupling from the 8 TeV LHC data,” Journal of High Energy Physics,
2696 vol. 07, p. 073, (2013).
- 2697 [51] M. Farina, C. Grojean, F. Maltoni, E. Salvioni, and A. Thamm, “Lifting de-
2698 generacies in Higgs couplings using single top production in association with a
2699 Higgs boson,” Journal of High Energy Physics, vol. 05, p. 022, (2013).
- 2700 [52] T.M. Tait and C.-P. Yuan, “Single top quark production as a window to physics
2701 beyond the standard model”, Phys. Rev. D 63 (2000) 014018 [hep-ph/0007298].

- 2702 [53] CMS Collaboration, “Modelling of the single top-quark production in associa-
2703 tion with the Higgs boson at 13 TeV.” <https://twiki.cern.ch/twiki/bin/viewauth/CMS/SingleTopHiggsGeneration13TeV>, last accessed on 16.01.2018.
- 2705 [54] CMS Collaboration, “SM Higgs production cross sections at $\sqrt{s} =$
2706 13 TeV.” <https://twiki.cern.ch/twiki/bin/view/LHCPhysics/CERNYellowReportPageAt13TeV>, last accessed on 16.01.2018.
- 2708 [55] S. Dawson, The effective W approximation, Nucl. Phys. B 249 (1985) 42.
- 2709 [56] S. Biswas, E. Gabrielli and B. Mele, JHEP 1301 (2013) 088 [arXiv:1211.0499
2710 [hep-ph]].
- 2711 [57] LHC Higgs Cross Section Working Group, “Handbook of LHC Higgs Cross
2712 Sections: 4.Deciphering the Nature of the Higgs Sector”, arXiv:1610.07922.
- 2713 [58] J. Ellis, D. S. Hwang, K. Sakurai, and M. Takeuchi.“Disentangling Higgs-Top
2714 Couplings in Associated Production”, JHEP 1404 (2014) 004, [arXiv:1312.5736].
- 2715 [59] CMS Collaboration, V. Khachatryan et al., “Precise determination of the mass
2716 of the Higgs boson and tests of compatibility of its couplings with the standard
2717 model predictions using proton collisions at 7 and 8 TeV,” arXiv:1412.8662.
- 2718 [60] ATLAS Collaboration, G. Aad et al., “Updated coupling measurements of the
2719 Higgs boson with the ATLAS detector using up to 25 fb^{-1} of proton-proton
2720 collision data”, ATLAS-CONF-2014-009.
- 2721 [61] File:Cern-accelerator-complex.svg. Wikimedia Commons, the free media repos-
2722 itory. Retrieved January, 2018 from <https://commons.wikimedia.org/wiki/File:Cern-accelerator-complex.svg>

- 2724 [62] J.L. Caron , “Layout of the LEP tunnel including future LHC infrastructures.”,
2725 (Nov, 1993). A C Collection. Legacy of AC. Pictures from 1992 to 2002. Re-
2726 trieved from <https://cds.cern.ch/record/841542>
- 2727 [63] M. Vretenar, “The radio-frequency quadrupole”. CERN Yellow Report CERN-
2728 2013-001, pp.207-223 DOI:10.5170/CERN-2013-001.207. arXiv:1303.6762
- 2729 [64] L.Evans. P. Bryant (editors). “LHC Machine”. JINST 3 S08001 (2008).
- 2730 [65] CERN Photographic Service.“Radio-frequency quadrupole, RFQ-1”, March
2731 1983, CERN-AC-8303511. Retrieved from <https://cds.cern.ch/record/615852>.
- 2733 [66] CERN Photographic Service “Animation of CERN’s accelerator network”, 14
2734 October 2013. DOI: 10.17181/cds.1610170 Retrieved from <https://videos.cern.ch/record/1610170>
- 2736 [67] C.Sutton. “Particle accelerator”.Encyclopedia Britannica. July 17,
2737 2013. Retrieved from <https://www.britannica.com/technology/particle-accelerator>.
- 2739 [68] L.Guiraud. “Installation of LHC cavity in vacuum tank.”. July 27 2000. CERN-
2740 AC-0007016. Retrieved from <https://cds.cern.ch/record/41567>.
- 2741 [69] J.L. Caron, “Magnetic field induced by the LHC dipole’s superconducting coils”.
2742 March 1998. AC Collection. Legacy of AC. Pictures from 1992 to 2002. LHC-
2743 PHO-1998-325. Retrieved from <https://cds.cern.ch/record/841511>.
- 2744 [70] AC Team. “Diagram of an LHC dipole magnet”. June 1999. CERN-DI-9906025
2745 retrieved from <https://cds.cern.ch/record/40524>.

- 2746 [71] CMS Collaboration “Public CMS Luminosity Information”. https://twiki.cern.ch/twiki/bin/view/CMSPublic/LumiPublicResults#2016__proton_proton_13_TeV_collis, last accessed 24.01.2018
- 2747
- 2748
- 2749 [72] J.L Caron. “LHC Layout” AC Collection. Legacy of AC. Pictures from 1992
2750 to 2002. September 1997, LHC-PHO-1997-060. Retrieved from <https://cds.cern.ch/record/841573>.
- 2751
- 2752 [73] J.A. Coarasa. “The CMS Online Cluster:Setup, Operation and Maintenance
2753 of an Evolving Cluster”. ISGC 2012, 26 February - 2 March 2012, Academia
2754 Sinica, Taipei, Taiwan.
- 2755 [74] CMS Collaboration. “The CMS experiment at the CERN LHC” JINST 3 S08004
2756 (2008).
- 2757 [75] CMS Collaboration. “CMS detector drawings 2012” CMS-PHO-GEN-2012-002.
2758 Retrieved from <http://cds.cern.ch/record/1433717>.
- 2759 [76] Davis, Siona Ruth. “Interactive Slice of the CMS detector”, Aug. 2016,
2760 CMS-OUTREACH-2016-027, retrieved from <https://cds.cern.ch/record/2205172>
- 2761
- 2762 [77] R. Breedon. “View through the CMS detector during the cooldown of the
2763 solenoid on February 2006. CMS Collection”, February 2006, CMS-PHO-
2764 OREACH-2005-004, Retrieved from <https://cds.cern.ch/record/930094>.
- 2765 [78] Halyo, V. and LeGresley, P. and Lujan, P. “Massively Parallel Computing and
2766 the Search for Jets and Black Holes at the LHC”, Nucl.Instrum.Meth. A744
2767 (2014) 54-60, DOI: 10.1016/j.nima.2014.01.038”

- 2768 [79] A. Dominguez et. al. “CMS Technical Design Report for the Pixel Detector
2769 Upgrade”, CERN-LHCC-2012-016. CMS-TDR-11.
- 2770 [80] CMS Collaboration. “Description and performance of track and primary-vertex
2771 reconstruction with the CMS tracker,” Journal of Instrumentation, vol. 9, no.
2772 10, p. P10009,(2014).
- 2773 [81] CMS Collaboration and M. Brice. “Images of the CMS Tracker Inner Bar-
2774 rel”, November 2008, CMS-PHO-TRACKER-2008-002. Retrieved from <https://cds.cern.ch/record/1431467>.
- 2776 [82] M. Weber. “The CMS tracker”. 6th international conference on hyperons, charm
2777 and beauty hadrons Chicago, June 28-July 3 2004.
- 2778 [83] CMS Collaboration. “Projected Performance of an Upgraded CMS Detector at
2779 the LHC and HL-LHC: Contribution to the Snowmass Process”. Jul 26, 2013.
2780 arXiv:1307.7135
- 2781 [84] L. Veillet. “End assembly of HB with EB rails and rotation inside SX ”,Jan-
2782 uary 2002. CMS-PHO-HCAL-2002-002. Retrieved from <https://cds.cern.ch/record/42594>.
- 2784 [85] J. Puerta-Pelayo.“First DT+RPC chambers installation round in the UX5 cav-
2785 ern.”. January 2007, CMS-PHO-OREACH-2007-001. Retrieved from <https://cds.cern.ch/record/1019185>
- 2787 [86] X. Cid Vidal and R. Cid Manzano. “CMS Global Muon Trigger” web site:
2788 Taking a closer look at LHC. Retrieved from https://www.lhc-closer.es/taking_a_closer_look_at_lhc/0.lhc_trigger

- 2790 [87] WLCG Project Office, “Documents & Reference - Tiers - Structure,”
 2791 (2014). <http://wlcg.web.cern.ch/documents-reference> , last accessed on
 2792 30.01.2018.
- 2793 [88] CMS Collaboration. “CMSSW Application Framework”, <https://twiki.cern.ch/twiki/bin/view/CMSPublic/WorkBookCMSSWFramework>,
 2794 last accesses 06.02.2018
- 2796 [89] A. Buckleya, J. Butterworthb, S. Giesekec, et. al. “General-purpose event gen-
 2797 erators for LHC physics”. arXiv:1101.2599v1 [hep-ph] 13 Jan 2011
- 2798 [90] A. Quadt. “Top Quark Physics at Hadron Colliders”. Advances in the Physics
 2799 of Particles and Nuclei. Springer-Verlag Berlin Heidelberg. DOI: 10.1007/978-
 2800 3-540-71060-8 (2007)
- 2801 [91] DurhamHep Data Project, “The Durham HepData Project - PDF Plotter.”
 2802 <http://hepdata.cedar.ac.uk/pdf/pdf3.html> , last accessed on 02.02.2018.
- 2803 [92] G. Altarelli and G. Parisi. “ASYMPTOTIC FREEDOM IN PARTON LAN-
 2804 GUAGE”, Nucl.Phys. B126:298 (1977).
- 2805 [93] Yu.L. Dokshitzer. Sov.Phys. JETP 46:641 (1977)
- 2806 [94] V.N. Gribov, L.N. Lipatov. “Deep inelastic e p scattering in perturbation the-
 2807 ory”, Sov.J.Nucl.Phys. 15:438 (1972)
- 2808 [95] F. Maltoni, G. Ridolfi, and M. Ubiali, “b-initiated processes at the LHC: a
 2809 reappraisal,” Journal of High Energy Physics, vol. 07, p. 022, (2012).
- 2810 [96] B. Andersson, G. Gustafson, G. Ingelman and T. Sjostrand, “Parton fragmen-
 2811 tation and string dynamics”, Physics Reports, Vol. 97, No. 2-3, pp. 31-145,
 2812 1983.

- 2813 [97] CMS Collaboration, “Event generator tunes obtained from underlying event
2814 and multiparton scattering measurements;” European Physical Journal C, vol.
2815 76, no. 3, p. 155, (2016).
- 2816 [98] J. Alwall et. al., “The automated computation of tree-level and next-to-leading
2817 order differential cross sections, and their matching to parton shower simula-
2818 tions,” Journal of High Energy Physics, vol. 07, p. 079, (2014).
- 2819 [99] T. Sjöstrand and P. Z. Skands, “Transverse-momentum-ordered showers and
2820 interleaved multiple interactions,” European Physical Journal C, vol. 39, pp.
2821 129–154, (2005).
- 2822 [100] S. Frixione, P. Nason, and C. Oleari, “Matching NLO QCD computations with
2823 Parton Shower simulations: the POWHEG method,” Journal of High Energy
2824 Physics, vol. 11, p. 070, (2007).
- 2825 [101] S. Agostinelli et al., “GEANT4: A Simulation toolkit,” Nuclear Instruments
2826 and Methods in Physics, vol. A506, pp. 250–303, (2003).
- 2827 [102] J.Allison et.al.,“Recent developments in Geant4”, Nuclear Instruments and
2828 Methods in Physics Research A 835 (2016) 186-225.
- 2829 [103] CMS Collaboration “Full Simulation Offline Guide”, <https://twiki.cern.ch/twiki/bin/view/CMSPublic/SWGuideSimulation>, last accessed 04.02.2018
- 2831 [104] A. Giammanco. “The Fast Simulation of the CMS Experiment” J. Phys.: Conf.
2832 Ser. 513 022012 (2014)
- 2833 [105] A.M. Sirunyan et. al. “Particle-flow reconstruction and global event description
2834 with the CMS detector”, JINST 12 P10003 (2017) <https://doi.org/10.1088/1748-0221/12/10/P10003>.

- 2836 [106] The CMS Collaboration. “ Description and performance of track and pri-
2837 mary vertex reconstruction with the CMS tracker”. JINST 9 P10009 (2014).
2838 doi:10.1088/1748-0221/9/10/P10009
- 2839 [107] J. Incandela. “Status of the CMS SM Higgs Search” July 4, 2012. Pdf slides.
2840 Retrieved from https://indico.cern.ch/event/197461/contributions/1478917/attachments/290954/406673/CMS_4July2012_Final.pdf
- 2842 [108] P. Billoir and S. Qian, “Simultaneous pattern recognition and track fitting by
2843 the Kalman filtering method”, Nucl. Instrum. Meth. A 294 219. (1990).
- 2844 [109] W. Adam, R. Fruhwirth, A. Strandlie and T. Todorov, “Reconstruction of
2845 electrons with the Gaussian sum filter in the CMS tracker at LHC”, eConf
2846 C 0303241 (2003) TULT009 [physics/0306087].
- 2847 [110] K. Rose, “Deterministic Annealing for Clustering, Compression, Classification,
2848 Regression and related Optimisation Problems”, Proc. IEEE 86 (1998) 2210.
- 2849 [111] R. Fruhwirth, W. Waltenberger and P. Vanlaer, “ Adaptive Vertex Fitting”,
2850 CMS Note 2007-008 (2007).
- 2851 [112] CMS collaboration, “Performance of CMS muon reconstruction in pp collision
2852 events at $\sqrt{s} = 7 \text{ TeV}$ ”, JINST 7 P10002 2012, [arXiv:1206.4071].
- 2853 [113] M. Cacciari, G. P. Salam, and G. Soyez, “The anti- k_t jet clustering algorithm,”
2854 Journal of High Energy Physics, vol. 04, p. 063, (2008).
- 2855 [114] B. Dorney. “Anatomy of a Jet in CMS”. Quantum Diaries. June
2856 1st, 2011. Retrieved from <https://www.quantumdiaries.org/2011/06/01/anatomy-of-a-jet-in-cms/>

- 2858 [115] The CMS Collaboration.“Event Displays from the high-energy collisions at 7
2859 TeV”, May 2010, CMS-PHO-EVENTS-2010-007, Retrieved from <https://cds.cern.ch/record/1429614>.
- 2861 [116] The CMS collaboration. “Determination of jet energy calibration and transverse
2862 momentum resolution in CMS”. JINST 6 P11002 (2011). <http://dx.doi.org/10.1088/1748-0221/6/11/P11002>
- 2864 [117] The CMS Collaboration, “Introduction to Jet Energy Corrections at
2865 CMS.”. <https://twiki.cern.ch/twiki/bin/view/CMS/IntroToJEC>, last ac-
2866 cessed 10.02.2018.
- 2867 [118] CMS Collaboration Collaboration. “Identification of b quark jets at the CMS
2868 Experiment in the LHC Run 2”. Tech. rep. CMS-PAS-BTV-15-001. Geneva:
2869 CERN, (2016). <https://cds.cern.ch/record/2138504>.
- 2870 [119] CMS Collaboration Collaboration. “Performance of missing energy reconstruc-
2871 tion in 13 TeV pp collision data using the CMS detector”. Tech. rep. CMS-PAS-
2872 JME16-004. Geneva: CERN, 2016. <https://cds.cern.ch/record/2205284>.
- 2873 [120] CMS Collaboration, “New CMS results at Moriond (Electroweak) 2013”,
2874 Retrieved from http://cms.web.cern.ch/sites/cms.web.cern.ch/files/styles/large/public/field/image/HIG13004_Event01_0.png?itok=LAWZzPHR
- 2877 [121] CMS Collaboration, “New CMS results at Moriond (Electroweak) 2013”,
2878 Retrieved from http://cms.web.cern.ch/sites/cms.web.cern.ch/files/styles/large/public/field/image/TOP12035_Event01.png?itok=uMdnSqzC

- 2881 [122] K. Skovpen. “Event displays highlighting the main properties of heavy flavour
2882 jets in the CMS Experiment”, Aug 2017, CMS-PHO-EVENTS-2017-006. Re-
2883 trieved from <https://cds.cern.ch/record/2280025>.
- 2884 [123] G. Cowan. “Topics in statistical data analysis for high-energy physics”.
2885 arXiv:1012.3589v1
- 2886 [124] A. Hoecker et al., “TMVA-Toolkit for multivariate data analysis”
2887 arXiv:physics/0703039v5 (2009)
- 2888 [125] L. Lista. “Statistical Methods for Data Analysis in Particle Physics”, 2nd
2889 ed. Springer International Publishing. (2017) <https://dx.doi.org/10.1007/978-3-319-62840-0>
- 2891 [126] I. Antcheva et al., “ROOT-A C++ framework for petabyte data storage, sta-
2892 tistical analysis and visualization ,” Computer Physics Communications, vol.
2893 182, no. 6, pp. 1384–1385, (2011).
- 2894 [127] Y. Coadou. “Boosted decision trees”, ESIPAP, Archamps, 9 Febru-
2895 ary 2016. Lecture. Retrieved from https://indico.cern.ch/event/472305/contributions/1982360/attachments/1224979/1792797/ESIPAP_MVA160208-BDT.pdf
- 2898 [128] J.H. Friedman. “Greedy function approximation: A gradient boosting ma-
2899 chine”. Ann. Statist. Volume 29, Number 5 (2001), 1189-1232. https://projecteuclid.org/download/pdf_1/euclid-aos/1013203451.
- 2901 [129] F. James, M. Roos, “MINUIT: Function minimization and error analysis”. Cern
2902 Computer Centre Program Library, Geneve Long Write-up No. D506, 1989

- 2903 [130] J. Neyman and E. S. Pearson, “On the problem of the most efficient tests
 2904 of statistical hypotheses”. Philosophical Transactions of the Royal Society of
 2905 London. Series A, Containing Papers of a Mathematical or Physical Character.
 2906 Vol. 231 (1933), pp. 289-337
- 2907 [131] B. Hespel, F. Maltoni, and E. Vryonidou, “Higgs and Z boson associated pro-
 2908 duction via gluon fusion in the SM and the 2HDM”, JHEP 06 (2015) 065,
 2909 [https://dx.doi.org/10.1007/JHEP06\(2015\)065](https://dx.doi.org/10.1007/JHEP06(2015)065), arXiv:1503.01656.
- 2910 [132] ATLAS Collaboration, “Measurements of Higgs boson produc-
 2911 tion and couplings in diboson final states with the ATLAS
 2912 detector at the LHC”, Phys. Lett. B726 (2013) 88–119,
 2913 doi:10.1016/j.physletb.2014.05.011, 10.1016/j.physletb.2013.08.010,
 2914 arXiv:1307.1427. [Erratum: Phys. Lett.B734,406(2014)].
- 2915 [133] CMS Collaboration, “Search for the associated production of a Higgs boson
 2916 with a single top quark in proton-proton collisions at $\sqrt{s} = 8$ TeV”, JHEP 06
 2917 (2016) 177, doi:10.1007/JHEP06(2016)177, arXiv:1509.08159.
- 2918 [134] B. Stieger, C. Jordá Lope et al., “Search for Associated Production of a Single
 2919 Top Quark and a Higgs Boson in Leptonic Channels”, CMS Analysis Note CMS
 2920 AN-14-140, 2014.
- 2921 [135] M. Peruzzi, C. Mueller, B. Stieger et al., “Search for ttH in multilepton final
 2922 states at $\sqrt{s} = 13$ TeV”, CMS Analysis Note CMS AN-16-211, 2016.
- 2923 [136] CMS Collaboration, “Search for H to bbar in association with a single top quark
 2924 as a test of Higgs boson couplings at $\sqrt{s} = 13$ TeV”, CMS Physics Analysis
 2925 Summary CMS-PAS-HIG-16-019, 2016.

- 2926 [137] CMS Collaboration, “Search for production of a Higgs boson and a single top
2927 quark in multilepton final states in proton collisions at $\sqrt{s} = 13$ TeV”, CMS
2928 Physics Analysis Summary CMS-PAS-HIG-17-005, 2016.
- 2929 [138] B. WG, “BtagRecommendation80XReReco”, February, 2017. <https://twiki.cern.ch/twiki/bin/view/CMS/BtagRecommendation80XReReco>.
- 2931 [139] CMS Collaboration, “Identification of b quark jets at the CMS Experiment
2932 in the LHC Run 2”, CMS Physics Analysis Summary CMS-PAS-BTV-15-001,
2933 2016.
- 2934 [140] M. Peruzzi, F. Romeo, B. Stieger et al., “Search for ttH in multilepton final
2935 states at $\sqrt{s} = 13$ TeV”, CMS Analysis Note CMS AN-17-029, 2017.
- 2936 [141] CMS Collaboration, “Baseline muon selections for Run-II.” <https://twiki.cern.ch/twiki/bin/view/CMSPublic/SWGuideMuonIdRun2>, last accessed on
2937 24.02.2018.
- 2939 [142] G. Petrucciani and C. Botta, “Two step prompt muon identification”, January,
2940 2015. <https://indico.cern.ch/event/368007/contribution/2/material/slides/0.pdf>.
- 2942 [143] H. Brun and C. Ochando, “Updated Results on MVA eID with 13 TeV samples”,
2943 October, 2014. <https://indico.cern.ch/event/298249/contribution/3/material/slides/0.pdf>.
- 2945 [144] K. Rehermann and B. Tweedie, “Efficient Identification of Boosted Semileptonic
2946 Top Quarks at the LHC”, JHEP 03 (2011) 059, [https://dx.doi.org/10.1007/JHEP03\(2011\)059](https://dx.doi.org/10.1007/JHEP03(2011)059), arXiv:1007.2221.

- 2948 [145] CMS Collaboration. “Tag and Probe”, [https://twiki.cern.ch/twiki/bin/
2949 view/CMSPublic/TagAndProbe](https://twiki.cern.ch/twiki/bin/view/CMSPublic/TagAndProbe), last accessed on 02.03.2018.
- 2950 [146] B. Maier, “SingleTopHiggProduction13TeV”, February, 2016. [https://twiki.
2951 cern.ch/twiki/bin/viewauth/CMS/SingleTopHiggsGeneration13TeV](https://twiki.cern.ch/twiki/bin/viewauth/CMS/SingleTopHiggsGeneration13TeV).